

ULTRA-LOW EMITTANCE III-V SEMICONDUCTOR PHOTOCATHODES

A Dissertation

Presented to the Faculty of the Graduate School
of Cornell University

in Partial Fulfillment of the Requirements for the Degree of
Doctor of Philosophy

by

Siddharth Srikrishna Karkare

May 2015

© 2015 Siddharth Srikrishna Karkare
ALL RIGHTS RESERVED

ULTRA-LOW EMITTANCE III-V SEMICONDUCTOR PHOTOCATHODES

Siddharth Srikrishna Karkare, Ph.D.

Cornell University 2015

Performance of large (km scale) electron accelerators (used for high energy physics experiments and as x-ray sources) as well as small (m scale) ultra-fast electron diffraction setups is limited by the source of electrons. Low energy (< 1 eV) electrons obtained using visible light from III-V semiconductors activated to negative electron affinity (NEA) are essential for many of these applications. Much of the physics behind the photoemission of electrons from such semiconductors is not well understood. A good understanding of this photoemission will enable design of novel materials that will have enhanced photoemission properties to improve the performance of the fore-mentioned applications. This thesis presents our theoretical, computational and experimental advances to achieve greater understanding of the photoemission process and their application to develop novel III-V semiconductor based structures that enhance photoemission properties.

First, using Monte Carlo based electron transport in conjunction with the three step photoemission model, we develop a photoemission simulation that explains the experimentally observed photoemission properties of NEA III-V photoemitters. Based on this simulation, novel layered III-V semiconductors have been designed and grown using molecular beam epitaxy (MBE) to enhance photoemission characteristics.

Second, we identify and discuss the various possible causes of the discrepancy between the theoretically predicted and experimentally observed energy

distributions. Effects of surface roughness and work-function non-uniformities at various length scales have been explored in detail. Ab-initio calculations using density functional theory are used to obtain properties of the photoemitting surface of GaAs based photocathodes and explore possible reasons behind surface non-uniformities.

Last, to improve photoemission diagnostics, a 2-D electron energy analyzer, which is capable of measuring the longitudinal (along the surface normal) and transverse (perpendicular to the surface normal) energy distributions simultaneously, has been designed and built. This energy analyzer uses the motion of low energy electrons in a strong magnetic field along with the principle of adiabatic invariance to measure the energy distribution of electrons with a resolution better than 6 meV rms.

BIOGRAPHICAL SKETCH

Siddharth Karkare was born in Pune, Maharashtra, India on 15th October, 1987. He obtained his undergraduate degree of Bachelors in Technology in the field of Energy Engineering with a minor in Physics from Indian Institute of Technology, Kharagpur, West Bengal, India in 2009. During his undergraduate course of study Siddharth worked on several small research projects in the field of neuro-signal processing under the guidance of Prof. Goutam Saha and molecular dynamics simulations under the guidance of Prof. Suman Chakraborty.

After finishing his undergraduate education, Siddharth moved to Ithaca, New York, where he completed his Master of Engineering degree in Engineering Physics at Cornell University in 2010. He continued at Cornell University as a graduate student in physics to obtain his Ph.D. in May 2015. His work mainly focused on studying low energy photoemission from high quantum efficiency materials used as electron sources for various high energy physics, x-ray and ultra-fast imaging applications. After graduation he will continue working in the same field as a post-doctoral research fellow at the Lawrence Berkeley National Lab, Berkeley California.

Dedicated to my family, friends and mentors.

ACKNOWLEDGEMENTS

I would begin by expressing immense gratitude towards my advisor, Prof. Ivan Bazarov, for his support and guidance through every step of my Ph.D. I have always admired his demeanor and how he approaches every problem, breaking it down to the simplest of problems. I would also like to thank Dr. Luca Cultrera and Tobey Moore. Their assistance and expertise was invaluable during my Ph.D. and I have learnt a great deal from them. I would also like to thank Dr. Bruce Dunham, Dr. Xianghong Liu, Dr. Yulin Li, Dr. Bill Schaff, Dr. Adam Bartnik, Karl Smolenski, my fellow graduate students - Colwyn Gulliford, Jared Maxson, Hyeri Lee and Hexuan Wang - and all other electron source group members for their inputs and assistance throughout my Ph.D. I would also like to extend a special thanks to Dr. Arunima Singh and Prof. Richard Hennig for their inputs regarding ab-initio calculations and Dr. Dimitri Dimitrov from Tech-X, Boulder, CO, for his inputs regarding the photoemission simulations.

I would like to give a special note of thanks to all the undergraduate and REU students, Ashwathi Iyer, Yoon-Woo Hwang, Richard Merluzzi, Eric Sawyer, Andrew Kim, Laurent Boulet, Teresa Esposito and Nicholas Erickson whom I had the opportunity and pleasure of working with and mentoring during my Ph.D. They have been of immense help in various aspects of the work presented in this thesis.

I would also like to thank the members of my special committee, Prof. Kyle Shen and Prof. Tomas Arias for their inputs at various points during my Ph.D.

I would also like to thank my family and friends for making my time in Ithaca very memorable part of my life. I will greatly cherish the memories I have about the time I spent with them.

Finally, I would like to acknowledge the funding support from the Department of Energy under Grant No. DE-SC0003965 and the National Science Foundation under Grant No. DMR-0807731. I would also like to acknowledge the support of the computational facilities provided by CHESS for some of the work presented in this thesis.

TABLE OF CONTENTS

Biographical Sketch	iii
Dedication	iv
Acknowledgements	v
Table of Contents	vii
List of Tables	x
List of Figures	xi
1 Introduction	1
1.1 Photoinjectors and photocathodes	1
1.2 Photocathode requirements	3
1.3 Challenges in ultra-low energy photoemission	4
1.4 Negative electron affinity III-V semiconductor photocathodes	6
1.5 Thesis outline	8
2 Monte Carlo charge transport and photoemission from negative electron affinity GaAs photocathodes	10
2.1 Abstract	10
2.2 Introduction	10
2.3 Model	13
2.3.1 Three valley model	13
2.3.2 Excitation	18
2.3.3 Conduction band electron transport	21
2.3.4 Treatment of GaAs to vacuum interface and emission	30
2.4 Comparison to photoemission experiments	41
2.4.1 Spectral response	41
2.4.2 Mean transverse energy and angular distributions	43
2.4.3 Response time	44
2.5 Limitations of the simulation	45
2.6 Conclusion and future work	46
3 Layered III-V Semiconductor Photocathodes	48
3.1 Abstract	48
3.2 Introduction	48
3.3 Design of Layered Structures	52
3.4 Experimental Results	56
3.5 Conclusion	58
4 Effects of surface non-uniformities on the mean transverse energy from photocathodes	61
4.1 Abstract	61
4.2 Introduction	61
4.3 Classical treatment	65

4.3.1	Details of model and calculation	65
4.3.2	Results	68
4.4	Quantum treatment	71
4.4.1	Emission model	71
4.4.2	Example of NEA-GaAs	76
4.5	Conclusion	79
5	Ab-initio studies of Cs on GaAs (100) and (110) surfaces	81
5.1	Abstract	81
5.2	Introduction	81
5.3	Simulation methods and details	84
5.3.1	Computational methods	84
5.3.2	Surface structures	85
5.3.3	Cs adsorption calculations	87
5.4	Results and Discussion	90
5.4.1	Mobility of Cs at low coverages	90
5.4.2	Cs position distribution	93
5.4.3	Work function change and adsorption energy	93
5.5	Conclusion	96
6	2-D energy analyzer for low energy electrons	98
6.1	Abstract	98
6.2	Introduction	98
6.3	Theory of low energy electron beams in strong magnetic fields	100
6.3.1	Adiabatic invariance and energy conservation	100
6.3.2	Motion of the guiding center	103
6.3.3	Verification by simulation	104
6.4	Description of the setup and measurement	105
6.4.1	Description of setup	105
6.4.2	Marking of electrons with a particular longitudinal energy	108
6.4.3	Measuring the 2-D energy distribution	110
6.4.4	Measuring the MTE	115
6.5	Optimizing the signal to noise ratio and the energy resolution	116
6.5.1	The signal to noise ratio	116
6.5.2	The energy resolution	117
6.6	Conclusion	121
7	Conclusion	122
A	Calculation of energy resolution	125
B	2-D energy distributions from quantum well and super-lattice structures	129
B.1	Physical and electronic structures	129

B.1.1	Quantum well structure	129
B.1.2	Super-lattice structure	131
B.2	Activation and spectral response	133
B.3	2-D energy distributions	134
B.4	Conclusion	137
Bibliography		139

LIST OF TABLES

2.1	List of symbols and values used	17
2.2	Response time for thin GaAs photocathodes under 1.46 eV excitation. The experimental values in column two are from Aulenbacher <i>et al.</i> [33]	44

LIST OF FIGURES

2.1	(a) Band Structure of GaAs showing the lowermost conduction band and the top 3 (heavy-hole, light-hole and split-off) valence bands. (b) Three valley model for GaAs band structure. The lowest conduction band is modeled as 3 spherical nearly parabolic valleys (Γ , L and X valleys) and the top three valence bands are modeled as spherical parabolic bands about the Γ point.	14
2.2	Absorption length vs photon energy for various doping levels as calculated by Perera <i>et al.</i> [47]. It can be seen that GaAs is nearly transparent to photon energies less than 1.4eV (band-gap).	18
2.3	Electron excitation from top 3 valence bands to the lowest conduction band. Only direct (vertical) transitions are shown. Indirect, inter-valence band and multi-photon transitions have been ignored.	20
2.4	Scattering rates for various valleys (a) Γ valley, (b) L valley, (c) X valley. In all valleys, at lower energies, the impurity and hole scattering are the dominant scattering mechanisms, followed by inter-valley optical scattering.	29
2.5	Comparison of simulated and experimental[50] drift velocities at different electric fields and p -doping densities of $N=1.5 \times 10^{17} \text{ cm}^{-3}$, $1.5 \times 10^{18} \text{ cm}^{-3}$ and $1 \times 10^{19} \text{ cm}^{-3}$. The main cause of disagreement is the assumption of the L and X valleys being spherical rather than ellipsoidal and the inaccuracy in the screening mechanism.	30
2.6	Band diagram of GaAs(Cs/F) near the surface for p -doping concentration of $1 \times 10^{19} \text{ cm}^{-3}$. The surface exhibits negative electron affinity condition ($E_A < 0$).	31
2.7	Magnitude of band bending vs doping density. The band bending magnitude is given as the difference between the Fermi level to VBM gap in the bulk and at the surface. In the bulk, this gap is determined by the doping level[53] and at the surface this gap is determined by the Fermi level pinning[54].	32
2.8	Band bending width vs doping density. The band bending width is calculated assuming the formation of a depletion region near the surface due to the electrons donated by the Cs atoms[54,55].	33
2.9	Mean transverse energy of emitted electrons using classical step boundary, assuming a thermalized electrons in GaAs, no band bending and no surface barrier.	36
2.10	Angular distribution of emitted electrons per unit solid angle obtained by the simulation, assuming a thermalized electrons in GaAs, no band bending and no surface barrier compared to the analytic result for the same case[30].	36

2.11	(a) Surface barrier predicted by Fisher <i>et al.</i> [57] and Spicer <i>et al.</i> [35] (assuming a negative affinity of 0.1 eV). (b) Arbitrarily shaped barrier approximated as a series of rectangles to calculate the transmission probability using the propagation matrix approach. (c) Fisher's barrier used to calculate transmission probability in Fig. 2.12.	38
2.12	Transmission probability vs longitudinal component of k-vector. The result depends on the transverse component of the wave-vector due to the change in the effective mass during emission and the non-parabolic valleys.	40
2.13	Comparison of measured and simulated spectral response. Electron affinity (E_A) is a variable parameter in the simulation. It is seen that the best fit is obtained for $E_A=-0.02$ eV.	42
2.14	Comparison of measured (data by Bazarov <i>et al.</i> [13] and data by Liu <i>et al.</i> [30]) and simulated MTE with and without surface scattering. Electron affinity is assumed to be 15 meV for simulations.	43
2.15	Simulated and experimental [13] response times for photon energies of 1.74 eV and 2.38 eV. The simulated values show a variation in the response time with electron affinity, but the electron affinity is unknown for the experimental data.	45
3.1	Process of photoemission from a) activated <i>p</i> -doped GaAs, b) layered structure with 100nm intrinsic GaAs. The various electron processes (indicated A-H) are described in the text.	52
3.2	Simulations of a) QE, b) Response time and c) MTE as a function of the thickness of intrinsic GaAs layer for NEA of 100meV and 200meV. A thin layer of intrinsic GaAs on heavily <i>p</i> -doped GaAs causes the response time and MTE to reduce, changing them in a favorable way. The reduction in QE is unfavorable but can be tolerated for use in a photoinjector.	57
3.3	a) QE and b)MTE as a function of incident photon energy for the two samples. The simulated results agree well with the experiment. The layered cathode shows a reduced QE w.r.t the control sample. However, the QE is still greater than 1% in the green, exceeding the QE requirement of most photoinjectors[12]. NEA is fixed for a particular sample. It should be noted that the photon energy range above 2.4 eV is outside the validity of the 3-valley model for GaAs and cannot be simulated.	59
4.1	Parallel plate capacitor model to calculate the effect of variation of work function on MTE. The equipotential lines get distorted near the cathode due to the non-uniform work function. This causes the electrons emitted from the cathode to gain transverse energy.	66

4.2	(a) Variation of MTE with h . The external electric field was set to zero for these calculations. (b) Variation of the MTE with the electric field, E_0 . The value of a was set to 100 nm for these calculations. h/a for the red curve is 1 MV/m and for the blue curve is 6 MV/m (shown by the black lines). The MTE is nearly independent of the electric field when $E_0 < h/a$, beyond that it reduces sharply with the electric field.	70
4.3	(a) Variation of MTE with the initial kinetic energy. $E_0 = 10$ MV/m, $h = 0.1$ V and $a = 100$ nm (b) Variation of MTE with the the period a . $E_0 = 10$ MV/m, $h = 0.1$ V and $K = 1$ meV.	70
4.4	(a) Potential to model the surface non-uniformities along with the incoming and scattered wave functions (b) δ function approximation to the potential used to account for surface non-uniformities	72
4.5	(a) Potential to model the GaAs surface. The non-uniformities are modeled using a small sinusoidal roughness of in the x direction (b) The sinusoidal roughness is approximated using a δ function.	77
4.6	(a) Calculated MTE as a function of the period (λ) of the surface non-uniformity for various electron energies. A spike in MTE occurs whenever the electron energy is sufficient to allow scattering into a higher order transverse wave-vector. (b) Calculated MTE as a function of the period (λ) for a realistic distribution of incoming wave-vectors. The MTE measured experimentally and calculated without the surface non-uniformity are also shown.	78
5.1	(Color online) (a) Top and (b) side view of the relaxed Ga terminated GaAs(100)-(4 \times 2) surface slab. (c) Top and (d) side view of the relaxed GaAs(110) surface. Both cells have a vacuum spacing of 25 Å, which sufficiently reduces interactions between the slabs. The Ga atoms are shown in red and the As atoms are shown in blue. For the (100) surface the x , y and z axes indicate the [011], [0 $\bar{1}$ 1] and [100] directions respectively. For the (110) surface the x , y and z axes indicate the [00 $\bar{1}$], [$\bar{1}$ 10] and [110] directions respectively.	86
5.2	The energy barrier for the diffusion of Cs, (a) along the trench ([011] direction) on GaAs(100), (b) across the dimer ([01 $\bar{1}$] direction) on GaAs(100), (c) between two adjacent X sites along the [00 $\bar{1}$] direction on GaAs(110), and (d) between two adjacent X sites along the perpendicular [1 $\bar{1}$ 0] direction on GaAs(110). Ga atoms are shown in red and As atoms in blue. The initial position of the diffusing Cs atom is shown as a yellow sphere, subsequent images along the minimum energy path of the Cs atom are shown as circles with the darkest circle denoting the final position.	88

5.3	Top view of the Cs position distributions on the (100) surface for Cs surface densities of (a) 0.78, (b) 2.35, and (c) 3.91 nm ⁻² , respectively. Top view of Cs position distributions on the (110) surface for Cs densities of (d) 0.74, (b) 2.21, and 3.69 nm ⁻² , respectively. The Cs position distributions are overlaid on the surface atoms of the GaAs slabs. The blue circles represent the As atoms and the red circles the Ga atoms. The intensity of the position distribution is indicated by the color bar. The position distributions on the (100) and (110) surfaces are normalized to the maximum of the distribution on that surface over all the Cs densities.	92
5.4	(a) Work function reduction ($\Delta\langle W \rangle$) as a function of Cs surface density for the GaAs(100) and the GaAs(110) surfaces. The experimental values[91,93] agree well with those calculated using DFT. Chemical potential of adsorbed Cs as a function of Cs surface density for (b) the GaAs(100) and (c) the GaAs(110) surfaces. The experimental values[94,95] are also presented.	94
6.1	Trajectory of the electron in a longitudinally varying magnetic field traveling from A to B. The guiding center follows the magnetic field line. The radius of gyration reduces and the transverse energy increases with increasing magnetic field.	102
6.2	Cross-section of the model of the energy analyzer. Corrector coils used to correct for the misalignments of the coils with the energy analyzer axis are not shown.	106
6.3	(a) Cross section of the gun electrodes, (b) Cross section of the RFA electrodes, (c) Potential and κ_1 on the axis in the gun calculated using POISSON SUPERFISH. For this calculation the potential in the emitter surface was set to $V_e = -7.63$ V, the potential on the pierce and marking electrode surface was set to $V_m = -8.13$ V and the potential on the surface of the accelerating electrodes was set to $F_c = -4.5$ V. Note that $\kappa_1(z_m) < 0.01\text{V/mm}^2$, where $z = z_m$ is the point of maximum potential barrier. (d) Potential and κ_1 on the axis in the RFA calculated using POISSON SUPERFISH. For this calculation the potential on the surface of the shield, pinhole and collector was set to $F_c = -4.5$ V and the potential on the retarding electrode surface was set to $V_r = -8.13$ V. Note that $\kappa_1(z_r) < 0.01\text{V/mm}^2$, where $z = z_r$ is the point of maximum potential barrier. $\kappa_1(z)$ is the negative of the second derivative of the electrostatic potential on axis w.r.t. z as shown in section IV B.	107

6.4	(a) a typical electrostatic potential and longitudinal magnetic field setup on axis of the analyzer. (b) evolution of a hypothetical square-shaped, uniform electron distribution as it propagates through the energy analyzer at various locations (1-4) shown in figure 6.4a.	108
6.5	Measurements from a NEA-GaAs photoemitter under 780 nm illumination. (a) $N_1(\epsilon_m, \epsilon_r)$ (b) 2-D energy distribution, $N(W_{ e}, W_{\perp e})$ (c) Longitudinal energy distributions at the retarding electrode for different α (d) The values of $\langle \epsilon_r \rangle$ for various values of α are obtained from figure 6.5c. MTE can be calculated as the negative slope of $\langle \epsilon_r \rangle$ vs. α	114
6.6	Peak defining the analyzer resolution. Blue solid curve ($\sigma = 5.7$ meV) is measured for the analyzer described in this paper. The black dashed curve ($\sigma = 17$ meV) is the curve obtained by Hoppe <i>et al</i> [117].	118
B.1	(a) Structure of the QW sample. (b) Profile of the conduction band for the QW structure as calculated from the schrodinger-poisson solver[1] along with the Cs barrier.	130
B.2	Transmission energies for the QW shows in figure B.1. The different curves are obtained by changing the thickness of the various layers in the QW by ± 3 Å. This uncertainty can cause a spread of about 20 meV in the resonant tunneling energy.	131
B.3	(a) Structure of the SL sample. (b) Band structure for the SL structure. k is the bloch wave vector and L is the lattice spacing of the SL structure	132
B.4	Spectral response of the quantum well (QW), super-lattice (SL) and p -doped GaAs samples. A, B, C and D indicated the features in the spectral response corresponding to the various bands and transmission energies in the band structures. The two wavelengths (780 nm and 690 nm) used to measure the energy distribution are also indicated. The kinks in the spectral response curves in the 2.1-2.3 eV range are an artifact of the measurement caused by the intense emission lines of the Hg lamp.	134
B.5	2-D energy distributions of (a) QW sample with 780 nm laser, (b) QW sample with 690 nm laser, (c) SL sample with 780 nm laser and (d) SL sample with 690 nm laser. The feature marked by (A) is a glitch in data taking and should be ignored.	136

CHAPTER 1

INTRODUCTION

1.1 Photoinjectors and photocathodes

Photoinjectors are the brightest known sources of bunched electron beams. A photoinjector is essentially a photoemissive material (called photocathode) placed in a DC or RF electric field[2]. Electron bunches are extracted from the photocathode using a pulsed laser (typically in the IR to UV wavelengths) and are accelerated in the electric field to form an electron beam. Electron beams obtained from photoinjectors enable a wide range of applications.

Electron beams from photoinjectors power most, modern-day, large (km) scale, electron accelerators. These include 4th generation light sources based on energy recovery linacs (ERL)[3] or free electron lasers (FEL)[4], electron colliders used for high energy physics experiments, electron beam based hadron coolers[5] used to increase the brightness of hadron beams and sources of intense gamma rays based on inverse Compton scattering[6]. The performance of all these applications is limited by the brightness of the electron beam supplied by the photoinjector.

The maximum beam brightness per bunch that can be obtained from a photoinjector depends only on the electric field at the cathode and the mean transverse energy (MTE) of the electrons emitted from the photocathode[7] and is given by

$$B_n = \frac{m_e c^2 \epsilon_0 E_{\text{cath}}}{2\pi \text{MTE}} \quad (1.1)$$

where m_e is the electron mass, c is the speed of light, ϵ_0 is the dielectric constant

and E_{cath} is the electric field at the cathode. The brightness is directly proportional to the electric field and inversely proportional to the MTE of electron emitted from the photocathode. The MTE is defined as $\text{MTE} = \frac{1}{2}m_e\langle v_x^2 + v_y^2 \rangle$, where, v_x and v_y are the velocities in the transverse directions.

On a smaller (few meters) scale, electron beams obtained from photoemission guns are used for ultra-fast electron diffraction (UED) [8, 9]. This technique allows imaging of dynamic processes in crystalline structures with a sub-100 femtosecond time resolution. The transverse coherence length of the electron beam is the important figure of merit with regards to this technique. The maximum size of the crystal unit cell for which the diffraction pattern can be resolved is set by the transverse coherence length given by

$$L_{\perp} = \lambda \frac{\sigma_{e,x}}{\epsilon_{n,x}}. \quad (1.2)$$

where $\lambda = \frac{\hbar}{m_e c}$ is the reduced Compton wavelength, $\sigma_{e,x}$ is the rms size of the electron beam at the sample and $\epsilon_{n,x}$ is the normalized transverse emittance. The emittance is the volume occupied by the beam in phase space and the normalized transverse emittance is given by $\epsilon_{n,x} = \sigma_{l,x} \sqrt{\frac{\text{MTE}}{m_e c^2}}$ where $\sigma_{l,x}$ is the rms laser spot size determined by the required charge per bunch for the UED application. Thus, the emittance can be reduced and the transverse coherence length can be increased by reducing the MTE of electrons from the photocathode.

The theoretical lower limit to the MTE is given by the disorder induced heating of electrons after they are emitted from the photocathode and is in the 1-2 meV range for most applications[10]. Most cathode materials used today give a MTE in the 100 meV - 1 eV range, which results in transverse coherence lengths of less than 1 nm, limiting the use of UED to metallic or small inorganic crystals. However, achieving a MTE of less than 10 meV will result in transverse

coherence lengths of ~ 10 nm allowing imaging the dynamic processes in large, complicated protein crystals with a sub-100 femtosecond time scale.

Reducing the MTE of electrons obtained from photocathodes can greatly increase the beam brightness from photoinjectors and improve the performance of a wide range of applications and also enable new ones.

1.2 Photocathode requirements

For practical use in photoinjectors, photocathodes need to satisfy several requirements. Along with low MTE, an ideal photocathode must have a high ($> 1\%$) quantum efficiency (QE) in the visible light, a quick ($< 1\text{-}2$ ps) response time, must have a large operational lifetime and must be robust to vacuum conditions. These expectations are often conflicting and to date, no material exists that satisfies all these requirements; trade-offs need to be made[11].

As described in the previous section, a low MTE is important to improve the performance of most applications of photoinjectors. The QE sets the specifications of the drive laser. For applications which require several 10s of mA beam currents (eg. ERLs or electron coolers of hadron beams) the QE requirements are more stringent. For such applications, the cathode QE must be greater than 1% in visible light[12] in order to have practically achievable laser requirements. However, for low ($< 100 \mu\text{A}$) current applications (eg. FELs or UED), several orders of magnitude smaller QE in the visible or UV range suffices. A quick response time of less than 1 ps is required for most applications to avoid an undesirable time structure in the emitted electron bunch[7]. Long operational lifetime and robustness to vacuum conditions are required for practical applica-

tion.

Very often the various requirements of a photocathode are conflicting and appropriate photoemissive materials and laser wavelengths need to be chosen to best suit the application. For example, GaAs activated using Cs and NF_3 can give a low MTE of 25 meV in the infrared wavelengths with response time larger than 100 ps making it useless for ultrafast accelerator applications. However, the same cathode in green light gives response time of less than 2 ps but has a much higher MTE of 120 meV[13].

An important research direction in accelerator technology is to engineer photocathode materials that will satisfy all the photocathode requirements and develop an ideal photoathode. Efforts in several directions which utilize effects of plasmonics[14], metal-oxide thin films[15, 16], layered semiconductor structures[17] etc. are underway. However, an ideal photocathode still remains a dream.

1.3 Challenges in ultra-low energy photoemission

For any photoinjector, a photocathode and incident laser wavelength combination that gives a minimum MTE after satisfying all the criteria of QE, response time and longevity is optimal. In general, MTE is proportional to the excess energy of excited electrons[18]. The excess energy is defined as the difference between the incident photon energy and the work function. Hence, to minimize the MTE, photocathode-laser wavelength combinations of excess energy less than 1-2 eV are generally chosen[11]. This results in ultra low-kinetic energy (< 1 eV) of the photoemitted electron.

The complicated emission physics of these low kinetic energy electrons is a poorly understood topic. The complications arise in both theoretical and experimental aspects of the problem.

In angle resolved photoemission spectroscopy (ARPES) the transverse momentum of photoemitted electrons is measured and conservation of transverse crystal momentum is used to deduce the band structure of materials[19]. In this technique, the kinetic energy of the emitted electrons is greater than a few eV, making their de Broglie wavelength well below the nm scale. In such a case, the translational symmetry in the transverse direction and hence the conservation of transverse momentum holds true[19]. However, at kinetic energies less than 1 eV, the de Broglie wavelength of the emitted electrons can be several nm long. In such a case, surface defects, surface reconstructions, work function non-uniformities and scattering with phonons and plasmons cause the breaking of transverse translational symmetry and hence transverse crystal momentum is not necessarily conserved during emission. These momentum conservation breaking effects along with a higher sensitivity of low energy electrons to surface non-uniformities make theoretical modeling of low energy photoemission difficult.

The difficulty in theoretical modeling is augmented by difficulty in experimental measurements of the energy and momentum distributions of the emitted electrons. Hemispherical energy analyzers, typically used for ARPES measurements, can measure the complete 3-D energy and angular distributions of emitted electrons with a meV scale resolution. However, they are reliable only for electrons with kinetic energy greater than 1 eV. Most of the electrons emitted from photocathodes have kinetic energies smaller than 0.1 eV. Electron

energy distributions measurements obtained for low kinetic energy electrons using hemispherical analyzers are marred by small stray magnetic fields and work function differences between the cathode and the analyzer, making the energy and angular distribution measurements unreliable. Some energy analyzers based on strong electric [20] and strong magnetic [21] fields have been developed to measure the low electron energy distributions or the MTE [22] reliably to the few tens of meV. However, these measure only the 2-D or 1-D energy distributions and a reliable technique to measure the complete 3-D energy distribution of low energy electrons has not been realized to date.

Despite decades of research, ultra-low energy photoemission remains poorly understood due to the difficulties of theoretical modeling and obtaining consistent experimental data.

1.4 Negative electron affinity III-V semiconductor photocathodes

Commonly used photocathode materials include metals like Cu, Mg, Pb and Nb and semiconductors like CsTe, alkali-antimonides[11] and III-V semiconductors activated to negative electron affinity (NEA).

A monolayer of Cs along with a monolayer of an oxidizing species like O₂ or NF₃ can reduce the work function of III-V semiconductors to an extent that the vacuum level goes below the bulk conduction band minima (CBM)[23]. Such a condition is called as NEA.

Among all III-V semiconductors and their alloys, GaAs is most widely used

as a photocathode because of its easy availability and its sensitivity to near infrared-visible region of the spectrum. NEA-GaAs has been used for decades as an infrared sensor and image intensifier in infrared imagery and night vision technology[23, 24, 25, 26]. NEA-GaAs is also one of the best known sources of electrons for photoinjectors. It demonstrates a QE greater than 10%, a short response time and a MTE of 120 meV in green light[13]. In the infrared regime, MTE as low as 25 meV has been demonstrated. It is also the best source of spin-polarized electrons[27].

Photoemission with visible light from NEA-GaAs is best explained using Spicer's three-step model - electron excitation from valance band to conduction band; transport of electrons excited into the conduction band to the surface; and emission from the surface into vacuum[28]. Due to the excellent knowledge of the band-structure, electron transport and light absorption properties of GaAs the first two steps of excitation and transport can be modeled accurately[29]. However, despite being studied for decades and being widely used, the last step of emission into vacuum is not well understood[29].

Owing to the small effective mass of electrons in the Γ -valley of GaAs and the conservation of transverse momentum, the electrons should be emitted in a narrow cone of less than 30° about the surface normal[30] and demonstrate very small MTE of less than 20 meV in green light. However, reliable measurements demonstrate a much higher MTE of 120 meV[13]. The cause of this discrepancy is thought to be due to some form of scattering at the surface during emission. The nature of this scattering remains poorly understood.

The possibility of a dramatic reduction in MTE due to the narrow-cone effect makes NEA-GaAs interesting from the point of view of low energy photoemis-

sion. Furthermore, the physical crystal structure and first two steps of electron excitation and transport are well understood in GaAs. This makes it an excellent candidate for the study of basic photoemission physics.

1.5 Thesis outline

This thesis investigates the physics of low energy photoemission from NEA III-V semiconductor cathodes for applications in photoinjectors. It is a compilation of the ‘first author’ publications of the author. Chapter one and seven provide an introduction and the summary of this work, respectively. Chapters 2 to 6 are based on the publications of the author [29, 17, 31, 21, 32].

First we explain the photoemission from NEA-GaAs using Monte Carlo electron transport simulation in conjunction with Spicer’s three-step model. Using this approach we have been able to accurately calculate the spectral response, MTE and response time without the use of *ad hoc* parameters. These simulations are extended to layered semiconductor structures and, guided by these simulations, layered cathodes are designed to improve photoemission characteristics. The layered structures are grown using molecular beam epitaxy and the photoemission results are found to be in good agreement with the simulations. The Monte Carlo simulations are detailed in chapter 2, whereas the design and development of the layered structures is presented in chapter 3.

Then we shed light on the structure of the Cs over-layer on GaAs and sources of scattering of electron during emission. In chapter 4 we explain various experimentally observed phenomena regarding Cs over-layer on the GaAs surface using density functional theory calculations. We show that spatial work func-

tion variations on the scale of 100 meV are possible on the GaAs(Cs) surface. In chapter 5 we investigate how spatial work functions variations and sub-nm surface roughness can affect photoemission and show that these may be possible causes for the unexplained surface scattering in NEA-GaAs photocathodes.

Finally we present our efforts to develop low energy photoemission diagnostics to obtain, simultaneously, the longitudinal and transverse energy distributions of emitted electrons. The 2-D analyzer designed and developed exploits the motion of low energy electrons in a strong magnetic field and the principle of adiabatic invariance. An energy resolution of 6 meV rms was demonstrated from this 2-D energy analyzer. Chapter 6 is devoted to the design and development of this analyzer. Appendix A presents an estimate of the energy resolution of the analyzer, while appendix B shows the energy distributions from III-V semiconductor based quantum well and super-lattice structures.

CHAPTER 2

MONTE CARLO CHARGE TRANSPORT AND PHOTOEMISSION FROM NEGATIVE ELECTRON AFFINITY GaAs PHOTOCATHODES

2.1 Abstract

High quantum yield, low transverse energy spread, and prompt response time make GaAs activated to negative electron affinity an ideal candidate for a photocathode in high brightness photoinjectors. Even after decades of investigation, the exact mechanism of electron emission from GaAs is not well understood. Here, photoemission from such photocathodes is modeled using detailed Monte Carlo electron transport simulations. Simulations show a quantitative agreement with the experimental results for quantum efficiency, energy distributions of emitted electrons and response time without the assumption of any ad hoc parameters. This agreement between simulation and experiment sheds light on the mechanism of electron emission and provides an opportunity to design novel semiconductor photocathodes with optimized performance. Much of the content of this chapter was previously published in Ref. [29].

2.2 Introduction

The need for a bright electron beam is well established in the fields of x-ray science, electron diffraction and electron microscopy. Photoinjectors are the brightest known sources of electrons. The ultimate brightness of an electron beam obtained from a photoinjector is limited by the mean transverse energy of the

electrons emitted from the photocathode[7]. An ideal photocathode for use in a photoinjector must have a high quantum efficiency (QE), low mean transverse energy (MTE), a quick response time and a good operational lifetime. Despite its extreme sensitivity to vacuum conditions GaAs activated to negative electron affinity (NEA) with Cs/O or Cs/NF₃, remains an excellent photocathode due to its high QE in the visible/near infrared range and low MTE[11].

Photoemission from NEA-GaAs can be best explained using Spicer's 3-step photoemission model[28]. According to this model photoemission from NEA-GaAs can be divided into 3 steps:

1. Optical excitation of electrons from valence band to conduction band.
2. Transport of excited electrons to the surface.
3. Emission of electrons from the surface.

Traditionally, it has been assumed that the electrons excited into the conduction band thermalize very quickly to the bottom of the conduction band and the transport is given simply by the thermal diffusion equation[28, 23, 33]. This assumption holds only for infrared optical excitation or for transmission type cathodes where the response time can be much longer than the time required for thermalization of excited electrons, which is on a picosecond scale. Most photoinjectors require a picosecond scale response time which is comparable to the time required for excited electron thermalization. This is achieved from GaAs cathodes by excitation with green or shorter wavelength light. In this case most of the emitted electrons are not thermalized and the traditional approach of modeling the transport using the diffusion equation fails. Specifically, the energy distribution and response time, both of which important for the operation of photoinjectors, predicted by the diffusion theory are very different from the

observed values. Resolution of this problem calls for a more intricate modeling of electron transport during photoemission.

In the past, a Monte Carlo based scheme of modeling hot electron transport during photoemission has been suggested[23] and implemented[34]. This scheme takes into account the interaction of electrons with lattice phonons and other charge carriers by assuming a mean free path and a crudely defined energy loss interaction. More detailed Monte Carlo based attempts to model transport during photoemission have been made by Spicer *et al.* [35] Their model assumes thermalized electrons in the bulk and considers some electron phonon interactions only in the band bending region (BBR) very close to the surface. These assumptions limit the applicability of these simulations to certain transmission cathodes or to longer wavelength infrared optical excitation.

Over the years, very detailed electron transport modeling that incorporates all the important scattering processes using a Monte Carlo technique has been developed for the bulk III-V semiconductors and applied to sub-micron electronic devices[36, 37, 38, 39]. In this paper, we report a photoemission simulation which uses this detailed Monte Carlo electron transport model in the bulk and near the surface to explain photoemission from GaAs based photocathodes. Such a detailed simulation of the photoemission process allows us to explain the experimental data without the assumption of any ad hoc parameters and resolves many discrepancies between theory and experiments.

Such a simulation can also be extended to study photoemission from other III-V semiconductors and to engineer multi-layered structures with graded doping to develop a photocathode with optimized emission properties.

2.3 Model

This simulation is based on Spicer's 3-step model. The three valley model is used to describe the band structure of GaAs. Below we describe the three valley model and the theory and implementation of each of the three steps of photoemission in considerable detail.

2.3.1 Three valley model

Fig. 2.1(a) shows the band structure of the first conduction band and the heavy hole, light hole and split-off valence bands of GaAs. In our simulations we use the three valley model of GaAs. This model assumes the top 3 valence bands (heavy hole, light hole and the split-off) to be spherical and parabolic near the Γ point. The dispersion relation for the valence bands is given by

$$E = -\frac{\hbar^2 \vec{\mathbf{k}}^2}{2m_{eff}}, \quad (2.1)$$

where E is the energy w.r.t. the top of the particular band, $\vec{\mathbf{k}}$ is the wave-vector of the hole, m_{eff} is the effective mass of the hole in that band.

The first conduction band is modeled as a combination of three valleys (the Γ valley, the L valley and the X valley). Electrons excited into the conduction band are assumed to be confined in one of these three valleys. During transport, the electrons can scatter within the same valley or can jump from one valley to the other. Fig. 2.1(b) shows the band structure of GaAs under the three valley assumption. Only one conduction band is taken into consideration.

The Γ and L valleys intersect at an energy of roughly 2.4 eV above the Valence

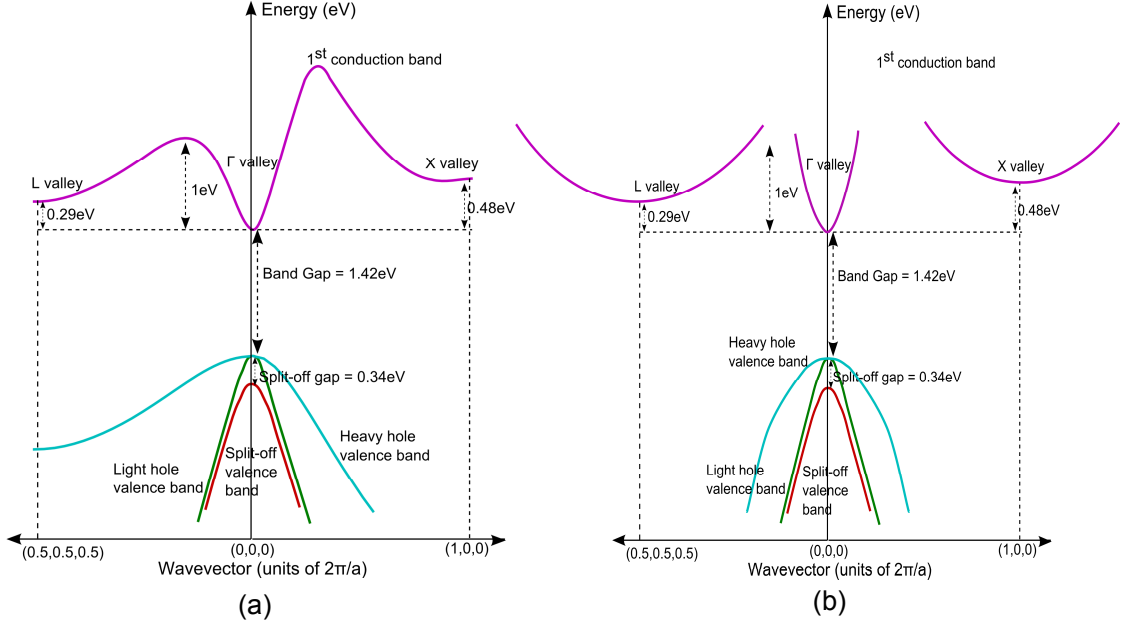


Figure 2.1: (a) Band Structure of GaAs showing the lowermost conduction band and the top 3 (heavy-hole, light-hole and split-off) valence bands. (b) Three valley model for GaAs band structure. The lowest conduction band is modeled as 3 spherical nearly parabolic valleys (Γ , L and X valleys) and the top three valence bands are modeled as spherical parabolic bands about the Γ point.

Band Maximum (VBM). Hence the three valley model holds only up to incident photon of 2.4 eV (green light).

The dispersion relation for each of the valleys can be given by

$$E(1 + \alpha E) = \frac{\hbar^2 \vec{k}^2}{2m_{eff}}, \quad (2.2)$$

where E is the energy w.r.t. the bottom of the valley, \vec{k} is the wave-vector of the electron w.r.t. the wave-vector at the valley bottom and m_{eff} is the effective mass of the electron in that valley and α is the non-parabolicity factor. The values of the effective masses and non-parabolicity factors used in this simulation are listed in Table 2.1

It should be noted that the L and X valleys are in fact ellipsoidal and have different effective masses in the longitudinal and transverse directions. In the present work we ignore this fact and assume the mass to be the density of states effective mass[40] for calculating the scattering rates and the conductivity effective mass[41] for the band structure, transport and emission calculations.

For intrinsic GaAs at room temperature, the band gap E_{g0} is taken to be 1.42 eV. The band gap E_g at higher p -doping is given by[41]

$$E_g = E_{g0} - \frac{3e^2}{16\pi\epsilon} \sqrt{\frac{e^2 N}{\epsilon k_B T}}, \quad (2.3)$$

where N is the p -doping density, ϵ is the dielectric constant of GaAs, k_B is the Boltzmann constant and T is the temperature. Any other change to the band structure (eg. formation of impurity bands or band tails) due to heavy doping has been ignored.

Symbol	Description	Value
Masses		
m_e	mass of electron in vacuum (kg)	9.109×10^{-31}
m_Γ	effective mass in Γ valley[36]	$0.067 m_e$
m_{Ldos}	density of states effective mass in L valley[36]	$0.55 m_e$
m_{Xdos}	density of states effective mass in X valley[36]	$0.85 m_e$
m_{Lcond}	conductivity effective mass in L valley[41]	$0.11 m_e$
m_{Xcond}	conductivity effective mass in X valley[41]	$0.27 m_e$
m_{hh}	effective mass in the heavy hole valence band[42]	$0.51 m_e$
m_{lh}	effective mass in the light hole valence band[42]	$0.082 m_e$
m_{so}	effective mass in the split-off valence band[40]	$0.15 m_e$
Non-parabolicity factors		
α_Γ	non-parabolicity factor for the Γ valley[36] (1/eV)	0.64

α_L	non-parabolicity factor for the L valley[43] (1/eV)	0.461
α_X	non-parabolicity factor for the X valley[43] (1/eV)	0.204
3-Valley model energies		
E_{g0}	Intrinsic band gap at room temperature[40] (eV)	1.42
E_{so}	Split-off energy gap[40] (eV)	0.33
$E_{\Gamma L}$	Gap between minima of Γ and L valleys[40] (eV)	0.29
$E_{\Gamma X}$	Gap between minima of Γ and X valleys[40] (eV)	0.48
Dielectric constants		
ϵ_s	Static dielectric constant for GaAs[44]	13.18 ϵ_0
ϵ_∞	High frequency dielectric constant for GaAs[40]	10.89 ϵ_0
Acoustic deformation potential		
$\Xi_{d\Gamma}$	Acoustic deformation potential for Γ valley[43] (eV)	7.01
Ξ_{dL}	Acoustic deformation potential for L valley[43] (eV)	9.2
Ξ_{dX}	Acoustic deformation potential for X valley[43] (eV)	9.0
Electro-mechanical Coupling constants		
K_{av}^2	Electro-mechanical coupling constant[44]	0.00252
Optical intervalley deformation potential		
$D_{\Gamma L}$	Γ to L valley scattering[43] (eV/m)	10×10^{10}
$D_{\Gamma X}$	Γ to X valley scattering[43] (eV/m)	10×10^{10}
D_{XL}	X to L valley scattering[43] (eV/m)	5×10^{10}
D_{LL}	L to L valley scattering[43] (eV/m)	10×10^{10}
D_{XX}	X to X valley scattering[43] (eV/m)	7×10^{10}
Optical intervalley phonon energies		
$\hbar\omega_{\Gamma L}$	Γ to L valley scattering[43] (meV)	27.8
$\hbar\omega_{\Gamma X}$	Γ to X valley scattering[43] (meV)	29.9

$\hbar\omega_{XL}$	X to L valley scattering[43] (meV)	29.3
$\hbar\omega_{LL}$	L to L valley scattering[43] (meV)	29
$\hbar\omega_{XX}$	X to X valley scattering[43] (meV)	29.9
Number of equivalent valleys for intervalley scattering		
$Z_{\Gamma L}$	Γ to L valley scattering[43]	4
$Z_{\Gamma X}$	Γ to X valley scattering[43]	3
$Z_{X\Gamma}$	X to Γ valley scattering[43]	1
$Z_{L\Gamma}$	L to Γ valley scattering[43]	1
Z_{XL}	X to L valley scattering[43]	4
Z_{LX}	L to X valley scattering[43]	3
Z_{LL}	L to L valley scattering[43]	3
Z_{XX}	X to X valley scattering[43]	2
Longitudinal optical phonon energy		
$\hbar\omega_{lo}$	Longitudinal optical phonon energy[43] (meV)	35.36
Physical parameters for GaAs		
ρ	Mass density[36] (kg/m ³)	5320
v_s	Speed of sound[36] (m/s)	5240

Table 2.1: List of symbols and values used

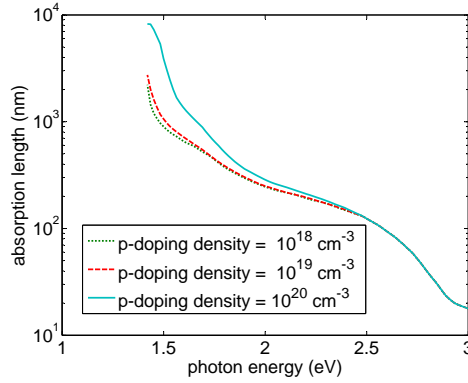


Figure 2.2: Absorption length vs photon energy for various doping levels as calculated by Perera *et al.*[47]. It can be seen that GaAs is nearly transparent to photon energies less than 1.4eV (band-gap).

2.3.2 Excitation

Light incident on GaAs surface decays exponentially into the surface. The intensity of light at a distance x beneath the GaAs surface is given by

$$I = I_0 \exp(-x/a), \quad (2.4)$$

where a is the absorption length. We assume that excitation of electrons from the valence band to the conduction band is the only dominant light absorption process [45, 37]. The only process considered is a two particle process in which one valence band electron interacts with only one photon and gets excited to the conduction band. All higher order processes involving multiple particles are ignored. Inter-valence band transition rates are also assumed to be negligible compared to valence band to conduction band rate for photon energies exceeding the band gap.

Doping dependent absorption length is calculated using the model developed by Perera *et al.*[46, 47] Fig. 2.2 shows the absorption length vs. photon

energies at various doping levels.

Since the photon has a negligible momentum compared to the crystal momentum of the electron, the crystal momentum of the electron is assumed to remain constant during transition. This results in a vertical (or direct) transition on the band diagram. Non-vertical (indirect) transitions require the involvement of a phonon making it a 3 particle transition process. The probability indirect transitions is small and these transitions are ignored. Fig. 2.3 shows transitions that are allowed from the three valence bands to the Γ valley in the conduction band. Direct transitions to other valleys are not possible with photons of energies less than 2.4 eV (the maximum energy for which the three valley model is valid).

The energy, ΔE_c ¹ (w.r.t. the conduction band minimum (CBM)), of the electron excited into the Γ valley with a photon of energy $\hbar\omega$, is calculated by equating the energy difference between the initial and final state of the electron to the energy of the photon[48].

$$\begin{aligned}
 \Delta E_c &= \xi_1 - \Delta E_h, & (2.5) \\
 \Delta E_h &= \frac{\xi_2}{2\alpha_\Gamma} \left(1 - \left(1 - \frac{4\alpha_\Gamma \xi_1 (1 + \alpha_\Gamma \xi_1)}{\xi_2^2} \right)^{1/2} \right), \\
 \xi_2 &= 1 + \frac{m_h}{m_\Gamma} + 2\alpha_\Gamma \xi_1, \\
 \xi_1 &= \hbar\omega - \Delta E,
 \end{aligned}$$

where m_h is the effective mass in the valence band from which the electron was excited and E_h is the initial energy of the electron below the VBM for the particular valence band. For the heavy hole and the light hole bands ΔE is equal to E_g (the band gap), whereas for the split-off band $\Delta E = E_g + E_{so}$. The fraction of electrons excited from a particular valence band is proportional to the product

¹The expression in [48] has a typographical error.

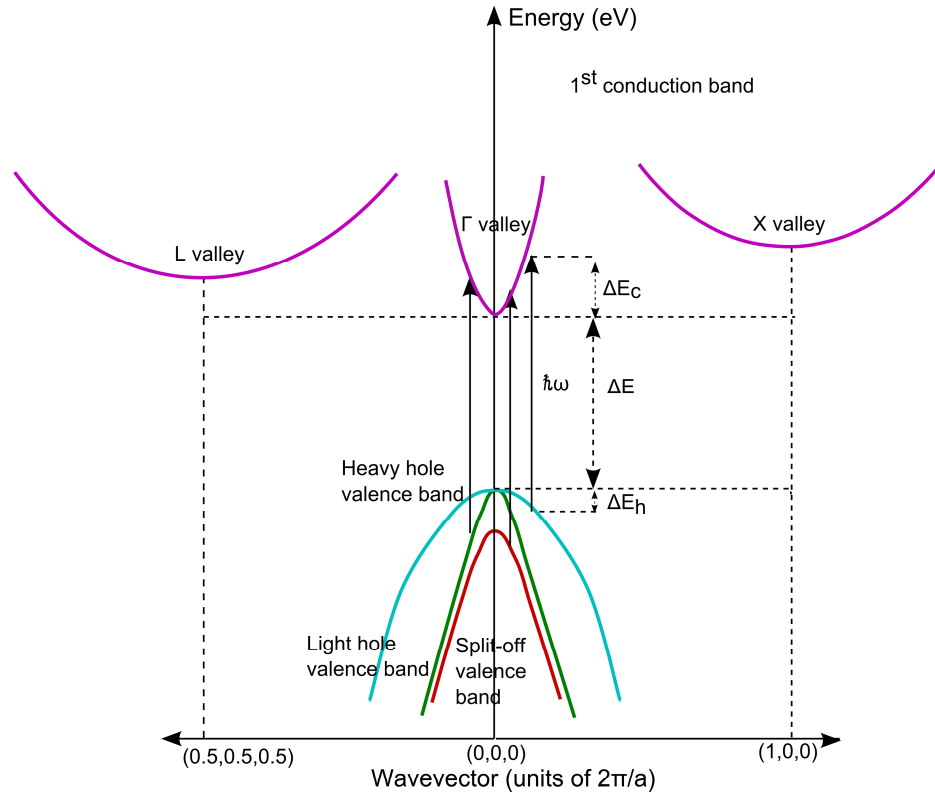


Figure 2.3: Electron excitation from top 3 valence bands to the lowest conduction band. Only direct (vertical) transitions are shown. Indirect, inter-valence band and multi-photon transitions have been ignored.

of the density of states in the initial and final position (in the energy-wave-vector diagram) of the electron.

According to Eq. 2.5 it would be impossible for the photons with energy less than E_g to excite electrons. Although experimental spectral response shows little emission taking place even below the energy gap obtained from Eq. 2.3. This is probably due to the effects of high doping like formation of impurity bands, that are not considered in Eq. 2.3. Electrons excited by photons with energy less than the band gap are assumed to have a very small initial energy of 5 meV in the conduction band right after excitation. The initial energy of the

electrons excited by low energy photons does not affect the output so long as it is smaller than 20 meV as nearly all electrons excited by low energy photons thermalize before they reach the surface.

The number of electrons excited at a particular depth beneath the surface is proportional to the intensity of light at that location and decays exponentially with a decay constant equal to the inverse absorption length. Thus for an excitation with green photons, most of the electrons are excited within 200 nm from the surface, whereas for an infrared excitation a significant number of electrons are excited as deep as 1 μm beneath the surface.

The incident light pulse is assumed to be a delta function in time. Also the time required for the excitation to take place is assumed to be negligible.

2.3.3 Conduction band electron transport

The simulation tracks electrons excited into the conduction band in both real space and k-space using semi-classical equations of motion given below

$$\begin{aligned} \hbar \frac{d\vec{\mathbf{k}}}{dt} &= -e(\vec{\mathbf{E}} + \vec{\mathbf{v}} \times \vec{\mathbf{B}}), \\ \vec{\mathbf{v}} &= \frac{1}{\hbar} \nabla_{\vec{\mathbf{k}}} E, \end{aligned} \quad (2.6)$$

$$\frac{d\vec{\mathbf{r}}}{dt} = \vec{\mathbf{v}}, \quad (2.7)$$

where E is the energy of the electron, $\vec{\mathbf{k}}$ is the wave-vector, $\vec{\mathbf{v}}$ is the group velocity of the electron, $\vec{\mathbf{r}}$ is the position of the electron and $\vec{\mathbf{E}}$ and $\vec{\mathbf{B}}$ are the external electric and magnetic fields applied to the electron respectively. In this section on bulk electron transport and calculation of scattering rates, all electron energies and wave-vectors are w.r.t. those of the valley bottom in which the electron

exists. The Velocity-Verlet algorithm[49] is used as an integrator to update the wave-vectors, velocities and positions of electrons. It is assumed that the charge density is small enough that the fields from other charged particles can be ignored. Scattering of electrons with phonons, charge carriers and impurities is taken into account using an ensemble Monte Carlo technique[36, 39]. Scattering rates are calculated using the Fermi's golden rule. The scattering matrix due to a perturbation H' to the hamiltonian of the lattice is given by

$$S(\vec{\mathbf{k}}, \vec{\mathbf{k}}') = \frac{2\pi}{\hbar} |\langle \vec{\mathbf{k}}' | H' | \vec{\mathbf{k}} \rangle|^2 \delta(E_{\vec{\mathbf{k}}'} - E_{\vec{\mathbf{k}}} \mp E_0), \quad (2.8)$$

where $\vec{\mathbf{k}}$ and $\vec{\mathbf{k}}'$ are the wave-vectors of initial and final states of the scattered electron, $E_{\vec{\mathbf{k}}}$ is the energy in the state with wave-vector $\vec{\mathbf{k}}$ and E_0 is the energy gained or lost during the scattering. The total scattering rate $W(\vec{\mathbf{k}})$ due to the perturbation H' is obtained by integrating over all possible final states -

$$W(\vec{\mathbf{k}}) = \frac{\Omega}{(2\pi)^3} \int S(\vec{\mathbf{k}}, \vec{\mathbf{k}}') d\vec{\mathbf{k}}', \quad (2.9)$$

where Ω is the volume of the crystal.

Different scattering processes result in different perturbations H' , giving different scattering rates. Broadly, electron scattering processes can be classified into 3 types[37]:

1. Impurity Scattering.
2. Phonon Scattering.
3. Carrier Scattering.

Each one of these can be classified further depending on the exact nature of scattering. Below we describe each of the scattering processes considered during the simulation and discuss their implementation.

Impurity Scattering

It can be classified into two types:

- a. Scattering with neutral impurities.
- b. Scattering with charged impurities.

Scattering with neutral impurities Most impurities in GaAs are ionized at room temperatures. The scattering effects due to the non-ionized neutral impurities are negligible at room temperatures and shall be ignored in this work. However, this effect can become important at cryogenic temperatures or in semiconductors for which dopant ionization energy is large compared to the wafer temperature and a significant number of neutral impurities exist [44].

Scattering with charged impurities Scattering with ionized impurities can be described using the Brooks-Herring approach, in which electrons scatter off a screened coulomb potential and the perturbation to the hamiltonian is given by

$$H' = \frac{Ze^2}{4\pi\epsilon_s r} e^{-q_s r}, \quad (2.10)$$

where Z is the charge on the impurity, e is the elementary electric charge, ϵ_s is the static dielectric constant and q_s is the inverse screening length[36, 44]. The screening length is calculated using the Thomas-Fermi approach and is given by

$$q_s^2 = \frac{e^2 m_{lh} (3N_{lh})^{1/3}}{\pi^{4/3} \epsilon_s \hbar^2}, \quad (2.11)$$

where m_{lh} is mass of the light holes and N_{lh} is the concentration of the light holes[37, 50]. Only light holes are considered for screening as they are much more mobile than heavy holes[50].

The impurity scattering rate is given by[36]

$$W(\vec{k}) = \frac{2\pi N_I Z^2 e^4 N(E_{\vec{k}})}{\hbar \epsilon_s^2} \frac{1}{q_s^2 (4\vec{k}^2 + q_s^2)},$$

The probability of scattering in an angle between θ and $\theta + d\theta$ is given by[36]

$$P(\theta) d\theta = \frac{\pi N_I Z^2 e^4 N(E_{\vec{k}})}{\hbar \epsilon_s^2} \frac{\sin \theta d\theta}{(2\vec{k}^2 (1 - \cos \theta) + q_s^2)^2}, \quad (2.12)$$

where N_I is the impurity density, also equal to the doping density, $Z = 1$ is the charge on each impurity, $N(E_{\vec{k}})$ is the density of states in the particular valley and θ is the angle between the wave-vectors before and after scattering. The density of states is given by

$$N(E_{\vec{k}}) = \frac{(2m_{eff})^{3/2} \gamma^{1/2}}{4\pi^2 \hbar^3} \frac{d\gamma}{dE_{\vec{k}}}, \quad (2.13)$$

$$\gamma = E_{\vec{k}} (1 + \alpha E_{\vec{k}}). \quad (2.14)$$

Phonon Scattering

It can be classified into the following types:

- a. Acoustic phonon scattering.
- b. Piezoelectric scattering.
- c. Optical phonon scattering.
- d. Polar optical phonon scattering.

Acoustic phonon scattering This is the scattering of an electron within the valley due to absorption or emission of an acoustic phonon. The energy of an acoustic phonon is assumed to be much lower than the thermal energy at room

temperature and hence this process is treated as an elastic process. This process scatters the electron isotropically and the scattering rate is given by[36]

$$W(\vec{\mathbf{k}}) = \frac{2\pi\Xi_d^2 k_B T}{\hbar c_L} N(E_{\vec{\mathbf{k}}}) C_a, \quad (2.15)$$

$$C_a = \frac{(1 + \alpha E_{\vec{\mathbf{k}}})^2 + \frac{1}{3}(\alpha E_{\vec{\mathbf{k}}})^2}{(1 + 2\alpha E_{\vec{\mathbf{k}}})^2},$$

where Ξ_d is the acoustic deformation potential, c_L is the elastic constant of GaAs given by $c_L = v_s^2 \rho$ (v_s is the speed of sound and ρ is the mass density), $N(E_{\vec{\mathbf{k}}})$ is the density of states in the particular valley.

Piezoelectric scattering In crystals whose lattice lacks inversion symmetry, such as those semiconductors with sphalerite or wurtzite structure (but not those with rock salt structure), elastic strain may be accompanied by macroscopic electric fields. This piezoelectric effect provides an additional coupling between the electron and acoustic phonons. This scattering is also assumed to be elastic and isotropic. The scattering rate is given by[44] -

$$W(\vec{\mathbf{k}}) = C_p \left(\log \left(1 + \frac{m_{eff} E_{\vec{\mathbf{k}}}}{\hbar^2 q_s^2} \right) - \frac{1}{1 + \frac{\hbar^2 q_s^2}{m_{eff} E_{\vec{\mathbf{k}}}}} \right),$$

$$C_p = \frac{(e^2 / (4\pi\epsilon_s)) K_{av}^2 k_B T}{\hbar^2 |\vec{\mathbf{v}}|}, \quad (2.16)$$

where K_{av}^2 is the electro-mechanical coupling coefficient and $\vec{\mathbf{v}}$ is the group velocity obtained from Eq. 2.6.

Optical phonon scattering Electrons can scatter from one valley to another by either absorbing or emitting an optical phonon of energy $\hbar\omega$. This is the only significant process that can cause intervalley scattering[44]. The optical phonon

absorption and emission scattering rates from valley i to valley j are given by the following equations

$$\begin{aligned}
W(\vec{\mathbf{k}}) &= \frac{Z_{ij}\pi D_{ij}^2}{\rho\omega_{ij}} \left(n(\omega_{ij}) + \frac{1}{2} \mp \frac{1}{2} \right) N(E_{\vec{\mathbf{k}}'}) F_{ij}, \\
F_{ij} &= \frac{(1 + \alpha_i E_{\vec{\mathbf{k}}})(1 + \alpha_j E_{\vec{\mathbf{k}}'})}{(1 + 2\alpha_i E_{\vec{\mathbf{k}}})(1 + 2\alpha_j E_{\vec{\mathbf{k}}'})}, \\
E_{\vec{\mathbf{k}}'} &= E_{\vec{\mathbf{k}}} \pm \hbar\omega_{ij} - \Delta E_{ij},
\end{aligned} \tag{2.17}$$

where $n(\omega_{ij})$ is the Bose-Einstein distribution for the phonons of frequency ω_{ij} , Z_{ij} is the number of equivalent j valleys an electron in i valley can scatter into, $D_{ij} = D_{ji}$ is the intervalley deformation potential, ρ is the mass density of GaAs, $\omega_{ij} = \omega_{ji}$ is the frequency of the optical phonon and $\vec{\mathbf{k}}'$ is the final wave-vector. Z_{ij} is 1 for scattering to Γ valley, 3 for scattering to X valley from Γ or L valleys, 2 for scattering to X valley from another X valley, 4 for scattering to L valley from Γ or X valleys and 3 for scattering from L to another L valley. This process is assumed to scatter electrons in an isotropic fashion[36].

Polar optical phonon scattering In polar materials the vibrations of oppositely charged atoms give rise to long-range macroscopic electric fields. Interaction of the electrons with these fields produces additional components of scattering called polar optical scattering. Absorption or emission of a polar optical phonon leads to an inelastic intravalley scattering process. The scattering rates

for absorption and emission are given by[44]

$$\begin{aligned}
W(\vec{\mathbf{k}}) &= \frac{e^2 \hbar \omega_{lo}}{4\pi \epsilon_p \hbar^2 |\vec{\mathbf{v}}|} \left(n(\omega_{lo}) + \frac{1}{2} \mp \frac{1}{2} \right) C_o, \\
C_o &= \frac{1}{2} \left(q_s^2 \left(\frac{1}{q_{max}^2 + q_s^2} - \frac{1}{q_{min}^2 + q_s^2} \right) \right), \\
&\quad + \log \left(\frac{q_{max}^2 + q_s^2}{q_{min}^2 + q_s^2} \right), \\
q_{max} &= \frac{\sqrt{2m_{eff}\gamma(E_{\vec{\mathbf{k}}})}}{\hbar} \left(1 + \sqrt{1 \pm \frac{\hbar \omega_{lo}}{E_{\vec{\mathbf{k}}}}} \right), \\
q_{min} &= \pm \frac{\sqrt{2m_{eff}\gamma(E_{\vec{\mathbf{k}}})}}{\hbar} \left(-1 + \sqrt{1 \pm \frac{\hbar \omega_{lo}}{E_{\vec{\mathbf{k}}}}} \right),
\end{aligned} \tag{2.18}$$

where $\vec{\mathbf{v}}$ is given by Eq. 2.6, $n(\omega_{lo})$ is the Bose-Einstein distribution for the longitudinal optical phonons of frequency ω_{lo} and the effective dielectric constant $\epsilon_p = \left(\frac{1}{\epsilon_\infty} - \frac{1}{\epsilon_s} \right)^{-1}$. The final energy is given by $E_{\vec{\mathbf{k}}'} = E_{\vec{\mathbf{k}}} \pm \hbar \omega_{po}$, where $\vec{\mathbf{k}}'$ is the final wave-vector.

The angle θ between $\vec{\mathbf{k}}'$ and $\vec{\mathbf{k}}$ is given by[39]

$$\begin{aligned}
\cos \theta &= \frac{1 + f - (1 + 2f)^r}{f}, \\
f &= \frac{2 \sqrt{\gamma(E_{\vec{\mathbf{k}}}) \gamma(E_{\vec{\mathbf{k}}'})}}{\left(\sqrt{\gamma(E_{\vec{\mathbf{k}}})} - \sqrt{\gamma(E_{\vec{\mathbf{k}}'})} \right)^2},
\end{aligned} \tag{2.19}$$

where, r is a random number chosen between 0 and 1 and γ is obtained from Eq. 2.14.

Carrier Scattering

The following carrier-carrier interactions are possible:

- a. Electron-hole binary scattering.

- b. Electron-electron binary scattering.
- c. Electron-plasmon scattering.

Electron-hole binary scattering The excited electrons are assumed to interact with holes through binary elastic collisions. The holes are randomly picked from thermalized hole distributions from the heavy hole and the light hole bands. Although the electron-hole collision is elastic the energy of both the electron and the hole changes during collision. This results in a net transfer of energy from the hot electrons to the thermalized holes. The implementation of electron hole binary scattering is described in detail in [48, 51].

Electron-hole scattering is the most important energy reducing mechanism for hot electrons in heavily p -doped GaAs.

Electron-electron binary scattering It is possible to implement this in a fashion similar to electron-hole scattering. Although in a p -doped semiconductor the density of electrons is very small and electron-electron scattering can be ignored.

Electron-plasmon scattering Electrons can interact with the collective density oscillations of the ambient charge carriers (plasmons) caused by the excited electrons. In p -doped GaAs the plasma oscillations of the holes are heavily damped and any interaction with them can be ignored [50]. In n -doped GaAs, this can be an important scattering mechanism and its implementation is described by Tomizawa[36].

Fig. 2.4 shows the scattering rates for various processes in the Γ , L and X

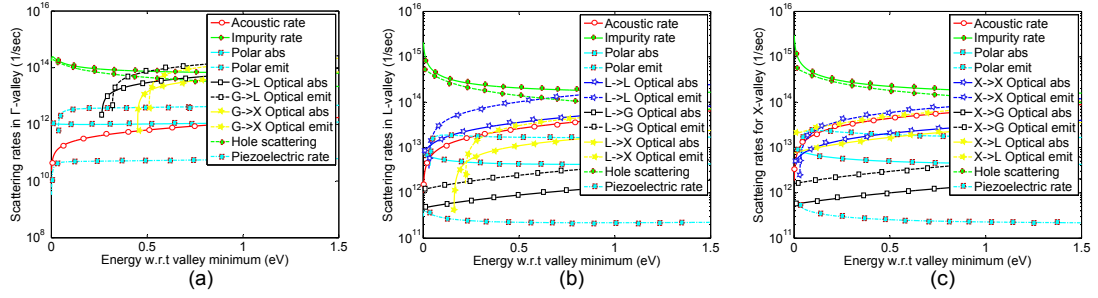


Figure 2.4: Scattering rates for various valleys (a) Γ valley, (b) L valley, (c) X valley. In all valleys, at lower energies, the impurity and hole scattering are the dominant scattering mechanisms, followed by inter-valley optical scattering.

valleys for a p -doping density of 10^{19} cm^{-3} . The parameters used to calculate these rates are given in Table 2.1.

Verification of the conduction band electron transport was performed by comparing the drift velocity predicted by the simulation to the experimentally measured[50] drift velocity at various electric fields and various doping levels. The results of the comparison are shown in Fig. 2.5. The simulations match the experimental results quite well except at high electric fields and low doping level of $1.5 \times 10^{17} \text{ cm}^{-3}$. This discrepancy can be attributed to the L and X valleys being simulated as spherical valleys instead of ellipsoidal valleys. A better match to the experimental results can be obtained by adjusting the effective mass for the L and X valleys to best fit the experimental results [50, 52]. However this assumption does not give a good match to the experimental photoemission spectral response curves and hence isn't used. In this work the density of states effective mass has been used for the calculation of the scattering rates and the conductivity effective mass has been used for calculation of the dispersion relation, velocities and emission. This assumption gives a good fit to the

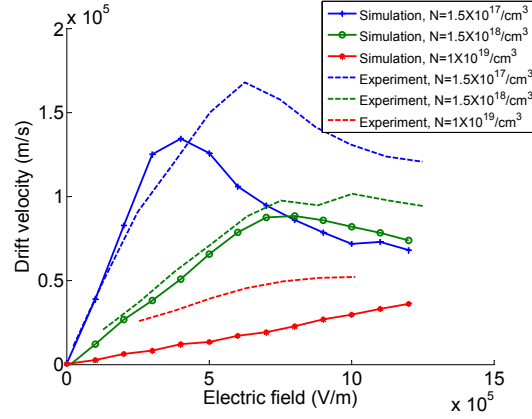


Figure 2.5: Comparison of simulated and experimental[50] drift velocities at different electric fields and p -doping densities of $N=1.5 \times 10^{17} \text{ cm}^{-3}$, $1.5 \times 10^{18} \text{ cm}^{-3}$ and $1 \times 10^{19} \text{ cm}^{-3}$. The main cause of disagreement is the assumption of the L and X valleys being spherical rather than ellipsoidal and the inaccuracy in the screening mechanism.

experimental spectral response (see section 2.4.1).

2.3.4 Treatment of GaAs to vacuum interface and emission

The excited electrons cool as they diffuse in bulk GaAs. Some of these reach the GaAs-vacuum interface. Fig. 2.6 shows the band structure near the GaAs-vacuum interface. The 4 main surface effects that have been considered are:

1. Band bending region.
2. Conservation laws during emission.
3. Surface barrier, image charge and vacuum level.
4. Scattering during emission.

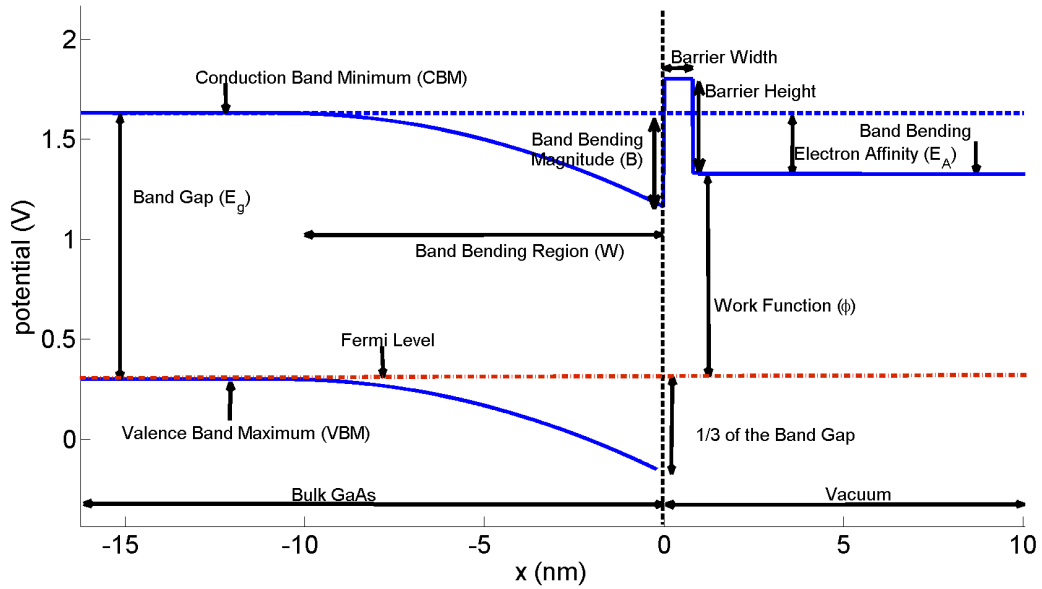


Figure 2.6: Band diagram of GaAs(Cs/F) near the surface for p -doping concentration of $1 \times 10^{19} \text{ cm}^{-3}$. The surface exhibits negative electron affinity condition ($E_A < 0$).

Each of the above effects and their implementation in the emission code is described below.

Band-Bending

The Fermi level in the bulk of heavily p -doped GaAs is close to the (VBM) and is given by Nilsson *et al.* [53] The Fermi level at the surface gets pinned to a different value relative to the VBM due to surface defects. Upon addition of Cs, the surface Fermi level is pinned to one third the band-gap value above the VBM at the surface[54]. This difference between the bulk and surface Fermi levels

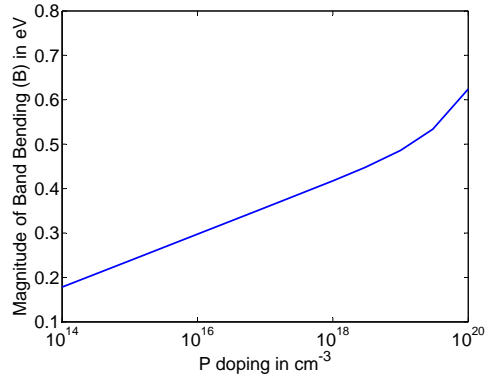


Figure 2.7: Magnitude of band bending vs doping density. The band bending magnitude is given as the difference between the Fermi level to VBM gap in the bulk and at the surface. In the bulk, this gap is determined by the doping level[53] and at the surface this gap is determined by the Fermi level pinning[54].

w.r.t. the VBM causes the valence and conduction bands to bend downwards in energy as one approaches the surface. The magnitude of this bending (B) is given by the difference between the Fermi level to VBM spacing, in the bulk and at the surface (see Fig. 2.6). Fig. 2.7 shows the dependence of B on the doping density. The bending is assumed to be quadratic in nature and the width is given by $W = \sqrt{\frac{2\epsilon_s}{eN} |B|}$ as shown by Sze[55], where ϵ_s is the static dielectric constant in GaAs, e is the elementary electric charge and N is the density of charge carriers. Fig. 2.8 shows the dependence of W on the doping density.

In the simulations, this band-bending is implemented by adding an electric field, acting on the electrons, that causes a change in potential, equal to the change in the VBM. The electrons in the band bending region are treated as semi-classical particles moving under the effect of this field using Eq. 2.6 and undergoing scattering similar to the bulk. Any changes in scattering and quantum effects arising due to the band bending are ignored.

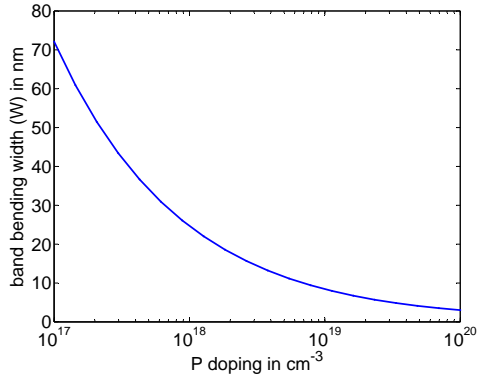


Figure 2.8: Band bending width vs doping density. The band bending width is calculated assuming the formation of a depletion region near the surface due to the electrons donated by the Cs atoms[54,55].

Conservation laws during emission

The two important conservation laws are obeyed during emission from the surface:

- a. Conservation of energy.
- b. Conservation of transverse momentum.

Conservation of energy The energy of the electrons (E) w.r.t. the valley bottom in GaAs is given by the dispersion relation (Eq. 2.2). The energy of an electron in vacuum (E') is given by $E' = \frac{\hbar^2 \mathbf{k}'^2}{2m_e}$ where \mathbf{k}' and m_e are the electron's wave vector and mass in vacuum. Let E_A be the affinity of the surface (vacuum level - bulk CBM) and E_V be the energy of the bottom of the valley w.r.t. the CBM. If E_A is less than zero we say that the surface has an effective negative affinity (see Fig. 2.6). Now the conservation of energy at the surface gives us

$$E + E_V - E_A = E'. \quad (2.20)$$

Conservation of transverse momentum The Hamiltonian of the GaAs-vacuum interface has translational symmetry in the plane of the emission surface. This causes the crystal momentum and hence the wave vector of the electrons in the transverse direction to be conserved during emission. If $\vec{\Lambda}$ is the wave vector corresponding to the valley bottom of the electron, the conservation of transverse momentum results in

$$\vec{\mathbf{k}}_{\perp} + \vec{\Lambda}_{\perp} = \vec{\mathbf{k}}'_{\perp}, \quad (2.21)$$

where the subscript \perp stand for the component in the transverse direction.

Condition for emission In order to be emitted the electron hitting the surface barrier must be able to satisfy both the conservation laws. Emission in vacuum requires that the emitted electron must have a non negative wave vector in the longitudinal direction in vacuum. From Eqs. 2.20 and 2.21, we obtain the longitudinal component of the vacuum wave vector as

$$\vec{\mathbf{k}}'_{\parallel} = \sqrt{\frac{2m_e(E - E_A + E_V)}{\hbar^2} - (\vec{\mathbf{k}}_{\perp} + \vec{\Lambda}_{\perp})^2}. \quad (2.22)$$

If $\vec{\mathbf{k}}'_{\parallel} \geq 0$, the electron can be emitted and removed out of the simulation, or else it is reflected back into the bulk and continues to be tracked and scattered.

If the valley from which the electron is being emitted, is in the direction of the surface normal, then $\vec{\Lambda}_{\perp} = 0$. Otherwise, typically $\vec{\Lambda}_{\perp}^2 \gg \frac{2m_e(E - E_A + E_V)}{\hbar^2}$ making $\vec{\mathbf{k}}'_{\parallel}$ imaginary and thus restricting emission from such valleys. For example, consider a electron in the L-valley $[\frac{1}{2} \frac{1}{2} \frac{1}{2}]$ at a (100) surface. In this case, $\vec{\Lambda}_{\perp}^2 = 0.5 \frac{4\pi^2}{a^2} = 0.6 \text{ \AA}^{-2}$ where $a = 5.6 \text{ \AA}$ is the lattice constant of GaAs. For $E_V = 0.29$ eV and a typical value of $E_A = -0.1$ eV and assuming $E \ll E_V - E_A$ we can calculate $\frac{2m_e(E - E_A + E_V)}{\hbar^2} = 0.05 \text{ \AA}^{-2} \ll \vec{\Lambda}_{\perp}^2$ making $\vec{\mathbf{k}}'_{\parallel}$ imaginary and forbidding

emission from this valley. Emission from this valley will be allowed only when an electron has an energy close to or greater than 1 eV w.r.t the CBM, which is impossible within the boundaries of the three valley model. Thus only Γ and certain X-valley electrons are allowed to emit from the (100) surface.

Another consequence of the conservation laws is the small transverse energy of emitted electrons. Assuming $\vec{\Lambda}_\perp = 0$, the transverse energy in vacuum is given by $E'_\perp = \frac{\hbar^2 \mathbf{k}_\perp^2}{2m_e}$, whereas the transverse energy in the conduction band of GaAs is given by $E_\perp = \frac{\hbar^2 \mathbf{k}_\perp^2}{2m_{\text{eff}}}$. The ratio of the transverse energies in vacuum to the transverse energy in the conduction band of GaAs is then given by $\frac{E'_\perp}{E_\perp} = \frac{m_{\text{eff}}}{m_e} = 0.067$ for Γ valley electrons. For the purpose of the above analytic calculations we assume parabolic bands, but the simulation does take into account the non-parabolicity.

The angle that the emitted electrons make with the surface normal is given by $\theta = \arctan \frac{|\mathbf{k}_\perp^2|}{|\mathbf{k}_\parallel^2|}$. For Γ valley electrons with a negative affinity surface it can be shown that $\theta < 15^\circ$ [30]. This result has also been observed experimentally [30, 26, 56].

Such a narrow cone distribution and a small MTE are also predicted by the simulation. Figs. 2.9 and 2.10 show variation of MTE with electron affinity (E_A) and the angular distribution of emitted electrons for a negative affinity surface ($E_A = -0.1$ eV) respectively. These results are obtained by assuming an initial thermalized distribution of electrons at room temperature in the Γ valley. No scattering or band bending was considered. It must be noted that Figs. 2.9 and 2.10 are presented only to show the effect of the conservation laws during emission and do not include effects of scattering or band-bending. This shows that the presence of the narrow emission cone is a surface emission effect arising

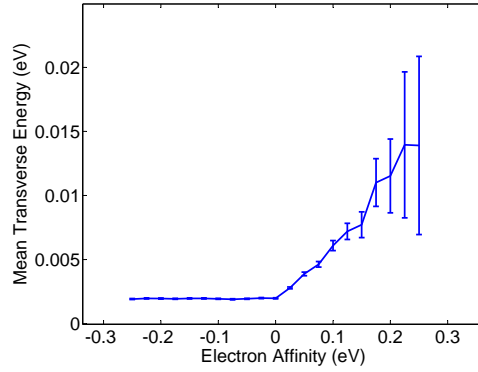


Figure 2.9: Mean transverse energy of emitted electrons using classical step boundary, assuming a thermalized electrons in GaAs, no band bending and no surface barrier.

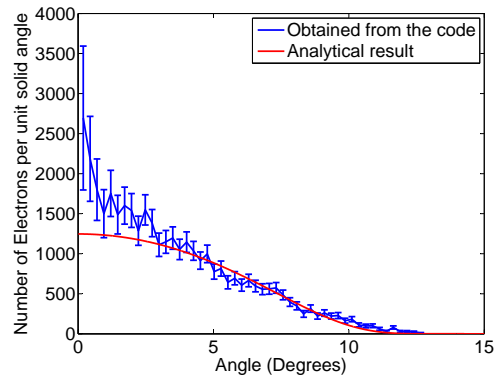


Figure 2.10: Angular distribution of emitted electrons per unit solid angle obtained by the simulation, assuming a thermalized electrons in GaAs, no band bending and no surface barrier compared to the analytic result for the same case[30].

due to the conservation of the transverse crystal momentum and not due to the longitudinal acceleration provided by the surface band bending.

Surface barrier, image charge and vacuum level

At the surface, the electrons experience a barrier which they either have to overcome or tunnel through to get emitted. The exact nature, shape or cause of this barrier is not very well understood. The double dipole effect [57] due to the Cs/O or Cs/F layer at the surface and the image charge effect[58] are two contributors to this barrier. Fisher *et al.*[57] modeled it as a rectangular barrier with height 0.28 eV above the vacuum level and a width of 8 Å by fitting the calculated values of quantum efficiency to the experimental ones. Spicer *et al.*[35] modeled this barrier as a triangular barrier with height of ~4 eV and a much narrower width of 1.5 Å by fitting the energy distribution of emitted electrons. These are two approximations to the barrier that are obtained by fitting the calculated or simulated results to experimental data. Fig. 2.11(a) shows the two barriers for comparison.

The vacuum level lies beyond the barrier and can be changed in the simulation to change the electron affinity of the surface. The vacuum level and the barrier shape are determined by the method of activation, quality of the vacuum during the activation and surface characteristics (cleanliness, orientation and roughness) of GaAs. These parameters are very sensitive and difficult to control and reproduce experimentally. Any external electric field present in the vacuum can also be included in the surface potential.

The electrons which satisfy the energy and transverse momentum conservation conditions for emission get emitted with a probability given by the quantum transmission probability through this barrier. The electrons that don't get transmitted are reflected and continue to drift and scatter within GaAs.

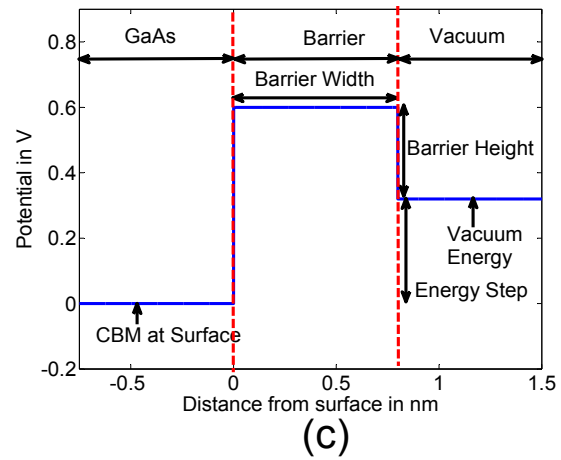
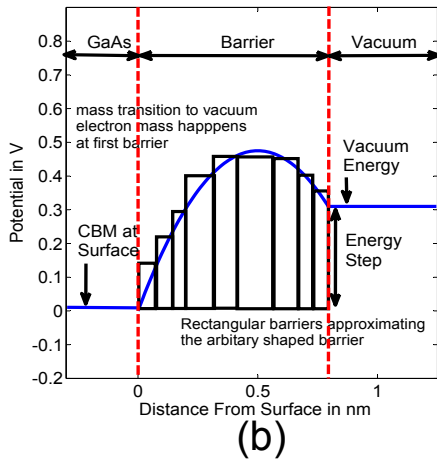
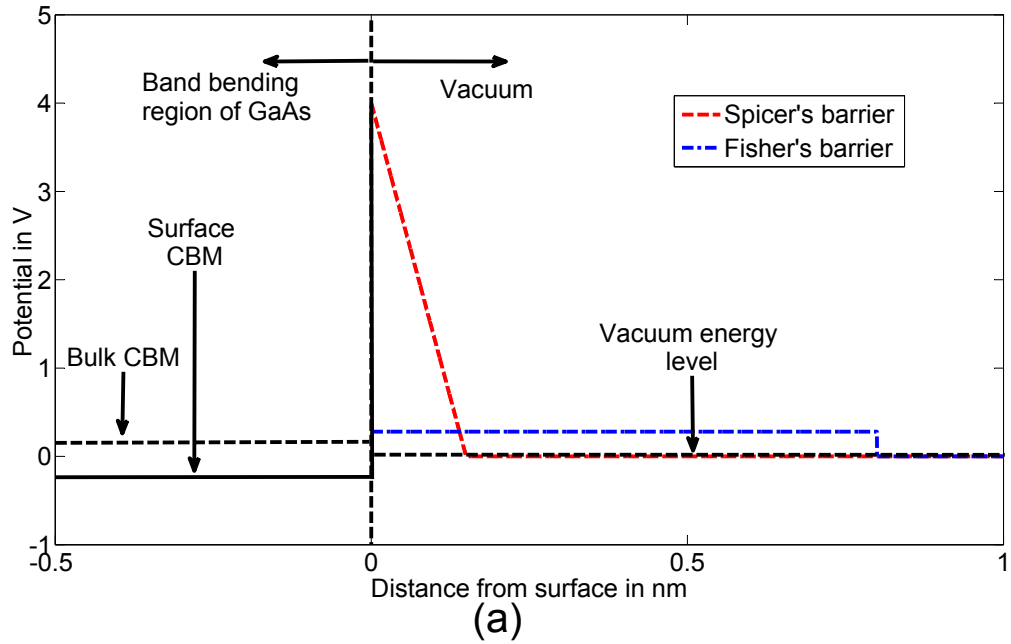


Figure 2.11: (a) Surface barrier predicted by Fisher *et al.*[57] and Spicer *et al.*[35] (assuming a negative affinity of 0.1 eV). (b) Arbitrarily shaped barrier approximated as a series of rectangles to calculate the transmission probability using the propagation matrix approach. (c) Fisher's barrier used to calculate transmission probability in Fig. 2.12.

The transmission probability across the barrier is calculated using the propagation matrix approach [59]. Due to the translational symmetry in the transverse direction, only the longitudinal component of the k-vectors are used to calculate the reflection coefficient. With this propagation matrix implementation one can simulate the surface barrier of any shape by approximating it by a finite number of rectangular barriers as shown in Fig. 2.11(b). The effective mass is assumed to change instantaneously, to the vacuum mass, at the interface of GaAs and the first rectangle of the barrier.

For all the results presented in this paper the rectangular barrier predicted by Fisher *et al.*[57] has been used. This barrier is shown in Fig. 2.11(c). The image charge effect has been assumed to be incorporated within the experimentally determined barrier and has not been included explicitly. All results presented here are performed at zero external electric field. Fig. 2.12 shows the transmission probability for this rectangular barrier as a function of the longitudinal component of the k-vector for various transverse components of the k-vector at an energy step of 0.25 eV (energy difference between the potentials before and after the barrier). The variation with the transverse component of the k-vector is only due to the effective mass change and the non-parabolicity. Without these two, the transmission probability will depend on the longitudinal component alone.

Scattering during emission

The small effective mass in the Γ valley results in a narrow-cone emission and a sub-thermal MTE. Such an effect has been experimentally observed by some [30, 26, 56]. However most [13, 25, 60, 61, 62] measure a MTE that is nearly an order

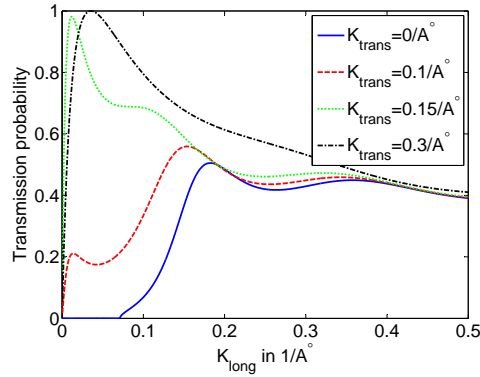


Figure 2.12: Transmission probability vs longitudinal component of k -vector. The result depends on the transverse component of the wave-vector due to the change in the effective mass during emission and the non-parabolic valleys.

of magnitude greater than that predicted by the narrow cone emission. The reason for this discrepancy is unclear. Scattering in the Cs/O layer, variations in the structure of the layer, non-uniform work function due to insufficiently clean surface and surface roughness are possible causes of the discrepancy.

Various attempts to investigate and model the large MTE have been made. Effects on MTE due to surface roughness have been studied[63, 25]. Various emission models have also been investigated[62]. The model implemented in this simulation assumes that electrons lose the emission angle information and are redistributed uniformly in the polar angle during emission. It is assumed that this surface scattering is elastic and the electrons do not lose or gain energy due to this scattering.

Despite its simplicity this surface scattering model gives MTE values comparable to the experimental values as shown in section 2.4.2. It is straightforward to modify the code to include any kind of energy, angle and wave-vector dependent surface scattering. The exact cause of scattering during emission has not

been identified and hence implementing it accurately is not possible.

2.4 Comparison to photoemission experiments

2.4.1 Spectral response

Sample preparation and measurement procedure

A commercially available, 0.5 mm thick, $1 \times 10^{19} \text{ cm}^{-3}$ Zn doped epi-ready GaAs wafer was cleaned with trichloroethylene and acetone. It was then anodized in dilute phosphoric acid, creating an anodized layer about 50 nm thick. Just before the wafer is indium soldered to the puck, the anodized layer is removed using ammonium hydroxide. The sample was then introduced into a vacuum chamber with a base pressure of 5×10^{-11} torr and heated to 620°C in vacuum to remove the oxide layer. Activation was performed by alternate evaporation of Cs and exposure to NF_3 using the yo-yo technique.

Monochromatic light, obtained from a Hg lamp followed by a diffraction grating, was used to measure the spectral response. The activated sample was electrically isolated from the rest of the chamber and biased to -30 V. The current emitted by the sample was measured using a picoammeter. The quantum efficiency (QE) was deduced by measuring the power of the light incident on the sample and the electron current recorded at this incident power.

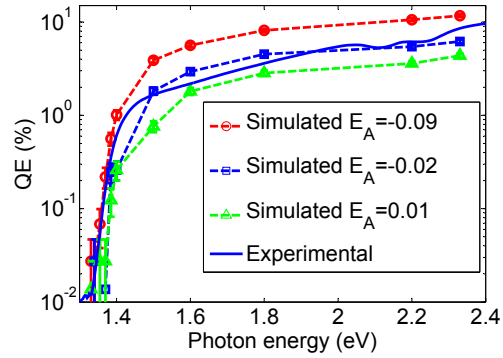


Figure 2.13: Comparison of measured and simulated spectral response. Electron affinity (E_A) is a variable parameter in the simulation. It is seen that the best fit is obtained for $E_A = -0.02$ eV.

Simulation and Experimental results

Fig. 2.13 shows the spectral response measurement along with the results obtained from the simulation for various values of electron affinity. A very close match is obtained between the experimental results and the simulated one with electron affinity of -0.02 eV. The match is remarkable as the simulated results are obtained entirely from the band structure and transport properties of GaAs and no arbitrary scaling parameters have been used. The only uncertain variable is the electron affinity which is deduced to be -0.02 eV by comparing the simulated results to the experiment. We see that the electron affinity was close to zero and only slightly negative. In order to calculate the quantum efficiency, the reflectivity value of GaAs was taken from Ref. [40].

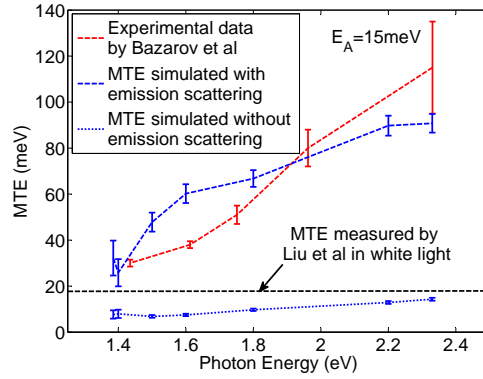


Figure 2.14: Comparison of measured (data by Bazarov *et al.*[13] and data by Liu *et al.*[30]) and simulated MTE with and without surface scattering. Electron affinity is assumed to be 15 meV for simulations.

2.4.2 Mean transverse energy and angular distributions

Fig. 2.14 shows the experimentally measured values of MTE [13] along with those calculated using the simulation with and without the scattering during emission. The electron affinity is assumed to be 15 meV. The MTE predicted by the simulation without scattering during emission is very small (<20 meV) due to the narrow cone effect. MTE deduced from the angular and energy distributions obtained by Liu *et al.*[30], using white light for excitation, is very close to this value. Similar angular distributions have also been observed by others [30, 26, 56].

However, several other measurements of MTE give a much larger value[13, 25, 60, 61, 62]. Fig. 2.14 shows experimental data from Bazarov *et al.* [13] Inclusion of scattering during emission in the simulation (modeled here using the cosine distribution of emitted electrons) causes the rise in the MTE values and gives values comparable to this experimental data.

GaAs thickness	τ_{90} Experimental	τ_{90} Simulation	τ_{80} Simulation
200 nm	4.6 ± 0.7 ps	6.9 ± 0.8 ps	4.7 ± 0.7 ps
400 nm	15 ± 2 ps	25.6 ± 4 ps	16.6 ± 3 ps

Table 2.2: Response time for thin GaAs photocathodes under 1.46 eV excitation. The experimental values in column two are from Aulenbacher *et al.*[33]

The cause for this discrepancy remains poorly understood. To resolve this discrepancy, it is essential to understand the scattering processes involved during emission and their dependence on various factors like the structure of the Cs layer, surface cleanliness, orientation, and roughness.

2.4.3 Response time

Response time, τ_x , is the time required for emission of x percent of the total number of emitted electrons due to an instantaneous incident light pulse. Diffusion theory predicts the response time to be nearly an order of magnitude greater than the experimental values[13] or requires the assumption of ad hoc diffusion constants to explain the experimental data[33]. The simulations presented here predict the response time accurately to within 50% of the experimental value without assuming any ad hoc parameters.

90% response times (τ_{90}) have been measured for thin GaAs cathodes with 1.46 eV infrared excitation [33]. Table 2.2 summarizes the result and compares it to the simulation. The simulation predicts the correct trend but overestimates the value of τ_{90} by approximately 50%. The value of τ_x is very sensitive for larger values of x due to the long emission tail[13]. This sensitivity is demonstrated by the values of τ_{80} predicted by the simulation.

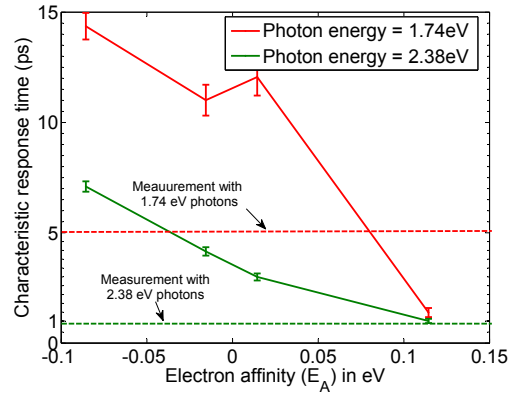


Figure 2.15: Simulated and experimental [13] response times for photon energies of 1.74 eV and 2.38 eV. The simulated values show a variation in the response time with electron affinity, but the electron affinity is unknown for the experimental data.

Simulations also predict a strong dependence of response time on the electron affinity for visible photon energies. Fig. 2.15 shows the characteristic response time (τ_{57})[13] vs electron affinity for various incident photon energies, for thick GaAs samples. Response time of thick (0.5 mm) GaAs samples has been measured for various wavelengths [13]. Neither the quantum efficiency nor the electron affinity for these measurements is known. Nevertheless, Fig. 2.15 shows that the measured response times are within the values predicted by the simulation for a reasonable assumption of electron affinity between 0.1 eV to -0.1 eV.

2.5 Limitations of the simulation

The following limitations of the simulation have been identified:

1. Three valley model limitations: This code is based on the three valley

model of GaAs. This model is valid only up to electron energies of at most 1 eV w.r.t. CBM. This corresponds to a photon excitation energy of 2.4 eV (green light). Further, the simulation assumes the L and X valleys to be spherical instead of ellipsoidal.

2. Quantum self consistency: The simulation is based on a semi-classical picture of the electron. The transport in the band bending region is modeled withing this approximation using an external electric field and quantum transport effects like tunneling and quantum reflection are ignored. These effects are taken into account during emission from the surface. Formation of localized surface states in the band-bending region is also ignored.
3. Abrupt GaAs-Vacuum interface: The simulation assumes that the band structure of bulk GaAs can be used right up to the surface and that the change in effective mass is instantaneous as the electron goes from GaAs to the barrier.

2.6 Conclusion and future work

Our simulation is the first to include the detailed modeling of absorption, 3-band charge transport and emission for activated III-V semiconductor photocathodes and to have demonstrated this level of agreement with experimental data. This Monte Carlo based transport simulation applied to photoemission gives a fundamental insight into the process of photoemission from III-V semiconductors like GaAs activated to low or negative electron affinity. It is successful in explaining various photoemission properties quantitatively using fundamental and well measured properties of GaAs, without relying on ad

hoc parameters. It helps to understand various mysteries regarding the quantum efficiency, energy distributions and response time of photoemission. Although, various questions relating to surface scattering still remain, this simulation helps in understanding the impact of hot electron relaxation and electron transport in the band bending region on various photoemission characteristics.

Such a simulation can, very easily, be extended to other III-V semiconductors and be applied to more complex layered structures with graded doping. This will enable us to engineer III-V semiconductor photocathodes and tune the various photoemission characteristics to optimize them.

This work has been funded by NSF under grant number DMR-0807731, DOE under grant number DE-SC0003965 and DOE-SBIR grant number DE-SC0006246.

CHAPTER 3

LAYERED III-V SEMICONDUCTOR PHOTOCATHODES

3.1 Abstract

Crucial photoemission properties of layered III-V semiconductor cathodes are predicted using Monte Carlo simulations. Using this modeling, a layered GaAs structure is designed to reduce simultaneously the transverse energy and response time of the emitted electrons. This structure, grown by molecular beam epitaxy and activated to negative electron affinity, is characterized. The measured values of quantum efficiency and transverse energy are found to agree well with the simulations. Such advanced layered structures will allow generation of short electron bunches from photoinjectors with superior beam brightness. Much of the content of this chapter was previously published in Ref. [17].

3.2 Introduction

Photoemission-based electron sources can provide extremely bright beams with sub-picosecond time resolution[7]. These sources enable applications such as ultrafast electron diffraction (UED)[8], inverse Compton scattering[6], electron cooling of hadron beams[5], polarized electron beams for colliders, and modern light sources based on free-electron lasers[4] or energy recovery linacs[3].

The photocathodes used in these sources must meet a number of often conflicting requirements: high efficiency; prompt emission (response time); low emittance and longevity. High quantum efficiency (QE) cathodes are desir-

able for applications with high average current or bunch charges. In order to reduce the demands on the drive laser, cathodes with QE values of 1% or greater are desirable[12]. Prompt emission implies that the electrons are emitted quickly after the incident photon pulse arrives at the cathode. Electrons excited deep within a cathode can take many tens of picoseconds to reach the surface and escape into vacuum, producing an undesirable time structure, while sub-picosecond to picosecond time scales are needed for most applications. The emitted electron beam is contained within a phase space volume, known as the emittance[7]. The intrinsic emittance of the beam from a photocathode is determined by the laser beam size and the mean transverse energy (MTE) of the emitted electrons through the relation:

$$\epsilon_{n,x} = \sigma_{l,x} \sqrt{\frac{MTE}{m_e c^2}} \quad (3.1)$$

where $\epsilon_{n,x}$ is the normalized transverse emittance in the x-plane, $\sigma_{l,x}$ is the rms laser spot size, m_e is the electron mass and c is the speed of light. The lower limit to laser spot size is given by the charge per bunch (q) required for the specific application and by the electric field E_{cath} at the cathode as $\sigma_{l,x} \approx \sqrt{\frac{1}{4\pi\epsilon_0} \frac{q}{E_{\text{cath}}}}$, assuming a short duration uniform round laser spot[7]. The value of the MTE, however, depends on the cathode material and can range from 25 meV up to 1 eV[11]. Finally, cathode longevity, or lifetime, implies that the photocathode is robust enough to operate in the environment of the application without significant QE degradation.

Finding a photocathode that simultaneously meets all of these requirements is difficult. For example, GaAs photocathodes have the lowest known MTE of 25 meV for laser excitation near the bandgap, but have poor QE ($\leq 1\%$) and a slow response time[13]. Using a green wavelength excitation on GaAs, the QE is high and the photoemission is prompt, but the MTE is five times worse.

Presently, no photocathode meets all of the stated requirements and tradeoffs must be made for each application.

For UED applications, the transverse coherence length (L_{\perp}) of the electron beam is important[9]. It is related to the beam emittance according to

$$L_{\perp} = \lambda \frac{\sigma_{e,x}}{\epsilon_{n,x}}. \quad (3.2)$$

where $\lambda = \frac{\hbar}{m_e c}$ is the reduced Compton wavelength and $\sigma_{e,x}$ is the rms size of the electron beam at the sample. This coherence length has to be of the order of the unit cell size of the molecule one is trying to resolve (which is of the order of 10 nm for proteins). Reducing MTE of the photocathodes to the <10 meV range would accomplish this task in the modern photoemission guns used for UED. If the MTE is made even smaller (1-2 meV scale) other effects, like disorder-induced heating [10], which are not directly related to the photocathodes themselves, come into play. However, no photocathode at the moment can demonstrate this low MTE simultaneously with a fast (< 1 ps) response time.

Reduction in MTE has been predicted from *ab initio* calculations of the surface band structure of Ag photocathodes with a thin layer of MgO[15]. However, such a photocathode has not been realized in practice. Furthermore, even with plasmonic QE enhancement[14], metallic photocathodes cannot provide sufficient QE to meet the requirements of high current applications[12]. QE greater than 1% in visible light can be obtained from III-V semiconductor photocathodes like GaAs activated to negative electron affinity (NEA) using Cs and NF₃ (or O₂) or from alkali-antimonides with positive electron affinity. MTE reduction in GaAs is possible at longer wavelengths, but at the expense of other parameters. Alkali-antimonides tend to have high surface roughness which limits the minimum MTE obtained to greater than 100 meV[64, 22].

In the past, layered semiconductor structures consisting of GaAsP/GaAs and InGaAs/AlGaAs have been developed for polarized electron sources[27]. Complex III-V semiconductor structures consisting of AlGaAs and GaAs layers with graded doping have been grown and activated to NEA with the goal of maximizing QE[65]. QE in excess of 50% with 2.4 eV photons has been obtained[65]. However, the MTE and response time of such QE-enhanced layered structures remains unknown. Furthermore, theoretical models so far have been unable to quantitatively predict photoemission properties like QE, MTE and response time from such photoemitters.

Recently, a quantitative agreement between theory and experiment has been obtained for these photoemission properties from NEA GaAs cathodes using a photoemission simulation that employs a semiclassical photoemission model using Monte Carlo based electron transport without the use of any *ad hoc* parameters[29]. In this letter, this simulation tool has been extended to allow photoemission from III-V semiconductor layers with graded doping. Guided by the simulations, a layered structure with a lower MTE and response time has been engineered. The measured photoemission properties from this engineered photoemitter are found to be in excellent agreement with the simulations.

For the first time, we have proposed and demonstrated a reduction in MTE along with a possible reduction in response time of photocathodes, by controlling the surface band bending and transport properties of a layered semiconductor structure. This opens a way to systematic, theory-driven design of complicated layered structures of III-V semiconductors that exploit the band gaps, inter-valley deformation potentials and electron transport properties of different semiconductor materials along with graded doping for optimization of var-

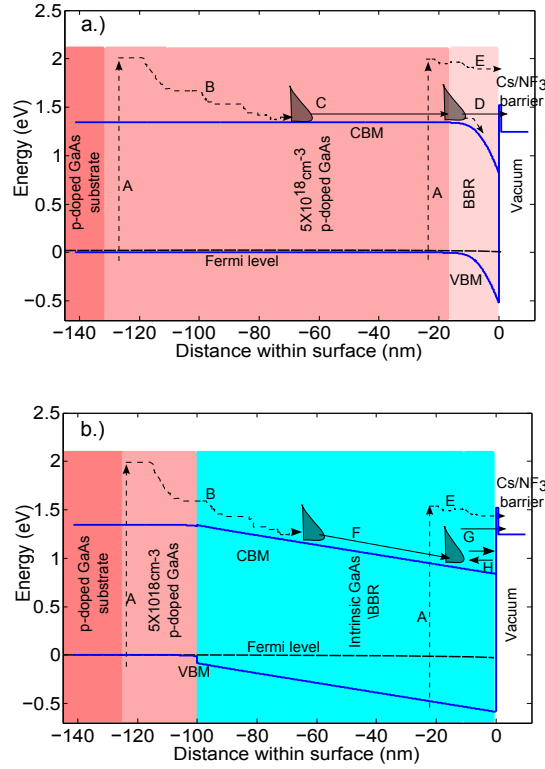


Figure 3.1: Process of photoemission from a) activated p -doped GaAs, b) layered structure with 100nm intrinsic GaAs. The various electron processes (indicated A-H) are described in the text.

ious photoemission properties. The use of such structures optimized for photoemission are expected to produce ultra-bright and ultra-fast electron bunches improving the performance in existing applications and enabling new ones.

3.3 Design of Layered Structures

The photoemission simulation approach [29] is based on Spicer's 3-step photoemission model[28]. Figure 3.1a shows the three steps of photoemission for p -doped GaAs. The first step is the excitation of electrons from the valence to the conduction band (process A in Figure 3.1). The second step is the transport

of excited electrons to the surface (processes B and C in Figure 3.1). During this step, the excited electrons scatter with phonons, holes and other electrons, losing energy and thermalizing towards the conduction band minima (CBM). A 3-D semi-classical electron transport model along with the 3-valley model for the conduction band structure is used to model this process. Scattering of electrons is taken into account using a Monte Carlo scheme. Scattering processes with acoustic, polar optical and inter-valley optical phonons as well as charged impurities and holes have been included. An electric field is applied to the electrons to simulate band-bending near the surface. The third step is the emission of electrons into vacuum (process D in Figure 3.1). Some electrons that are excited close to the surface reach vacuum without complete thermalization (process E in Figure 3.1). Due to the activating layer of Cs and NF_3 (or O_2) on the surface the vacuum level goes below the bulk conduction band minima (NEA condition). Electrons reaching the surface tunnel through a small barrier formed by the activating layer and are emitted into vacuum.

The small effective electron mass in the Γ -valley of GaAs along with the conservation of transverse momentum at the surface should cause the MTE to be lower than 5 meV. However, the measured values of MTE are an order of magnitude higher. This discrepancy is not well understood and has been attributed to surface roughness or surface scattering during emission[63]. In the simulations, this fact has been accounted for by introducing an elastic process that causes the electrons to be emitted in a cosine distribution about the normal to the surface (refer to [29] for details). The MTE values obtained from using this assumption are close to the experimental results. NEA, defined as the difference between the bulk CBM and the vacuum level, has a very strong dependence on the surface cleanliness, vacuum conditions and the details of the activation procedure. This

varies from sample to sample and from activation to activation and is difficult to reproduce exactly in experiment. The typical value of NEA may vary from 50 mV to 250 mV. In the simulation the NEA is allowed to vary between these values to best fit the experimental data but afterwards it is held fixed for any particular sample. Details of this simulation approach and its implementation have been presented elsewhere[29].

The simulation tool described above has been extended to handle layered structures. The energies of the Γ -valley, L-valley, X-valley and valence band maxima (VBM) as a function of the depth beneath the surface are calculated using a Schrodinger-Poisson solver[1]. We assume that the Fermi level at the surface is pinned to one-third of the band gap above the VBM at the surface due to the activation layer present[54]. The band gap renormalization due to high doping has been included[66]. The gradient of the valley minima gives the electric field applied to the electrons in that particular valley during the electron transport. Scattering is taken into account using the same Monte Carlo technique. The scattering rates have a spatial dependence in accordance with the layer material and doping level and the hole density obtained from the Schrodinger-Poisson solver.

The simulation model has several limitations. It does not include the effects of localized quantum states near the surface in the band-bending regions. The transport of electrons is treated in a semi-classical fashion and does not include quantum tunneling and reflection except at the vacuum interface. The effects of quantum well states have also been ignored. The maximum photon energy that can be simulated is limited by the electron energies up to which the 3-valley model of the conduction band is valid. This limit is about 2.4 eV for GaAs.

Despite these limitations, the simulations produce excellent agreement with the experimental data as discussed below.

Photoemission from a structure made of a layer of intrinsic GaAs over the bulk GaAs p -doped to $5 \times 10^{18} \text{cm}^{-3}$ was simulated for an incident photon energy of 2.4 eV (photon energy of a standard frequency-doubled ytterbium fiber laser). Figure 3.1b shows the process of photoemission from this structure with a 100 nm thick intrinsic GaAs layer. The intrinsic GaAs layer causes the band-bending region (BBR) to extend into the surface nearly to the entire depth of the intrinsic layer. This affects the excitation and transport properties and hence changing the photoemission characteristics with the thickness of this layer. The dependence of QE, MTE and response time on the thickness of this layer is shown in Figure 3.2 for two values of NEA. Throughout this work, we quote the characteristic response time defined as the time required for about 57% of all photoemitted electrons to escape into vacuum assuming an infinitely short laser pulse[13].

In order to understand the effects of the intrinsic layer on emission, the emitted electrons can be roughly classified into two categories: 1) those that are excited close to the surface and get emitted before thermalizing; and 2) those that are excited deep within the surface and thermalize to the bulk CBM before emission. For a p -doped cathode without any intrinsic layer, the category 2 electrons dominate the emission. The BBR is small so these electrons do not get enough time to relax in it. As the thickness of the intrinsic layer increases more category 2 electrons relax into the BBR (process F in Figure 3.1). Most of these electrons do not have sufficient energy to escape and get trapped in the BBR (process H in Figure 3.1), eventually recombining with holes. Some of the category 2 electrons

do not relax sufficiently in the BBR and have a high enough energy to be emitted (process G in Figure 3.1). This relaxation causes a number of the category 2 electrons to take a long time to reach the surface with insufficient energy to escape into vacuum. This explains the reduction of the QE and response time seen in Figures 3.2a and 3.2b.

The relaxation in the BBR also reduces the average energy of the emitted electrons. This causes the MTE to initially drop with increasing intrinsic layer thickness. However, as the thickness of this layer increases further, most of the category 2 electrons cannot be emitted, leading to the category 1 electrons to dominate the photoemission. These electrons are not thermalized and have a high energy when they reach the surface. This causes the MTE to eventually increase with the intrinsic layer thickness as seen in Figure 3.2c.

Thus, it is possible to reduce both MTE and response time simultaneously via an optimal choice of the intrinsic layer thickness. Even though this reduction is accompanied by a drop in QE, it still remains above the 1% level needed for many applications[12].

3.4 Experimental Results

Guided by the simulations, a structure consisting of a 100 nm thick layer of intrinsic GaAs over the $5 \times 10^{18} \text{ cm}^{-3}$ *p*-doped bulk (Figure 3.1b) was grown using molecular beam epitaxy (MBE). The sample was capped with a thick layer of As, removed from the MBE chamber and transported in air into the GaAs activation chamber. The base vacuum in the GaAs activation chamber was 3×10^{-11} Torr. Here, the As cap was removed by heating the sample to 350°C for 2 hours, thus

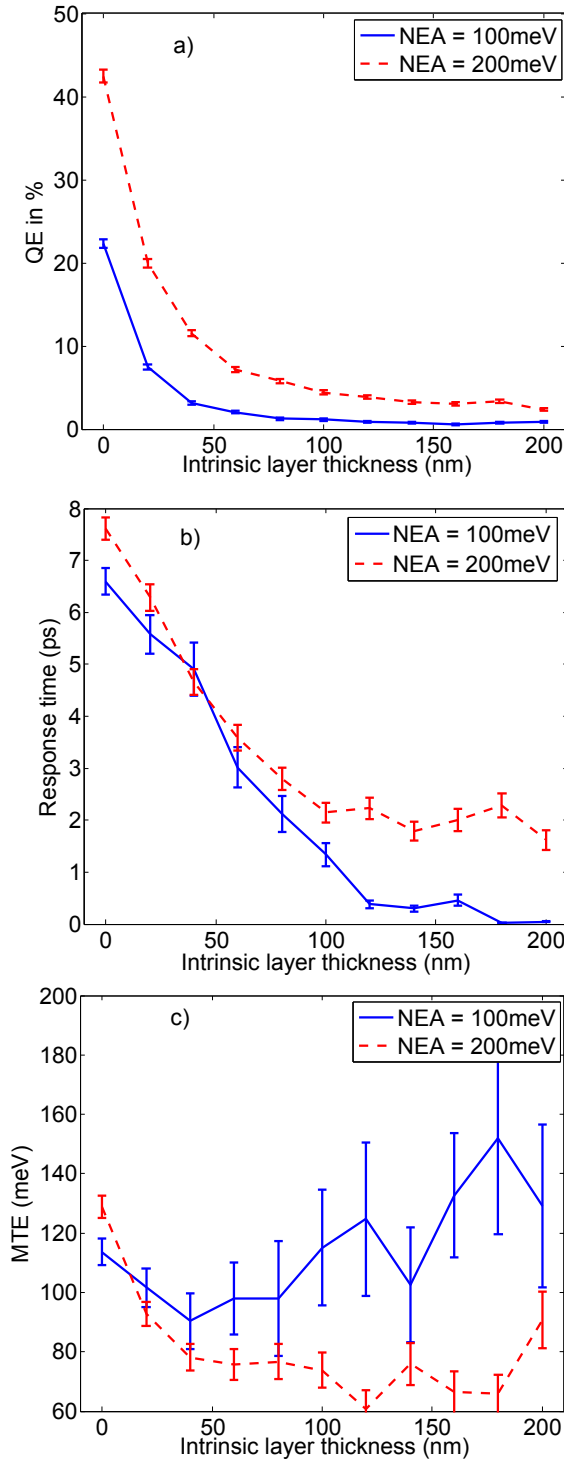


Figure 3.2: Simulations of a) QE, b) Response time and c) MTE as a function of the thickness of intrinsic GaAs layer for NEA of 100meV and 200meV. A thin layer of intrinsic GaAs on heavily *p*-doped GaAs causes the response time and MTE to reduce, changing them in a favorable way. The reduction in QE is unfavorable but can be tolerated for use in a photoinjector.

preserving the surface structure and cleanliness. The sample was activated to NEA using alternating exposures of Cs and NF_3 [24].

The spectral response was measured by collecting the current emitted from the activated sample while scanning the wavelength of the incident light. The activation chamber is connected in vacuum to a high voltage DC photogun[12]. Here, the MTE of emitted electrons was measured at various photon energies using a thoroughly benchmarked solenoid scan technique[13, 22].

A control sample, a GaAs wafer p -doped uniformly to $5 \times 10^{18} \text{ cm}^{-3}$ (Figure 3.1a), was transported from the MBE chamber, cleaned, activated and measured using the exact same procedure as the layered sample.

Figure 3.3 shows the spectral response and MTE measurements of this sample and the control sample along with the simulation results. NEA of 70 mV and 140 mV were used in the simulation to fit the data from the control and the layered samples, respectively. It is seen that the measured results are in excellent agreement with the simulations. The measurements show a 30-50% drop in the MTE for the layered sample as compared to the control sample in the red-green wavelengths. For a given bunch charge and a bunch frequency (determined by the application of the photoinjector), this results in a proportional increase in beam brightness [7, 67].

3.5 Conclusion

In summary, using the Monte Carlo based photoemission simulation model we designed a layered GaAs photocathode with reduced MTE and response time

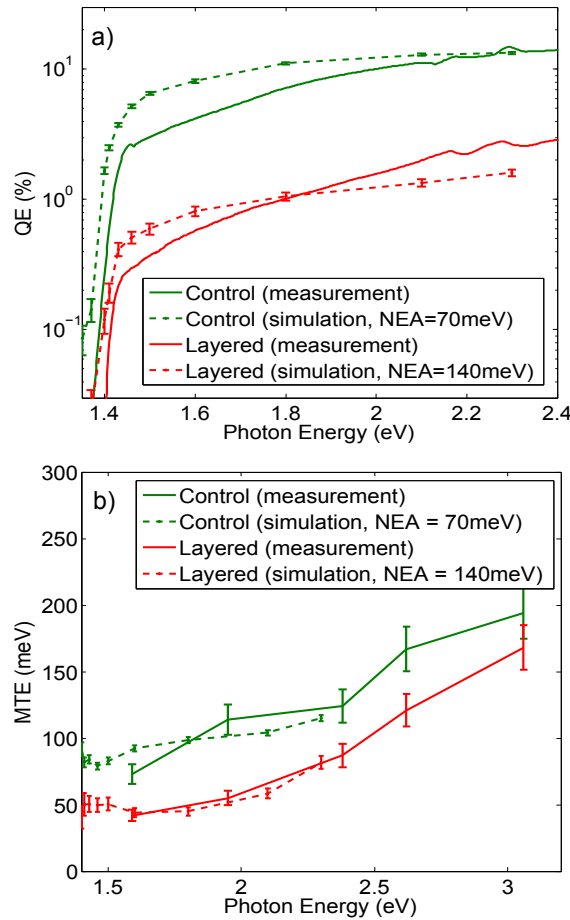


Figure 3.3: a) QE and b) MTE as a function of incident photon energy for the two samples. The simulated results agree well with the experiment. The layered cathode shows a reduced QE w.r.t the control sample. However, the QE is still greater than 1% in the green, exceeding the QE requirement of most photoinjectors[12]. NEA is fixed for a particular sample. It should be noted that the photon energy range above 2.4 eV is outside the validity of the 3-valley model for GaAs and cannot be simulated.

compared to the bulk GaAs. The structure was grown using MBE and activated to NEA. The measured QE and MTE agree well with the simulations. This and more advanced layered structures will be used to increase the electron beam brightness obtained from photoinjectors in the future.

This work has been funded by the NSF under grant number DMR-0807731 and DOE under grant number DE-SC0003965. The authors would like to thank Dr. Dimitre Dimitrov, Tech-X Corp, Boulder, CO, for many useful discussions.

CHAPTER 4
EFFECTS OF SURFACE NON-UNIFORMITIES ON THE MEAN
TRANSVERSE ENERGY FROM PHOTOCATHODES

4.1 Abstract

The mean transverse energy of electrons obtained from photocathodes limits the performance of photoinjectors. The factors that influence the mean transverse energy are poorly understood. In this paper we show that spatial work function variations and sub nanometer scale roughness and surface defects can limit the mean transverse energy. Atomically perfect surfaces will be required to minimize the mean transverse energy obtained from photocathodes.

4.2 Introduction

Photoinjectors provide electron beams for most 4th generation light sources like energy recovery linacs and free electron lasers and ultra-fast electron diffraction (UED) setups. For light source applications, the mean transverse energy (MTE) of electrons emitted from the photocathode limits the beam brightness obtained from photoinjectors[7]. For UED applications, the transverse coherence length of the electron beam is limited by the MTE obtained from photocathodes[8, 9]. The transverse coherence length sets the maximum size of the crystal unit cell for which a diffraction pattern can be resolved. Thus reducing the MTE from photocathodes can result in brighter electron beams and can allow UED of crystals with larger unit cells, for example, proteins.

Thermal emittance, which is the volume occupied by the electron beam in phase space, is a more familiar quantity to accelerator physicists. The normalized thermal emittance can be related to the MTE and the rms laser spot size on the cathode ($\sigma_{l,x}$) through the relation $\epsilon_{n,x} = \sigma_{l,x} \sqrt{\frac{\text{MTE}}{m_e c^2}}$ where m_e is the mass of an electron and c is the speed of light.

The theoretical lower limit to the MTE, given by a disorder induced scattering after emission, is 1-2 meV[10]. Smallest MTE demonstrated is in the 25-40 meV range from GaAs activated to negative electron affinity (NEA) using Cs and NF₃[13] under infrared illumination or from antimony films using near photoemission threshold wavelengths[20]. However, NEA-GaAs under infrared illumination has a very large response time in the 100 ps range[13] and antimony or other metals have very small quantum efficiency near photoemission threshold making them impractical for use in a photoinjector. In most photoinjectors, MTE in range of 100 meV to 1 eV is obtained from photocathodes[11]. Thus, nearly two orders of magnitude improvement in MTE may be possible by engineering photocathode materials[17, 16, 15]. However, no theory exists that can explain the observed MTE from photocathodes satisfactorily; several discrepancies exist.

One theory states that the MTE obtained from metal photocathodes is nearly one third the excess energy[18]. Here, the excess energy is defined as the energy difference between the incident photon and the work function of the material. An extension of this theory states that the MTE approaches the lattice temperature energy (25 meV at room temperature) as the excess energy tends to zero (near photoemission threshold)[68]. This theory produces reasonable agreement with experimental data for metal and thin film alkali antimonide

photocathodes[20, 64, 22, 69]. However, this theory does not take into account the effects of band structure, conservation of transverse momentum during emission and the effective mass of electrons in the lattice. In NEA-GaAs cathodes, the conservation of transverse momentum and small effective mass of electrons in the Γ valley should result in a MTE below 20 meV in infrared-green wavelengths[29, 23]. However, experimental results show a MTE of 25-120 meV in this wavelength range[13]. This discrepancy has been attributed to a surface scattering mechanism that redistributes the emitted electrons uniformly in the polar angle[29] or causes the Γ valley electrons near the surface to have an effective mass equal to the mass of a free electron[62]. However, no physical reason for this scattering mechanism has been identified.

To add to the complexity, the surfaces of frequently used photocathode materials are far from perfect. Photocathode surfaces often display roughness on the scales of 10s of nm[70, 71, 63]. Single crystal photocathodes which are atomically flat may exhibit surface reconstructions, atomic scale surface defects and monolayer adsorbates. The effect of greater than 10 nm scale roughness on MTE has been studied[63, 71, 72, 25]. However, the effect of sub-nm scale surface defects, surface reconstructions and adsorbates on MTE remained unexplored.

Work function variations ranging from 1 meV to 100s of meV over less than nm scale to micron scale (along the cathode surface) can be caused due to atomic defects, atomic steps, surface reconstructions, localized charging, localized strains, grain boundaries and adsorbates[73, 74, 75, 76]. The effect of such work function variations on MTE also remained unexplored.

In this paper, we investigate the effect of these work function variations and surface non-uniformities to show that it is important to consider them in order

to explain the observed MTE accurately.

First we treat the effect of spatial work function variations on emitted electrons in a classical manner. The classical treatment is valid whenever the De Broglie wavelength of emitted electrons is much smaller than the scale of the spatial work function variation. Electric fields are formed in the vacuum region close to the cathode surface because of the work function variations. These electric fields deflect the emitted electrons and cause the MTE to increase. We estimate the rise in MTE due to these electric fields for a sinusoidal variation in the work function. We show that the effect of work function variation can be significant, but reduces with increase in the kinetic energy of the emitted electron.

Next, we formulate a quantum mechanical emission model to include the effects of surface non-uniformities in the case when the De Broglie wavelength of the emitted electrons is similar to the scale of the surface non-uniformities. Such non-uniformities include atomic steps and defects, surface reconstructions, work function variations on a nm scale and adsorbates.

Finally, using the quantum mechanical formulation and the example of photoemission from activated GaAs photocathodes we show that sub nm scale roughness which can comprise of atomic steps, surface defects and surface reconstructions can limit the minimum MTE attainable.

4.3 Classical treatment

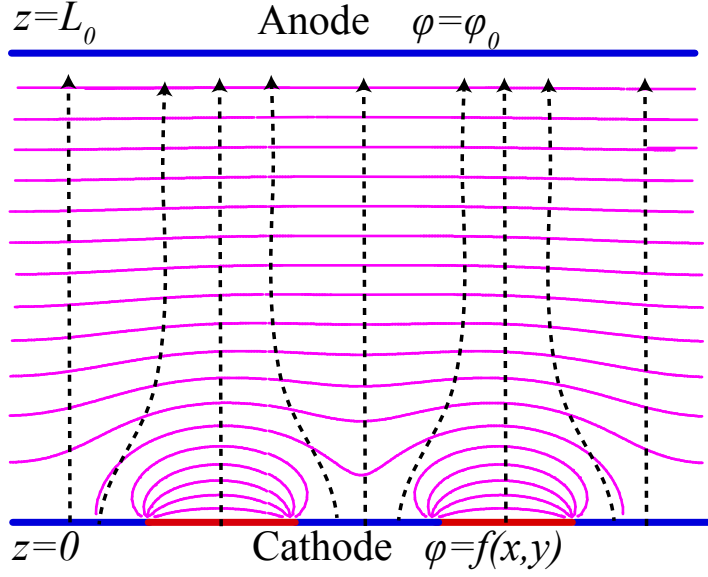
Generally, electrons emitted from photocathodes have kinetic energies in the 10 meV to 1 eV range[11]. This results in a De Broglie wavelength of 1 nm to 10 nm. Thus spatial variations in work functions at a scale much greater than 10 nm can be treated in a classical manner. Work function variations at these large spatial scales can be caused due to localized surface charging, localized strains, patches of surface adsorbates and different grain orientations[73, 74, 75, 76].

The spatial variations in work function cause transverse (parallel to cathode surface) electric fields. These give a transverse kick to the emitted electrons and increase the MTE of the cathode. In this section, we calculate the electric fields formed due to a sinusoidal work function variation and estimate the effect they have on the MTE.

A similar effect, in which the transverse electric fields are caused due to the surface roughness of the cathode has been studied[72, 25]. The calculation given below to estimate the effects of work function variation on MTE closely follows surface roughness effect calculation.

4.3.1 Details of model and calculation

The potential of an electron right outside an electrode is the negative of bias applied to the electrode in volts plus the work function in eV. Thus variation in the work function essentially causes a variation in the surface potential of the electrode. In any photoinjector, a cathode is placed in a very high ($\sim 1-50$ MV/m) longitudinal electric field. The variations in the surface potential cause the lon-



— Equipotential lines \dashrightarrow Electron trajectory

Figure 4.1: Parallel plate capacitor model to calculate the effect of variation of work function on MTE. The equipotential lines get distorted near the cathode due to the non-uniform work function. This causes the electrons emitted from the cathode to gain transverse energy.

itudinal electric field very close to the cathode surface to deform and acquire transverse components which decay rapidly as one goes away from the cathode. To model such a field we consider a parallel plate capacitor as shown in figure 4.1. It consists of a cathode that is grounded at $z = 0$ and a parallel anode biased to a voltage ϕ_0 at $z = L_0$. Thus the longitudinal electric field at the cathode without the work function variation is $E_0 = \phi_0/L_0$. Let the work function variation on the cathode be given by $f(x, y) \ll \phi_0$. For simplicity we approximate the work function variation by a sinusoidal function, $f(x, y) = h \sin\left(\frac{2\pi}{a}x\right) \sin\left(\frac{2\pi}{a}y\right)$, where h is the amplitude of the work function variation and a is its spatial period.

Using the Laplace equation $\nabla^2\phi = 0$ with boundary conditions $\phi|_{z=0} = f(x, y)$ and $\phi|_{z=L_0} = \phi_0$ we can obtain ϕ in the region between the cathode and the anode

as

$$\begin{aligned}\phi(x, y, z) = & \phi_0 \frac{z}{L_0} \\ & + h \frac{(e^{-zy} - e^{(z-2L_0)\gamma})}{1 - e^{-2L_0\gamma}} \sin\left(\frac{2\pi}{a}x\right) \sin\left(\frac{2\pi}{a}y\right)\end{aligned}\quad (4.1)$$

where $\gamma = \frac{2\sqrt{2}\pi}{a}$. We also assume that $a \ll L_0$ so that the transverse electric fields (E_x and E_y) are nearly zero well before $z = L_0$. Using this approximation the potential can be given as

$$\begin{aligned}\phi(x, y, z) = & \phi_0 \frac{z}{L_0} \\ & + h e^{-zy} \sin\left(\frac{2\pi}{a}x\right) \sin\left(\frac{2\pi}{a}y\right)\end{aligned}\quad (4.2)$$

From this the electric fields in the x , y and z can be calculated as:

$$\begin{aligned}E_x &= \frac{2\pi}{a} h e^{-zy} \cos\left(\frac{2\pi}{a}x\right) \sin\left(\frac{2\pi}{a}y\right) \\ E_y &= \frac{2\pi}{a} h e^{-zy} \sin\left(\frac{2\pi}{a}x\right) \cos\left(\frac{2\pi}{a}y\right) \\ E_z &= -E_0 + h \gamma e^{-zy} \sin\left(\frac{2\pi}{a}x\right) \sin\left(\frac{2\pi}{a}y\right)\end{aligned}\quad (4.3)$$

The transverse velocities (v_x and v_y) can be calculated by integrating the equations of motion. We integrate the equations of motion numerically using an 8-stage symplectic implicit integrator[77]. Electrons are launched from a fine grid of spacing $a/40$ on the surface to obtain a fine sampling of all areas of the surface. The electrons are launched perpendicular to the surface with kinetic energy K . The initial transverse velocity and energy are set be zero. The electrons are tracked in the electric field given by equation 4.3 and the trajectories are calculated till the point the transverse electric fields become negligible and

the transverse velocities are constant. The mean transverse energy is then calculated by averaging over the transverse energy of all the electrons. As the initial transverse velocities and energies are zero, this analysis gives us only the contribution of work function non-uniformities to the MTE.

An analytic expression for the MTE can also be obtained by making the assumption $h/a \ll E_0$ and that the change in the x and y is negligible compared to a . With these assumptions the expressions for the electric fields become:

$$\begin{aligned} E_x &= \frac{2\pi}{a} h e^{-z\gamma} \cos\left(\frac{2\pi}{a} x_0\right) \sin\left(\frac{2\pi}{a} y_0\right) \\ E_y &= \frac{2\pi}{a} h e^{-z\gamma} \sin\left(\frac{2\pi}{a} x_0\right) \cos\left(\frac{2\pi}{a} y_0\right) \\ E_z &= -E_0 \end{aligned} \quad (4.4)$$

where x_0 and y_0 are the co-ordinates of the point from where the electron is launched.

Under these approximations the equations of motion can be integrated analytically to give MTE as:

$$\text{MTE} = \frac{\pi^2 h^2 e}{4 \sqrt{2} a E_0} e^{-\frac{\beta^2}{2\alpha}} \text{erfc}^2\left(\frac{\beta}{2 \sqrt{\alpha}}\right) \quad (4.5)$$

where $\alpha = \frac{\sqrt{2}\pi e E_0}{a m_e}$ and $\beta = \frac{4\pi \sqrt{K}}{a \sqrt{m_e}}$.

4.3.2 Results

Figure 4.2 shows the MTE calculated by numerically tracking electron trajectories for initial kinetic energies (K) of 20 meV and 60 meV and $a = 100$ nm. Figure 4.2a shows the MTE calculated at zero electric field as a function of h for $K = 20$

meV. We can see that values of h as low as 0.1 V can result in MTE higher than 20 meV.

Figure 4.2b shows the variation of MTE with electric field for two cases: $h = 0.1$ V and $K = 20$ meV; $h = 0.6$ V and $K = 60$ meV. We can see that for both cases the MTE is nearly constant with electric field (E_0) so long as the electric field is below h/a (shown by the black lines in the figure). If $E_0 < h/a$, the first term in the expression for E_z in equation 4.3 can be ignored, making the electric field near the cathode surface independent of E_0 . Hence the MTE does not vary much with E_0 in this regime. However, as the electric field rises beyond h/a , the electrons are extracted away from the cathode surface more quickly. This gives them less time to interact with the transverse electric fields close to the surface and hence the MTE reduces. This reduction in MTE with electric field should be easily observable in with electric fields in the range of 1-10 MV/m if the MTE is indeed limited by work function non-uniformities on a classical scale. Such a change with electric field is contrary to the change expected due to the 10-100 nm scale surface roughness[72, 25]. Due to the surface roughness effect, the MTE increases with increasing electric field.

MTE also reduces with increase in initial kinetic energy (K) and increase in the period a . Figure 4.3 a and b show the variation of MTE with initial kinetic energy and the period a respectively, for $h = 0.1$ V and $E_0 = 10$ MV/m. These parameters are such that the approximations made to estimate the MTE in equation 4.5 are valid. The MTE in figure 4.3 is calculated from this equation.

In short, we see that work function variations of ~ 0.1 eV over a scale of ~ 100 nm can limit the MTE to 20-30 meV if the kinetic energy of electrons emitted electrons is near 20 meV. This is often the case with near threshold photoemis-

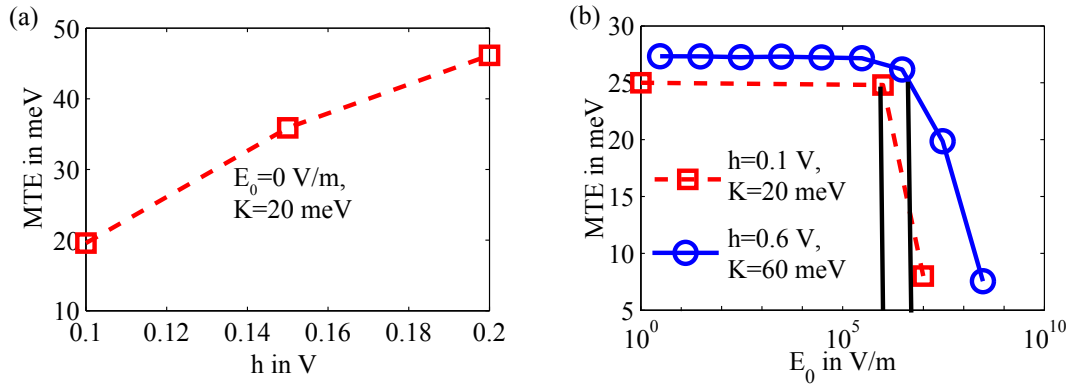


Figure 4.2: (a) Variation of MTE with h . The external electric field was set to zero for these calculations. (b) Variation of the MTE with the electric field, E_0 . The value of a was set to 100 nm for these calculations. h/a for the red curve is 1 MV/m and for the blue curve is 6 MV/m (shown by the black lines). The MTE is nearly independent of the electric field when $E_0 < h/a$, beyond that it reduces sharply with the electric field.

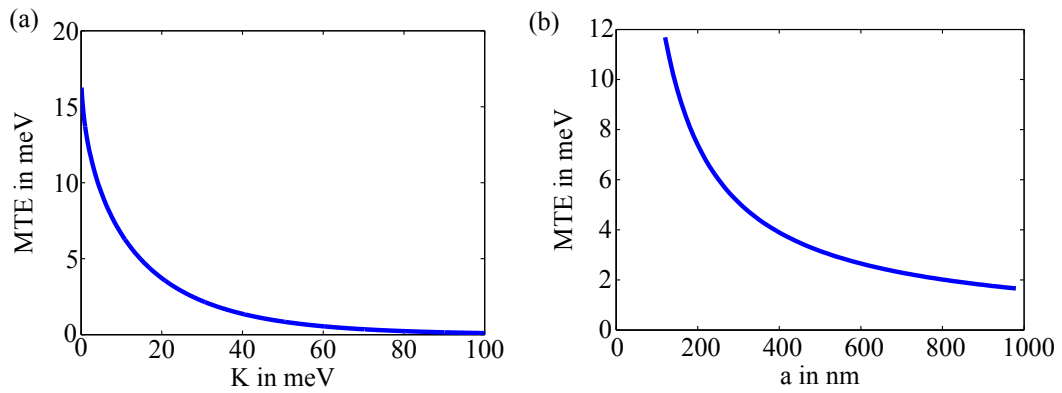


Figure 4.3: (a) Variation of MTE with the initial kinetic energy. $E_0 = 10$ MV/m, $h = 0.1$ V and $a = 100$ nm (b) Variation of MTE with the the period a . $E_0 = 10$ MV/m, $h = 0.1$ V and $K = 1$ meV.

sion, where the excess energy and hence the kinetic energy of emitted electrons is ~ 25 meV (thermal energy at room temperature). Hence, in order to obtain MTE of less than 20 meV it will be necessary to ensure the spatial uniformity of cathode work functions.

4.4 Quantum treatment

Electrons emitted from photocathodes have a De Broglie wavelength ranging from 1 nm to 10 nm. Surface non-uniformities on this scale have to be treated in a quantum mechanical manner. Such surface non-uniformities may include atomic defects, steps, surface reconstructions, adsorbates and work function variations on this scale.

Below we develop an emission model that takes into account surface non-uniformities and show how conservation of transverse momentum can be violated in their presence.

4.4.1 Emission model

The emission model described here assumes a semiconductor cathode, however it can easily be extended to metallic cathodes.

The model assumes Spicer's 3-step process of photoemission[28]. The first two steps of electron excitation from valence band to conduction band and subsequent electron transport to the surface in the conduction band are well understood[29]. Here we discuss the last step of emission to include the effects

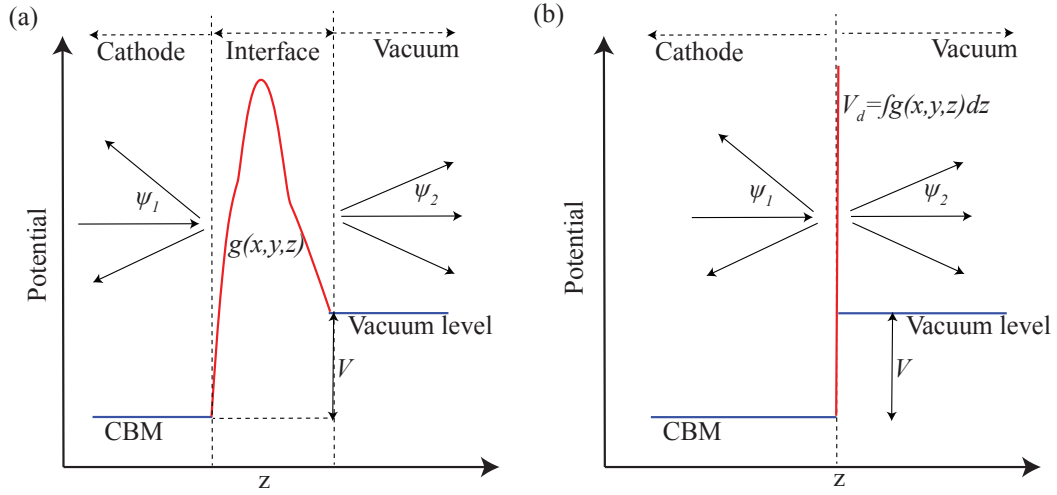


Figure 4.4: (a) Potential to model the surface non-uniformities along with the incoming and scattered wave functions (b) δ function approximation to the potential used to account for surface non-uniformities

of surface non-uniformities.

Figure 4.4a shows the potential used to describe the cathode-vacuum interface. The electrons approach the surface in the form of plane waves with crystal momentum \mathbf{k}_{in} and energy E_c . We assume that the energy and the crystal momentum are related via the parabolic, spherical dispersion relation

$$E_c = \frac{\hbar^2 |\mathbf{k}_{\text{in}}|^2}{2m^*} \quad (4.6)$$

where m^* is the effective mass of the electron inside the cathode. The potential within the cathode and in vacuum is assumed to be constant. The interface is represented by a potential $g(x, y, z)$ along with a step of height V . The potential $g(x, y, z)$ includes all interface effects, transverse variations of the potential due to surface non-uniformities and defects and electric fields due to work function variations. $g(x, y, z)$ is zero in the cathode bulk and in vacuum, but is non-zero

in the interface region. The incoming electron wave gets scattered due to the potential $g(x, y, z)$. Part of the incoming wave gets reflected and the rest gets transmitted into vacuum.

We approximate the wave function of the incoming electron with a plane wave $\psi_{in} = e^{i(\mathbf{k}_{inr}\mathbf{r} + k_{inz}z)}$ where $\mathbf{k}_{inr} = k_{inx}\vec{\mathbf{x}} + k_{iny}\vec{\mathbf{y}}$ is the transverse component and $k_{inz}\vec{\mathbf{z}}$ is the longitudinal component of the wave vector \mathbf{k}_{in} and \mathbf{r} is the position vector in the transverse direction.

The challenge is to calculate the scattering of the incoming plane wave due to the interface potential $g(x, y, z)$. A similar problem has been studied extensively to model electron transport across semiconductor heterojunctions[78, 79, 80, 81, 82, 83]. The most general solution to this problem is obtained by solving the Lippmann-Schwinger equation[78, 84]. Solutions using tight-binding like approach[79, 80, 81] and transfer matrix approach have also been attempted[82].

Here, we simplify this problem by replacing the interface potential $g(x, y, z)$ by a δ function whose height varies in x and y and is given by $V_d(x, y) = \int g(x, y, z) dz$. Such a simplification is valid when the interface region is much smaller than the wavelength of the emitted electrons. Figure 4.4b shows the potential with this δ function approximation. The Hamiltonian for this system can be written as

$$H = -\frac{\hbar^2}{2} \nabla \left(\frac{1}{m} \nabla \right) + V \cdot S(z) + V_d(x, y) \delta(z) \quad (4.7)$$

where $m = m^*$ if $z < 0$ and $m = m_e$ if $z \geq 0$ and $S(z)$ is the heavy side function.

$V_d(x, y)$ can be expanded in terms of its Fourier components as

$$V_d(x, y) = \sum_{\eta} V_{\mathbf{k}_{\eta}} e^{i(\mathbf{k}_{\eta} \cdot \mathbf{r})} \quad (4.8)$$

The wave function of the incoming and the reflected electrons within the photocathode can then be written as

$$\begin{aligned} \psi_1 = & \psi_{in} + \alpha_{\mathbf{k}_{inr}} e^{i(\mathbf{k}_{inr} \cdot \mathbf{r} - k_{1inz} z)} + \\ & \sum_{\eta} e^{i(\mathbf{k}_{r\eta} \cdot \mathbf{r} - k_{1z\eta} z)} \end{aligned} \quad (4.9)$$

where $\mathbf{k}_{r\eta}$ and $k_{1z\eta} \hat{\mathbf{z}}$ are the transverse and longitudinal components, respectively, of the wave vectors into which the incoming electron wave is scattered due to reflection from the barrier V_d and $\alpha_{\mathbf{k}_{r\eta}}$ are the probability coefficients for the respective scattered wave vectors.

The wave function of the electrons transmitted into vacuum can be written as

$$\psi_2 = (1 + \alpha_{\mathbf{k}_{inr}}) e^{i(\mathbf{k}_{inr} \cdot \mathbf{r} + k_{2inz} z)} + \sum_{\eta} \alpha_{\mathbf{k}_{r\eta}} e^{i(\mathbf{k}_{r\eta} \cdot \mathbf{r} + k_{2z\eta} z)} \quad (4.10)$$

where $\mathbf{k}_{r\eta}$ and $k_{2z\eta} \hat{\mathbf{z}}$ are the transverse and longitudinal components, respectively, of the wave vectors into which the incoming electron wave is scattered in vacuum.

ψ_1 and ψ_2 are general and satisfy the condition $\psi_1 = \psi_2$ at $z = 0$.

We assume that this scattering is elastic in nature. Hence from the conservation of energy, all the reflected wave vectors satisfy the relation

$$\frac{\hbar^2 (k_{r\eta}^2 + k_{1z\eta}^2)}{2m^*} = E_c \quad (4.11)$$

and all the transmitted wave vectors satisfy the relation

$$\frac{\hbar^2 (k_{r\eta}^2 + k_{2z\eta}^2)}{2m_e} = E_v = E_c - V \quad (4.12)$$

$$\frac{\hbar^2 (k_{inr}^2 + k_{2inz}^2)}{2m_e} = E_v = E_c - V \quad (4.13)$$

where E_v is the kinetic energy of the electron emitted into vacuum.

Now the coefficients $\alpha_{k_{inr}}$ and $\alpha_{k_{r\eta}}$ can be calculated by integrating the Schrodinger equation for the Hamiltonian given in equation 4.7 across the δ barrier in the z direction from 0^- to 0^+ and comparing the coefficients of the same exponents as done by Liu and Coon[83].

For a 1-D sinusoidal δ barrier at the surface, given by $V_d = 2V_0 \cos(k_s x)$ the set of equations to calculate α coefficients can be written in the form of a tridiagonal matrix system as

$$\begin{pmatrix} \ddots & & & & \\ \cdots & D(k_{inx} - k_s) & -V_0 & 0 & \cdots \\ \cdots & -V_0 & D(k_{inx}) & -V_0 & \cdots \\ \cdots & 0 & -V_0 & D(k_{inx} + k_s) & \cdots \\ \cdots & \vdots & \vdots & \vdots & \ddots \end{pmatrix} \begin{pmatrix} \vdots \\ \alpha_{k_{inx}-k_s} \\ \alpha_{k_{inx}} \\ \alpha_{k_{inx}+k_s} \\ \vdots \end{pmatrix} = \begin{pmatrix} \vdots \\ 0 \\ V_0 \\ R(k_{inx}) \\ V_0 \\ 0 \\ \vdots \end{pmatrix} \quad (4.14)$$

where, $R(k_x) = \frac{\hbar^2}{2} \left(\frac{k_{2z}}{m_e} - \frac{k_{1z}}{m^*} \right)$ and $D(k_x) = \frac{\hbar^2}{2i} \left(\frac{k_{2z}}{m_e} + \frac{k_{1z}}{m^*} \right)$. k_{1z} and k_{2z} can be calculated in terms of k_r from equations 4.11 and 4.12.

By solving this system one can obtain the coefficients α in terms of the transverse wave vector of the incoming plane wave k_{inx} and the δ barrier at the interface. The probability of transmission into one of the scattered components with transverse wave vector $k_x \neq k_{inx}$ is given by[82]

$$T_{k_x} = \frac{m^* |\alpha_{k_x}|^2 (k_{2z} + k'_{2z})}{2m_e k_{1z}} \quad (4.15)$$

and the probability of unscattered transmission is given by

$$T_{k_{inx}} = \frac{m^* |1 + \alpha_{k_{inx}}|^2 (k_{2inz} + k'_{2inz})}{2m_e k_{1inz}} \quad (4.16)$$

The MTE due to the emission of the plane wave can then be given by

$$\text{MTE} = \frac{\sum_m \frac{\hbar^2 (k_{inx} + mk_s)^2 T_{k_{inx} + mk_s}}{2m_e}}{\sum_m T_{k_{inx} + mk_s}} \quad (4.17)$$

4.4.2 Example of NEA-GaAs

NEA-GaAs cathodes should exhibit MTE of less than 10 meV in infrared light due to the small effective mass of Γ valley electrons and the conservation of transverse momentum during emission[29]. However, the smallest MTE measured from these cathodes is in the 25-40 meV range[13, 21, 17].

Using the emission model discussed in section IIIA, we show that surface non-uniformities including atomic surface defects and surface reconstructions could explain the large MTE observed from GaAs.

In our model of the activated GaAs surface, we assume that the work function is uniform, and the barrier due at the interface is negligible. The surface is modeled only by a step rise in the potential along with a sudden change in effective mass as shown in figure 4.5a. For the activated GaAs (100) surface, the conduction band minimum (CBM) at the surface is ~ 0.5 V below the vacuum level[29], making the height of the step barrier $V = 0.5$ V. In our model we assume that the band bending is very gradual and hence ignore any slope to the CBM near the surface. This assumption is true for very lightly doped GaAs cathodes or for layered GaAs cathodes with un-doped top layer[17].

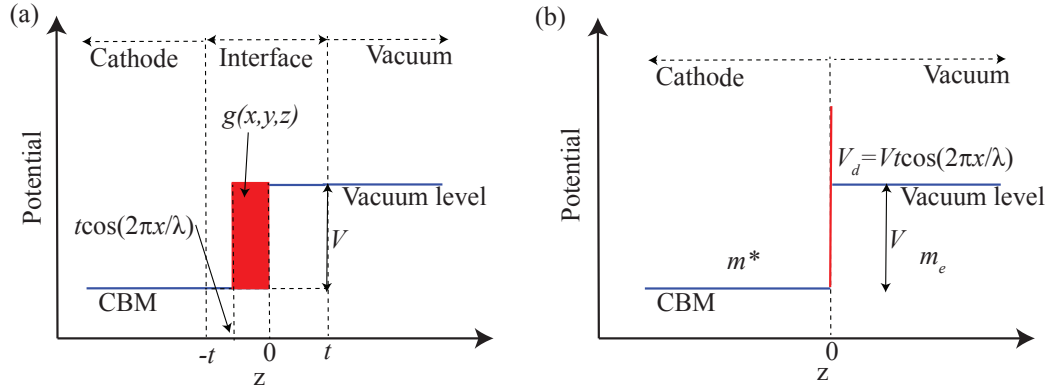


Figure 4.5: (a) Potential to model the GaAs surface. The non-uniformities are modeled using a small sinusoidal roughness of in the x direction (b) The sinusoidal roughness is approximated using a δ function.

The atomic defects, steps and reconstructions of the surface are modeled by introducing a sinusoidal surface ‘roughness’ in the x direction. The z position of the potential step at the interface changes due to this roughness and is given by $z = t \cos\left(\frac{2\pi}{\lambda}x\right)$, where $t = 1$ nm, making the rms roughness only 0.7 nm. λ is the periodicity of the surface roughness. As shown in figure 4.5b, this roughness can be approximated by a δ function barrier whose height is given by $Vt \cos\left(\frac{2\pi}{\lambda}x\right) = 0.5 \cos\left(\frac{2\pi}{\lambda}x\right)$ nm-V. For this approximation to be valid the wavelength of the electrons must be much larger than 1 nm. The MTE can be estimated from equation 4.17.

Figure 4.6a shows MTE as a function of the period of the surface roughness (λ) for various kinetic energies of emitted electrons. The transverse momentum of the incoming electrons was set to zero. Thus the MTE calculated is purely due to the effect of sub-nm scale roughness. We can see that the MTE can increase with increasing kinetic energy of the electrons.

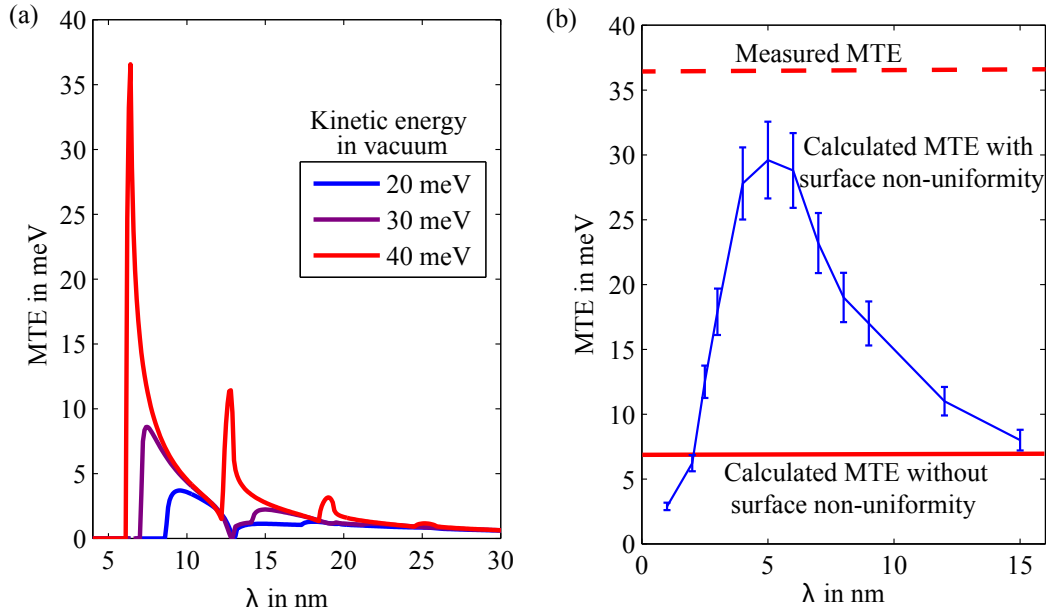


Figure 4.6: (a) Calculated MTE as a function of the period (λ) of the surface non-uniformity for various electron energies. A spike in MTE occurs whenever the electron energy is sufficient to allow scattering into a higher order transverse wave-vector. (b) Calculated MTE as a function of the period (λ) for a realistic distribution of incoming wave-vectors. The MTE measured experimentally and calculated without the surface non-uniformity are also shown.

A realistic distribution of the electron wave-vectors emitted from the surface was calculated from the Monte Carlo based electron transport simulation[29] for incident photon energy of 1.6 eV. The MTE from such a distribution was calculated using equation 4.17 with $t = 1$ nm. Figure 4.6b shows this MTE for various values of λ . The MTE obtained experimentally and from the Monte Carlo simulation without assuming any surface scattering are also shown.

Scattering occurs only when the electron wavelength is comparable to the period of the surface non-uniformities. Hence, the MTE calculated using the quantum model for surface non-uniformities initially rises with increasing λ

and then decreases. The MTE is comparable to the measured value if the period of non-uniformities is 4-6 nm. Thus it is possible to explain the higher MTE measured from GaAs cathodes.

Although we discuss a specific case of GaAs cathodes, a similar argument can be made for any cathode material. Hence, to obtain very low MTE it may be necessary to make the surface devoid of sub-nm scale roughness and essentially have an atomically perfect surface.

As the excess energy of the photons increases, electrons emitted have a higher kinetic energy and a smaller wavelength. For kinetic energy equal to 0.2 eV, the De Broglie wavelength becomes lower than 3 nm, questioning the δ function approximation. More general solutions to the scattering problem should be implemented to investigate this regime.

4.5 Conclusion

We investigated the effect of surface non-uniformities on the MTE of photocathodes. We conclude that work function variations that have spatial periods over 100 nm and can be treated classically can limit the minimum achievable MTE. Atomic scale defects and surface reconstructions can form a sub-nm scale roughness on the surface. Such a roughness should be modeled quantum mechanically and may limit the MTE to 20-30 meV. Thus to achieve the theoretical limit of MTE, one must obtain an atomically perfect surface with a uniform work function.

Surface uniformity of the practically used cathodes should be investigated.

Experimental tools like Kelvin Probe Force Microscopy should be used to characterize the work function variation over the surface to a nm resolution. Techniques like Atomic Force Microscopy can be used to image the quality of the surface and obtain the density and scale of the atomic defects. It may be possible to explain the discrepancy between measured and theoretically predicted values of MTE for several cathodes by incorporating the effect of surface non-uniformities.

This work was supported by the Department of Energy under grant number DE-SC0003965.

CHAPTER 5

AB-INITIO STUDIES OF Cs ON GaAs (100) AND (110) SURFACES

5.1 Abstract

GaAs with an atomic monolayer of Cs is one of the best known photoemissive materials. The results of density functional theory calculations of Cs adsorption on the GaAs(100)-(4×2) gallium-terminated reconstructed surface and the GaAs(110) surface are presented in this work. Coverage of up to 4 Cs atoms/nm² on GaAs surfaces has been studied to predict the work function reduction and adsorption energies accurately. The high mobility of Cs atoms on the (110) surface allows formation of ordered structures, whereas the low mobility of Cs of the (100) surface causes amorphous growth. Much of the content of this chapter was previously published in Ref. [31].

5.2 Introduction

GaAs activated using Cs is an excellent photoemitter and has found numerous applications as source of both spin polarized[85] and non-polarized electrons in photoinjectors [12] and as an infrared light sensor in image intensifiers[25]. An ideal photoemitter should have a high quantum efficiency (QE), low mean transverse energy (MTE) of the emitted electrons, a short response time, good lifetime and low sensitivity to non-ideal vacuum conditions. Despite its very stringent requirements on vacuum, GaAs activated using Cs remains an excellent photoemitter due to its high QE in visible and near infrared light and the

low MTE of emitted electrons[13].

The process of photoemission from activated GaAs has been best explained using Monte Carlo electron transport simulations within the framework of Spicer's three step photoemission model[29]. This model divides the process of photoemission into three steps: (i) the excitation of electrons by photon absorption, (ii) the transport of excited electrons to the surface, and (iii) the emission of electrons reaching the surface into vacuum. While the steps of excitation and transport are well understood, the emission of electrons into vacuum uses several ad-hoc assumptions to explain experimental results[29].

Assuming conservation of transverse momentum at the surface due to translational invariance and the small electron effective mass in the Γ -valley of the first conduction band in GaAs, the emitted electrons should exhibit very low MTE of less than 5 meV[63, 29]. However, even for the best quality GaAs(100) surfaces grown using molecular beam epitaxy, experimental observations indicate MTE values of 25-100meV[17]. The larger MTE values have been explained by introducing an ad-hoc scattering at the surface due to the non-conservation of transverse momentum. The cause of this scattering has not been understood. Understanding the structure of the Cs layer is important to identify the surface scattering mechanism responsible for the increased MTE.

Photoemission from GaAs can be obtained by depositing only 0.5-1 monolayer (ML) of Cs on the surface. Different authors define a monolayer of Cs differently, and hence to avoid confusion we do not use the monolayer notation and instead use the surface density of Cs atoms/nm², with the typical 1 ML thought to roughly correspond to 4-8 Cs atoms/nm².

The adsorption of Cs on GaAs has been studied for decades. Numerous surface studies of Cs on the (100) and (110) surfaces of GaAs have been performed using Auger spectroscopy, low energy electron diffraction (LEED) and scanning tunneling microscopy (STM). The two surfaces show very different Cs adsorption characteristics. Cs adsorbs on the (110) surface to form 1-D structures at low coverages. At higher coverages greater than 2.2 Cs atoms/nm² the lines form 2-D polygons which merge to form a (4×4) structure. This structure has been observed by LEED[86, 87] and STM[88, 89]. Formation of such structures is evidence that the Cs atoms are mobile on the GaAs (110) surface. On the other hand, both LEED and STM studies confirm the formation of an amorphous layer[90, 91, 92] on the (100) surface and no ordered 1-D or 2-D structures of Cs atoms are observed. Various experimental studies have characterized the Cs activation of the (100) and (110) surfaces by measuring the photoemission current, work function reduction, strength of the Auger Cs signal and Cs adsorption energies as a function of Cs dosage[86, 87, 90, 93, 94, 92, 95, 91, 96, 97]. However, a complete theoretical understanding of these characteristics and differences is still lacking.

Density-functional theory (DFT) has proven helpful in the study of the work function of various materials[98, 99, 100, 101, 102]. DFT correctly predicts that the adsorption of Cs on transition metal surfaces lowers the work function through the formation of a surface dipole[99]. DFT calculations for isolated Cs atoms adsorbed on As and Ga terminated GaAs(100) surfaces have shown that Cs is preferentially located surrounded by As[101, 102]. However, only low Cs coverages (< 1 atom/nm⁻²) and not all possible adsorption sites were considered.

In this paper, we report DFT calculations for Cs adsorbed on the Ga terminated (100) and the (110) surfaces of GaAs for Cs surface densities of up to 4 atoms/nm². For low Cs surface densities (<1 atom/nm²), we compute the diffusion activation energy for Cs atoms to move on the GaAs surface allowing us to compare the mobility of Cs atoms on the (110) and the (100) surfaces. The low mobility on the (100) surface can explain the formation of the amorphous Cs layer while the higher mobility on the (110) surface is consistent with the experimentally observed formation of the ordered (4×4) epitaxial layer. For higher Cs coverages, we show that the preferred adsorption sites of the Cs atoms change with the surface density of Cs atoms and find that the resulting work function reduction and the adsorption energies agree well with experimental data. Our study of Cs adsorption on GaAs surfaces demonstrates the feasibility of using computational approaches to discover new photoemissive surfaces and structures.

5.3 Simulation methods and details

5.3.1 Computational methods

All calculations are performed using the plane-wave DFT code VASP, which utilizes the projector-augmented wave (PAW) method[103, 104, 105]. Throughout this work, the generalized gradient approximation (GGA) with the Perdew-Burke-Ernzerhof (PBE) parametrization is used[106]. The PAW potentials describe for Ga and As assume a [Ar] core and for Cs a [Kr] 4d¹⁰ core, resulting in 3, 5, and 9 valence electrons, respectively. A plane-wave cutoff energy of 400 eV

and a $4 \times 4 \times 1$ k -point mesh ensure a convergence of the energy to 2 meV/atom. The structures are relaxed until the forces are below 0.01 eV/Å.

5.3.2 Surface structures

The calculations for both the gallium-terminated GaAs(100)-(4×2) surface and the GaAs(110) surface were performed using a slab geometry with a vacuum layer of 25 Å, which was found to be sufficient to make interactions between the slabs negligible. The number of atomic layers in both slabs was chosen sufficiently large to converge the surface energy to 1.3 meV/Å². The work function for each surface is determined by the difference between the highest occupied band of the surface slab and the electrostatic potential in the vacuum. The vacuum potential is taken as the average electrostatic potential half-way between the periodic slabs. To accurately describe the electrostatic potential in the vacuum region, a dipole correction is added along the direction perpendicular to the slabs.

Figures 5.1a and b show the slab for the GaAs(100)-(4×2) surface consisting of nineteen atomic layers and containing 140 atoms. The size of the cell was 7.995 Å \times 15.990 Å \times 50.440 Å. The (4×2) surface reconstruction of the Ga terminated (100) surface exhibits a dimer reconstruction[101]. After relaxation our calculations reproduced the previously computed structural parameters to an accuracy of 1%[101]. It is important to note that in this work we use the GaAs reconstruction on both sides of the slab and do not use hydrogen termination on one side as done in previous works[101, 107]. During relaxation atoms in the four outermost layers were allowed to move and the remaining atoms were

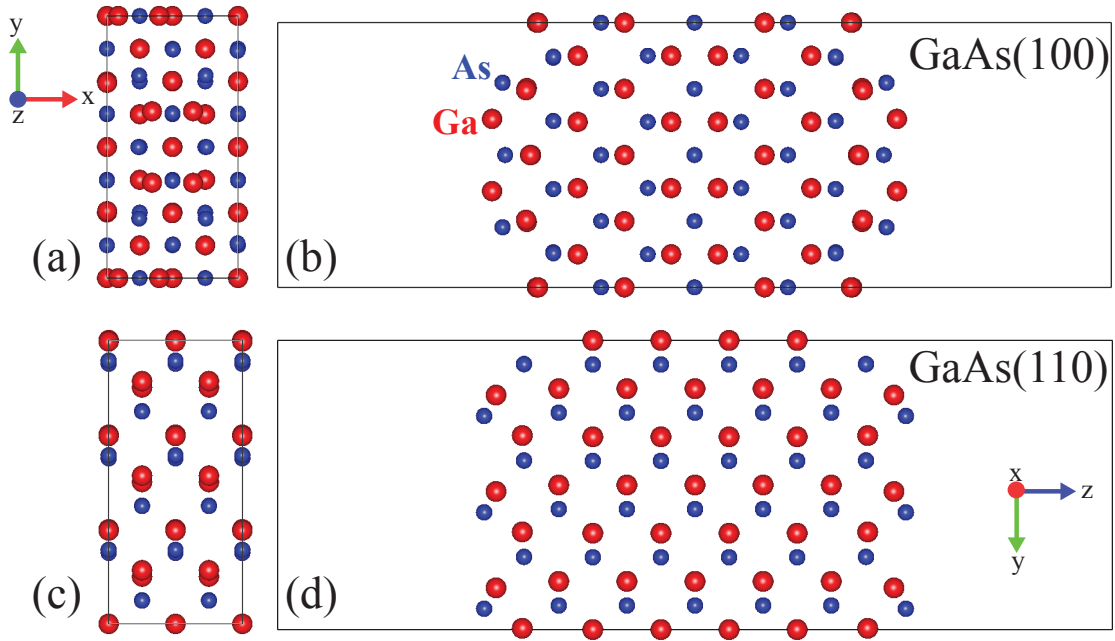


Figure 5.1: (Color online) (a) Top and (b) side view of the relaxed Ga terminated GaAs(100)-(4 \times 2) surface slab. (c) Top and (d) side view of the relaxed GaAs(110) surface. Both cells have a vacuum spacing of 25 Å, which sufficiently reduces interactions between the slabs. The Ga atoms are shown in red and the As atoms are shown in blue. For the (100) surface the x, y and z axes indicate the [011], [0 $\bar{1}$ 1] and [100] directions respectively. For the (110) surface the x, y and z axes indicate the [00 $\bar{1}$], [$\bar{1}$ 10] and [110] directions respectively.

kept fixed.

Figure 5.1c and d illustrate the computational cell for the GaAs(110) slab consisting of eleven atomic layers and containing 156 atoms. The size of the cell was 7.995 Å \times 16.961 Å \times 48.986 Å. The GaAs(110) surface is stable and does not show any reconstruction. Nevertheless, the surface As atoms relax outwards, to a position slightly above the surface Ga atoms.[108] Our DFT calculations reproduce the same behavior. During relaxation the atoms in the two outermost layers were allowed to move and the remaining atoms were fixed to the bulk

position.

To estimate the mobility of Cs atoms on GaAs surface, we calculate the energy barrier for surface diffusion. The energy barriers for pathways connecting the lowest energy adsorption sites are calculated using the nudged elastic band method[109, 110], allowing the atomic positions of the top two layers of the slab to relax.

5.3.3 Cs adsorption calculations

We study several configurations for five different surface densities of Cs atoms, corresponding to 1-5 Cs atoms on the simulation cell surface. Cs atoms are placed at random x and y positions and at a z position 3.2 \AA away from the outermost surface atom with a minimum allowed Cs-Cs distance of 4.0 \AA . The Cs atoms along with the outermost 4 layers for the (100) surface and 2 layers for the (110) surface of the GaAs slabs were allowed to relax. This is repeated several times for each density of Cs atoms to obtain a statistical sampling. To reduce the computational cost of generating the relaxed configurations, different Cs configurations are placed on the top and bottom surface of the slabs, doubling the number of relaxed configurations. The number of relaxed configurations, n , is 20 for 1 to 5 Cs atoms on the (110) surface. For the (100) surface, the number of configurations is 20 for 1 to 3 Cs atoms, 18 for 4 Cs atoms case and 12 for 5 Cs atoms.

The energy for each relaxed Cs configuration is obtained by separate calculations where Cs atoms are only adsorbed on one surface. The total adsorption energy of N number of Cs atoms per surface per simulation cell is given by

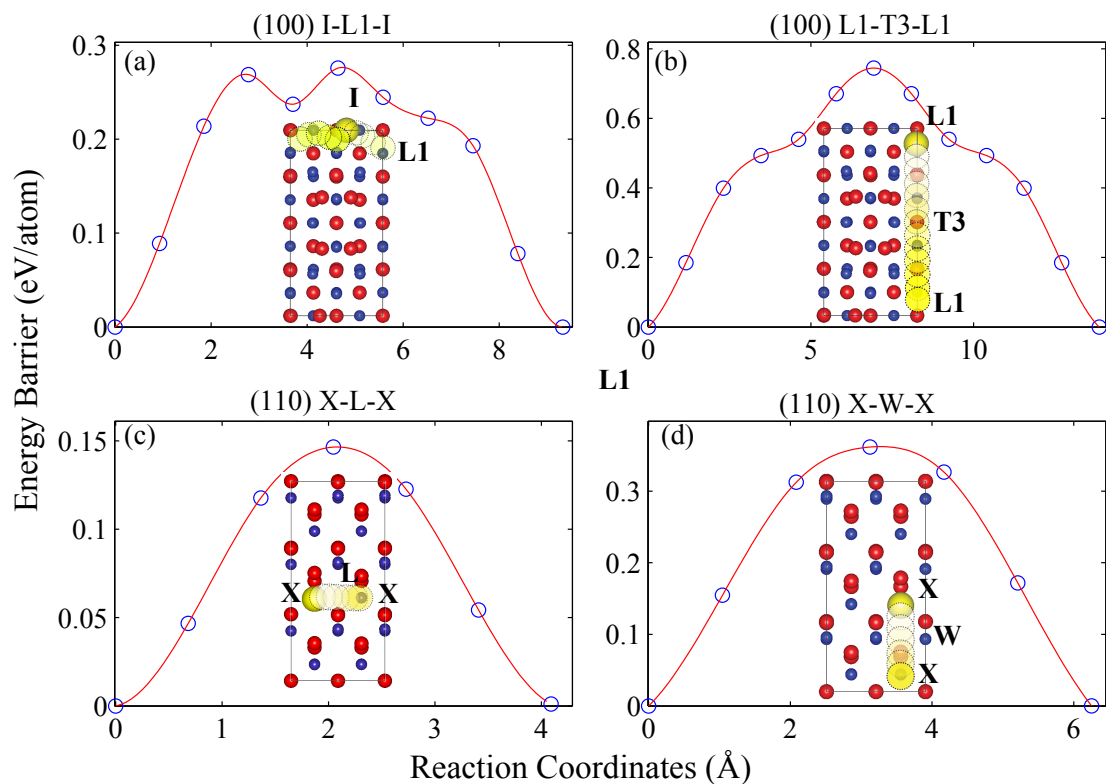


Figure 5.2: The energy barrier for the diffusion of Cs, (a) along the trench $[01\bar{1}]$ direction) on GaAs(100), (b) across the dimer $[01\bar{1}]$ direction) on GaAs(100), (c) between two adjacent X sites along the $[00\bar{1}]$ direction on GaAs(110), and (d) between two adjacent X sites along the perpendicular $[1\bar{1}0]$ direction on GaAs(110). Ga atoms are shown in red and As atoms in blue. The initial position of the diffusing Cs atom is shown as a yellow sphere, subsequent images along the minimum energy path of the Cs atom are shown as circles with the darkest circle denoting the final position.

$\Delta E_N = (E_{\text{slab}} + NE_{\text{Cs}}) - E_{\text{slab+Cs}}$, where E_{slab} is the energy of the relaxed GaAs slab without any Cs atoms, E_{Cs} is the energy of a free Cs atom in vacuum, N is the number of adsorbed Cs atoms, and $E_{\text{slab+Cs}}$ is the energy of the slab with the relaxed Cs atoms on one surface.

Thermodynamic averages at room temperature for observables, Q_N , as a function of the number of Cs atoms, such as the adsorption energy, Cs atom position distribution, or work function, are estimated assuming classical thermodynamics using

$$\langle Q_N \rangle = \frac{\sum_{i=1}^n Q_N^i \exp\left(-\frac{\Delta E_N^i}{k_B T}\right)}{\sum_{i=1}^n \exp\left(-\frac{\Delta E_N^i}{k_B T}\right)}, \quad (5.1)$$

where k_B is the Boltzmann constant, $T = 293\text{K}$ corresponds to room temperature, and the superscript i denotes the i^{th} configuration. The thermodynamically weighted standard deviation, σ_Q , is given by

$$\sigma_{Q_N} = \sqrt{\langle (Q_N - \langle Q_N \rangle)^2 \rangle}. \quad (5.2)$$

The chemical potential of Cs is defined as the energy released by adding a Cs atom to the surface and is estimated from the average adsorption energies by $\mu_{\text{Cs}} = \langle \Delta E_N \rangle - \langle \Delta E_{N-1} \rangle$. The work function is defined as the energy difference $\langle W \rangle = \langle E_{\text{vac}} - E_{\text{fermi}} \rangle$ between the energy of the electrostatic potential in the vacuum region, E_{vac} , and the energy of the highest occupied orbital in the slab, E_{fermi} [98, 99, 100].

The position distribution of Cs atoms on the surface is calculated using a Gaussian smearing. For the purpose of visualization in figure 5.3, the (x, y) coordinates of the Cs atoms are convolved with a truncated 2-D Gaussian function of width $\sigma = 1.75 \text{ \AA}$ ($1/\sqrt{2}$ times the covalent bonding radius of Cs) and a truncation radius equal to σ . The position distributions are averaged following

Eq. (5.1).

5.4 Results and Discussion

5.4.1 Mobility of Cs at low coverages

Figure 5.2 shows the low-energy equilibrium positions of a single Cs atom on the (110) and (100) surfaces of GaAs and the minimum energy path for Cs diffusing between the equilibrium positions. For the (100) surface the most stable position, labeled as I , has an adsorption energy of 2.55 eV and lies in a trench away from the dimer reconstruction. Figures 5.2(a) and (b) illustrate the minimum energy paths for diffusion along the trench ([011] direction) and to cross over the dimer reconstruction ([01 $\bar{1}$] direction) on GaAs(100), proceeding through a metastable minimum, labeled $L1$. In order to move along the trench (in the [011] direction), the Cs atom follows the path $I - L1 - I$ with a low energy barrier of only 0.28 eV. The crossing over the dimer reconstruction proceeds through the saddle point labeled $T3$ with a resulting energy barrier of $E_{T3} - E_I = 0.96$ eV.

For the (110) surface the most stable position, labeled as X , has an adsorption energy of 1.71 eV. Figure 5.2(c) and (d) illustrate the minimum energy paths between neighboring X positions. The energy barrier for the Cs atom to move along the [00 $\bar{1}$] direction is 0.15 eV, while the barrier to move in the perpendicular direction ([1 $\bar{1}$ 0]) is 0.35 eV. The energy barriers are denoted as L and W , respectively. The sizable difference in the energy barrier for diffusion along the trench and across the dimer reconstruction demonstrates that the diffusion of Cs on GaAs(110) is anisotropic, which might be responsible for the experimentally

observed formation of 1-D structure as discussed below.

The jump frequency, Γ , for the surface diffusion of an isolated Cs atom between adjacent equilibrium position follows an Arrhenius behavior,

$$\Gamma = \nu \exp\left(-\frac{\Delta E_a}{k_B T}\right), \quad (5.3)$$

where the prefactor of the jump frequency is approximated as $\nu \approx 10^{13}$ Hz for a GaAs surface[93] and ΔE_a is the barrier the Cs atom needs to overcome during the jump.

At room temperature, for the (110) surface the barriers of $\Delta E_a = 0.15$ eV along the $[00\bar{1}]$ direction and of $\Delta E_a = 0.35$ eV along the perpendicular $[1\bar{1}0]$ direction result in jump frequencies of $\Gamma = 3 \times 10^{10}$ Hz and 1×10^7 Hz, respectively. This corresponds to an isolated Cs atom diffusing a root-mean square (RMS) distance of $\approx 100 \mu\text{m}$ and $\approx 2.5 \mu\text{m}$ per second along the two perpendicular directions, respectively. The 40 times larger RMS displacement of Cs along the $[00\bar{1}]$ direction compared to the $[1\bar{1}0]$ direction is likely the reason Cs atoms arrange into 1-D line structures at very low Cs surface densities and 2-D structures at higher Cs densities as observed experimentally in STM studies[88, 89].

In contrast, on the (100) surface, at room temperature, the large energy barrier of $\Delta E_a = 0.96$ eV along the $[01\bar{1}]$ direction to cross the dimer reconstruction results in $\Gamma = 5 \times 10^{-4}$ Hz, making the Cs atom practically immobile in this direction. The barrier along the trench ($[011]$ direction) is lower with $\Delta E_a = 0.28$ eV resulting in $\Gamma = 2 \times 10^8$ Hz. The Cs atom can be mobile in this direction and can form 1-D chains. However, cluttering of Cs atoms on the (100) results in a severely modified surface potential as seen from figure 5.3(a)-(c). This may cause the Cs to become immobile in both directions, resulting in the amorphous growth of Cs on the surface as observed experimentally[91].

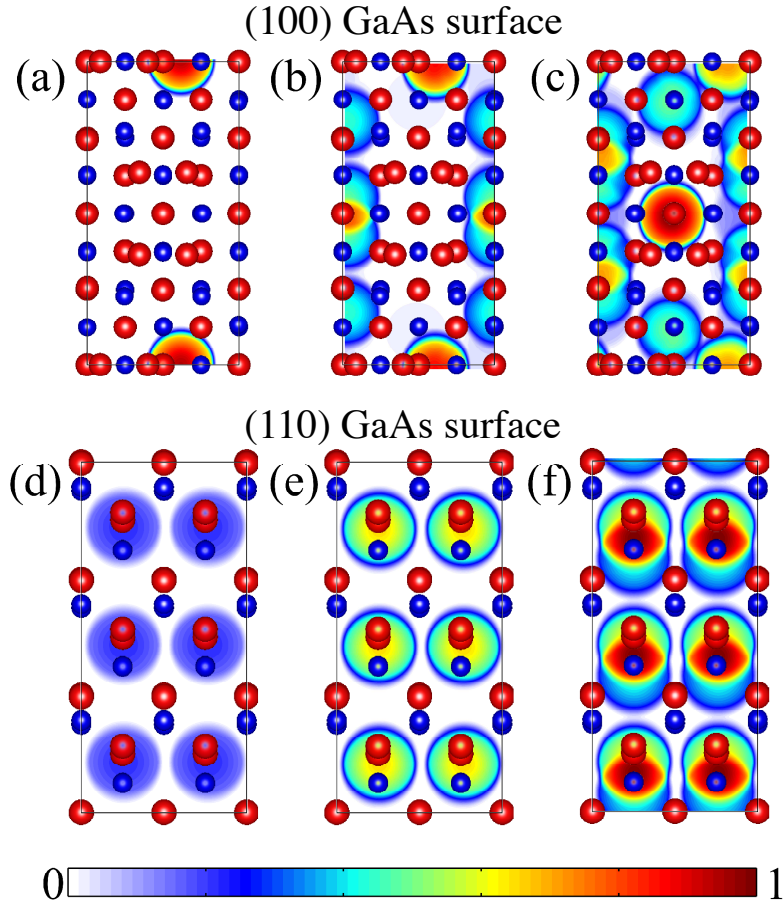


Figure 5.3: Top view of the Cs position distributions on the (100) surface for Cs surface densities of (a) 0.78, (b) 2.35, and (c) 3.91 nm⁻², respectively. Top view of Cs position distributions on the (110) surface for Cs densities of (d) 0.74, (b) 2.21, and 3.69 nm⁻², respectively. The Cs position distributions are overlaid on the surface atoms of the GaAs slabs. The blue circles represent the As atoms and the red circles the Ga atoms. The intensity of the position distribution is indicated by the color bar. The position distributions on the (100) and (110) surfaces are normalized to the maximum of the distribution on that surface over all the Cs densities.

It is interesting to note that at temperature of 77 K $\Gamma = 1 \times 10^{-10}$ Hz for $\Delta E_a = 0.35$ eV, making the Cs atom immobile on the (110) surface too. Thus, At low temperatures, an amorphous growth of Cs layer might happen on the (110) surface too.

5.4.2 Cs position distribution

Figure 5.3 shows the Cs position distributions as a function of Cs surface densities for the (100) and (110) surfaces. The Cs surface distribution on the (100) surface shows an interesting dependence on surface density. As shown in Fig. 5.3(a), for low Cs coverages, the Cs atoms stay away from the raised dimer reconstruction and are preferentially located in the trenches. As the Cs density increases in Fig. 5.3(b), Cs starts to prefer the areas around the dimer and for the highest density studied, Cs atoms preferentially sit atop the dimer reconstruction as shown in Fig. 5.3(c). Electron energy loss spectroscopy (EELS) shows the appearance of peaks characteristic to plasmonic oscillations in 2-D metallic islands at a Cs coverage of about 0.5ML[97]. The appearance of these peaks has been interpreted as a phase transformation of the Cs layer in which isolated Cs atoms form 2-D clusters on the GaAs (100) surface. This change observed in the EELS spectra and the phase transformation could be caused by the changes in the distribution of the Cs surface positions.

For the (110) surface, Figs. 5.3(d)-(f) show that the Cs atoms essentially prefer to stay inside or near the center of the rectangle formed by the surface As atoms at all surface densities. As the Cs density increases the interactions between the Cs atoms simply broadens the position distribution (Fig. 5.3(f)).

5.4.3 Work function change and adsorption energy

Figure 5.4(a) shows that the predicted work function reduction as a function of Cs surface density agrees well with the experimental results for both GaAs surfaces. The work function reduction is caused by the change in surface dipole

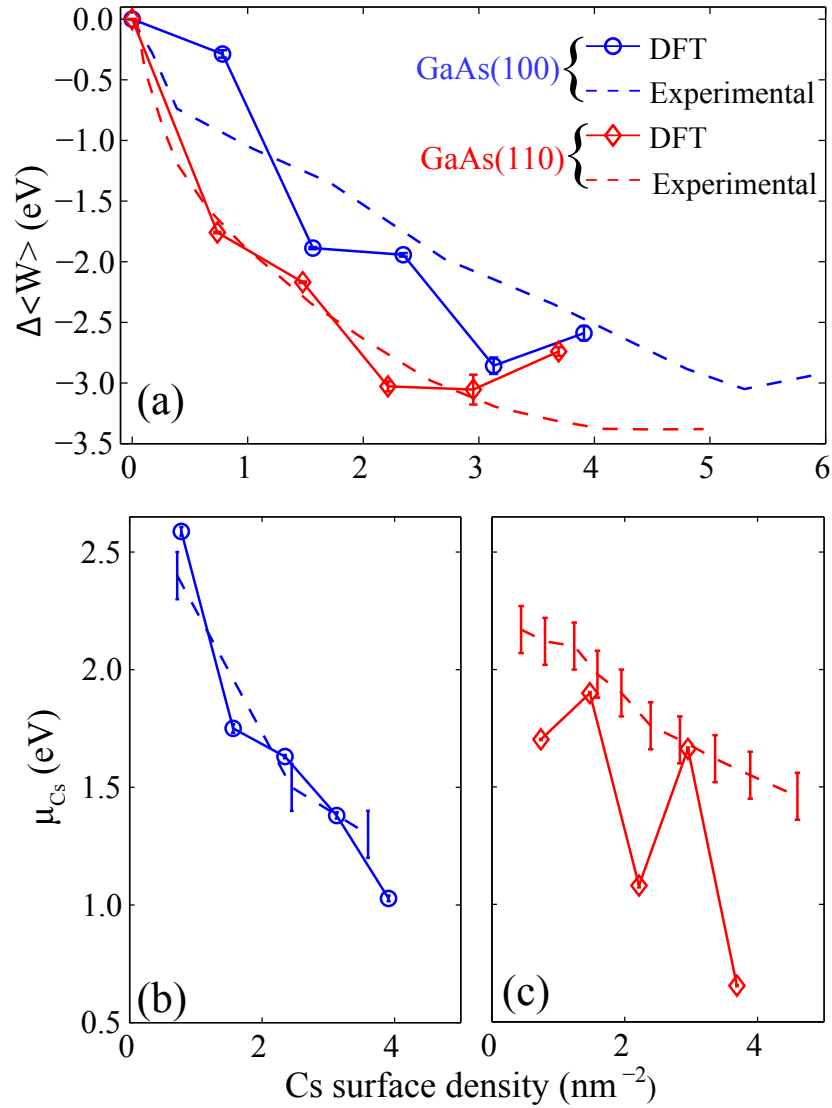


Figure 5.4: (a) Work function reduction ($\Delta\langle W \rangle$) as a function of Cs surface density for the GaAs(100) and the GaAs(110) surfaces. The experimental values[91,93] agree well with those calculated using DFT. Chemical potential of adsorbed Cs as a function of Cs surface density for (b) the GaAs(100) and (c) the GaAs(110) surfaces. The experimental values[94,95] are also presented.

due to charge transfer from the Cs ad-atoms to the GaAs substrate. The work function reduction (ΔW) is proportional to the change in the surface dipole per unit area (Δp) and is given by $\Delta W = \frac{e}{\epsilon_0} \Delta p$, where e is the electron charge and ϵ_0 the vacuum permittivity. At very low coverages the surface Cs dipoles do not interact and the work function reduces with increasing Cs coverage. However at higher Cs densities the work function goes through a minimum and then increases due to the interaction between the Cs atoms[99], finally reaching the work function of bulk Cs at very high Cs densities. The simulation shows a slight increase in the work function at Cs surface densities close to 4 nm^{-2} but is still much smaller than the calculated work function of bulk Cs of 1.99 eV. Simulations at higher Cs densities would be needed to confirm the expected rise in work function. Work function at higher Cs surface densities, close to 4 nm^{-2} , show a variation of about 100 meV. This work function variation on the surface could lead to the observed high values of MTE[29].

Figure 5.4(b) shows how the chemical potential of Cs varies with the Cs surface density for the (100) surface. We see that the agreement between the experimental results and the DFT calculations is quite good for the (100) surface. The continuous reduction in the Cs chemical potential suggests a homogeneous coverage of Cs on the surface.

Figure 5.4(c) shows the dependence of the Cs chemical potential on the surface density for the (110) surface. The DFT calculations predict a non-monotonic behavior, suggesting a possible phase separation of the Cs on the surface and that Cs atoms could preferentially form clusters. Such clustering is indeed observed on the (110) surface using STM in the form of 1-D and 2-D Cs structures[88, 89]. As the chemical potential is the energy released by adding

a Cs atom to the surface, a higher chemical potential corresponds to a lower energy structure of Cs on the surface. Hence, the experimentally observed 1-D and 2-D structures have lower energy than a uniform Cs coverage causing the discrepancy in the observed and calculated adsorption energies in Fig. 5.4(c). Simulating these structures is beyond the scope of the DFT modeling due to the large size of the required simulation cell. The periodic boundary conditions add constraints due to which formation of lower energy structures is not possible for certain Cs coverages. For these coverages the chemical potential has a lower value than the experimental observations causing spikes in figure 5.4(c). This behavior is thus an artifact of the constraints enforced by a small simulation cell and periodic boundary conditions.

5.5 Conclusion

Using density-functional calculations, we show that the formation of different surface structures observed in the Cs adsorption on the (110) and the (100) surfaces of GaAs can be attributed to the difference in the mobility of Cs atom on these two surfaces. At room temperature, Cs is very mobile on the (110) surface. This allows the formation of low-energy ordered 1-D and 2-D structures at low coverage and at higher coverage the growth of ordered epitaxial layers on the (110) surface. On the (100) surface at low coverages, Cs atoms are much less mobile causing them to deposit in an amorphous fashion. Thermodynamic averages of the DFT energies accurately predict the Cs adsorption energy and the work function reduction of the GaAs surface as a function of Cs coverage. The computational expense currently limits this approach to defect-free surfaces. However, the good agreement of the results with experimental data

indicates that defects do not have a strong affect on the adsorption energy and work function.

This work shows that it is possible to computationally screen materials for surface structures and compositions that effectively lower the workfunction. The computational approach is general and applicable to study the workfunction for the adsorption of other alkali metals like Li, Na and K on various III-V semiconductor surfaces.

This work is supported by National Science Foundation under Awards No. DMR-0807731, No. DMR-1056587, through the Cornell Center for Materials Research under Award No. DMR-1120296, and by the Department of Energy under Award No. DE-SC0003965. The research used computational resources of the Texas Advanced Computing Center under Contract No. TG-DMR050028N.

CHAPTER 6

2-D ENERGY ANALYZER FOR LOW ENERGY ELECTRONS

6.1 Abstract

A 2-D electron energy analyzer is designed and constructed to measure the transverse and longitudinal energy distribution of low energy (< 1 eV) electrons. The analyzer operates on the the principle of adiabatic invariance and motion of low energy electrons in a strong longitudinal magnetic field. The operation of the analyzer is studied in detail and a design to optimize the energy resolution, signal to noise ratio and physical size is presented. An energy resolution better than 6 meV has been demonstrated. Such an analyzer is a powerful tool to study the process of photoemission which limits the beam quality in modern accelerators. Much of the content of this chapter was previously published in Ref. [21].

6.2 Introduction

The maximum achievable brightness from photoinjectors that provide bright sub-picosecond electron bunches is limited by the transverse energy spread of electrons obtained from the photocathode[7]. Various photoemission properties like quantum efficiency (QE), transverse energy spread and response time, limit the performance of photoinjectors. It is important to understand the process of low energy photoemission to optimize the photoemission properties to improve the performance of photoinjectors. However, the process of low electron energy

(< 1 eV) photoemission is not well understood. A lack of consistent experimental data is the major cause of this.

Longitudinal (along the normal to the photoemitting surface) and transverse (along the photoemitting surface) energy distributions of photoemitted electrons are the key observables to develop our understanding of the photoemission process. Several techniques exist to measure the total and longitudinal energy distributions of photo emitted electrons of energies less than 1 eV[111, 112, 113]. These essentially rely on retarding field analyzers. Transverse energy distributions can also be measured by providing a longitudinal acceleration to electrons generated out of a point and imaging the spot size after allowing the beam to expand in a drift or longitudinal acceleration region[20, 114, 62, 25]. The mean transverse energy (MTE) of electrons can be measured using emittance measurement techniques[22, 13] in photoinjectors.

Simultaneous measurement of longitudinal energy and transverse energy, or equivalently, total energy and emission angle, is more involved. In principle, advanced hemispherical energy analyzers typically used for Angle Resolved Photoemission Spectroscopy studies can be used[19] for this purpose. However, their use is limited to higher energy (> 1 eV) electrons because of their sensitivity to stray magnetic fields and work function variations. Further, they are expensive and have a limited angular range (typically < 40°). Another technique relying on crossed electric and magnetic fields between two parallel plates has been proposed[115], but was never realized to our knowledge due to the complex mathematical transformations involved in extracting the distributions from the raw data.

A 2-D energy analyzer capable of measuring transverse and longitudinal

energy distributions simultaneously was developed and used to measure low energy photoelectrons emitted from cesiated GaAs photocathodes by Orlov *et al*[60]. This analyzer utilizes the principle of adiabatic invariance and motion of low energy electrons in a strong longitudinal magnetic field to obtain the energy distributions with a resolution better than 17 meV. The analyzer can accept electrons emitted at all angles and can measure low energy electrons accurately.

In this paper, we perform a detailed analysis of the principles of operation of the 2-D analyzer described above, highlighting the factors that limit the energy resolution, signal to noise ratio and the physical size of the setup. Guided by this analysis, a 2-D energy analyzer is designed and built to optimize the fore-mentioned features. The new design demonstrates nearly three fold increase in the energy resolution and more than a 50 fold gain in signal to noise ratio as compared to the previously reported results[60]. It is compact with a length less than 50 cm.

The new design makes the analyzer better, cheaper and easier to deploy making it a practical tool for low energy photoemission diagnostics.

6.3 Theory of low energy electron beams in strong magnetic fields

6.3.1 Adiabatic invariance and energy conservation

In a longitudinal magnetic field, electrons follow a helical path around the magnetic field lines. The radius of gyration depends on the transverse energy of the

electrons and is given by

$$r_g = \frac{\sqrt{2m_e W_\perp}}{eB} \quad (6.1)$$

where W_\perp is the transverse kinetic energy, B is the magnetic field strength, m_e is the electron mass and e is the magnitude of the electron charge.

The frequency of the helical motion is given by

$$\omega = \frac{eB}{m_e} \quad (6.2)$$

and the pitch of the helix is given by

$$p = \frac{2\pi \sqrt{2m_e W_\parallel}}{eB} \quad (6.3)$$

where W_\parallel is the longitudinal kinetic energy of the electron.

The property of adiabatic invariance implies that in a longitudinal magnetic field the transverse energy of electrons varies directly with the strength of the magnetic field, if the latter changes gradually. The constant of proportionality is called the adiabatic invariant and is given by [116].

$$\mu = \frac{W_\perp}{B} \quad (6.4)$$

In our case, the magnetic field strength varies in the longitudinal (z) direction. Hence the transverse energy of the electron changes as it moves in the z direction.

The condition of adiabatic invariance holds true when the adiabaticity parameter ψ , defined as,

$$\psi = \frac{p}{B} \left| \frac{dB}{dz} \right| \quad (6.5)$$

is negligible compared to unity[117].

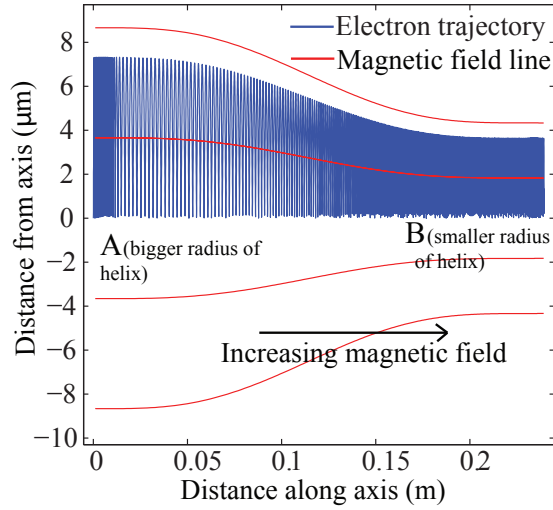


Figure 6.1: Trajectory of the electron in a longitudinally varying magnetic field traveling from A to B. The guiding center follows the magnetic field line. The radius of gyration reduces and the transverse energy increases with increasing magnetic field.

A consequence of the adiabatic invariance is the variation of the radius of the helix formed by the electron. The square of the radius is inversely proportional to the strength of the magnetic field. Thus the radius of the helix reduces with increasing magnetic field strength as shown in figure 6.1.

Another important property is the conservation of energy of the electron in a magnetic field. This implies, for a particular electron,

$$W_{\perp} + T = C \quad (6.6)$$

where C is a constant and the total longitudinal energy, $T = W_{\parallel} - V$, is the sum of the longitudinal energy (W_{\parallel}) and the negative electrostatic potential ($-V$) when W_{\parallel} is expressed in eV. To be able to directly add the energies to the electrostatic potential, all energies in this article are assumed to be expressed in eV. The negation of the electrostatic potential is to account for the negative charge of the electron.

Adiabatic invariance implies that the transverse energy (W_{\perp}) changes only with the magnetic field strength and not with the electrostatic potential. Change in the electrostatic potential (V) causes only the longitudinal energy (W_{\parallel}) to change, keeping T constant. Change in the magnetic field strength causes both the transverse energy and the longitudinal energy to change to satisfy the adiabatic invariance and the conservation of energy, creating a coupling between the two energies. The energy analyzer exploits this coupling to obtain the transverse energy by measuring the longitudinal energy before and after the coupling.

6.3.2 Motion of the guiding center

The helical motion of the electrons can be treated as a fast circular motion around a relatively slowly moving point called the guiding center. Below we show that in a cylindrically symmetric system, the guiding center of low energy electrons follows the magnetic field lines when projected on the r-z plane.

The velocity of the guiding center of the helix followed by an electron in a magnetic field is given by

$$\mathbf{v} = v_{\parallel} \mathbf{b} + \frac{\mathbf{b}}{eB} \times [mv_{\parallel}^2 (\mathbf{b} \cdot \nabla) \mathbf{b} + \mu \nabla B - e\mathbf{E}] \quad (6.7)$$

where v_{\parallel} is the magnitude of the velocity in the direction parallel to the magnetic field, \mathbf{b} is the unit vector in the direction of magnetic field and \mathbf{E} is the electric field [118].

The first term in the above equation gives the component of the velocity parallel to the magnetic field while the second term gives the velocity perpendicular to the magnetic field. Due to the cylindrical symmetry, \mathbf{B} and \mathbf{E} have

components only in \hat{r} and \hat{z} directions and are independent of the azimuthal angle. Hence, in this case, the second term has only the azimuthal component. Therefore the component of velocity that is perpendicular to the magnetic field has only the azimuthal component. Hence when projected on the r-z plane, the guiding center follows the lines of magnetic field. This effect causes the electrons to stay focused and form a beam in the analyzer.

6.3.3 Verification by simulation

The adiabatic invariance, energy conservation and the motion of the guiding center was validated using electron tracking simulations. Electric and magnetic field maps of the energy analyzer were computed using POISSON SUPERFISH[?]. The trajectory of the electron in these realistic field maps was obtained by integrating the equations of motion using an 8-stage symplectic implicit integrator[77]. Figure 6.1 shows the trajectory of an electron obtained by such a simulation.

The energies obtained from the electron tracking throughout the analyzer matched with those obtained from equation A.7 to an accuracy of better than 1 meV, showing that the assumptions about the adiabatic invariance and energy conservation are indeed valid. It was also verified that the guiding center of the trajectory follows the magnetic field lines when projected onto the r-z plane to an accuracy of $0.1 \mu\text{m}$.

6.4 Description of the setup and measurement

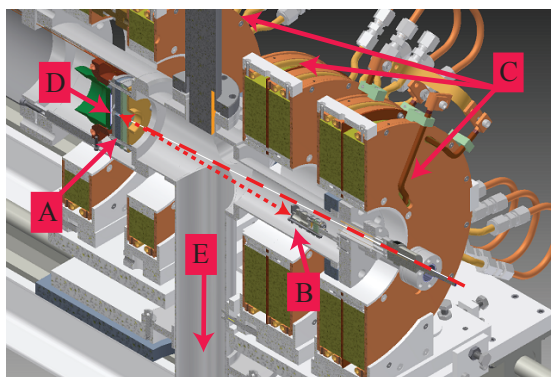
We present the working principle of the analyzer in some detail in addition to what can be found in previous literature [60, 117, 119] for convenience of the reader and to explain how our design is improved beyond the original implementation.

6.4.1 Description of setup

The design presented here is a modification of the energy analyzer developed by Orlov *et al*[60, 117, 119]. Figure 6.2 shows a model of the entire setup.

The setup consists of an electron emitter followed by a set of electrodes called the ‘gun’, a drift space and another set of electrodes called the ‘retarding field analyzer’ (RFA). Figures 6.3a and 6.3b show the detailed design of the gun and RFA electrodes. All the electrodes are cylindrically symmetric with a central hole through which the electron beam can pass. The ‘gun’ consists of the pierce electrode, the marking electrode and two accelerating electrodes. The pierce and marking electrodes are shorted and the two accelerating electrodes are grounded. The RFA consists of a shield, the retarding electrode, a pinhole and a collector.

The entire setup is immersed in a strong longitudinal magnetic field of larger than 400 G produced by four solenoid coils. The strength of the magnetic field increases from B_i at the marking electrode in the gun to $B_f = \alpha B_i$ at the retarding electrode in the RFA. The magnetic field is produced by 4 solenoid coils whose currents can be changed individually allowing us to change α from 1 to 4.2 and



A: Gun
 B: RFA
 C: Solenoid coils
 D: Photoemitter
 E: Pumping ports
 Laser
 Electron beam

Figure 6.2: Cross-section of the model of the energy analyzer. Corrector coils used to correct for the misalignments of the coils with the energy analyzer axis are not shown.

keeping $\frac{dB}{dz}$ and $\frac{d^2B}{dz^2}$ negligible in the gun and RFA regions to improve the resolution of the analyzer.

All electric and magnetic fields in the setup are cylindrically symmetric. This causes the guiding center of the helices formed by the electrons to follow the magnetic field lines when projected onto the r - z plane. If the maximum transverse energy of emitted electrons is 1 eV and we have a minimum magnetic field of 400 G in the analyzer, the radius of gyration of electrons around the magnetic field lines is less than $100 \mu\text{m}$. This confines the electrons near the axis of the analyzer to form a beam that travels from the emitter towards the collector. Small corrector coils are used to correct for the misalignments the solenoid coils have with the analyzer axis and guide the beam to the center of the RFA.

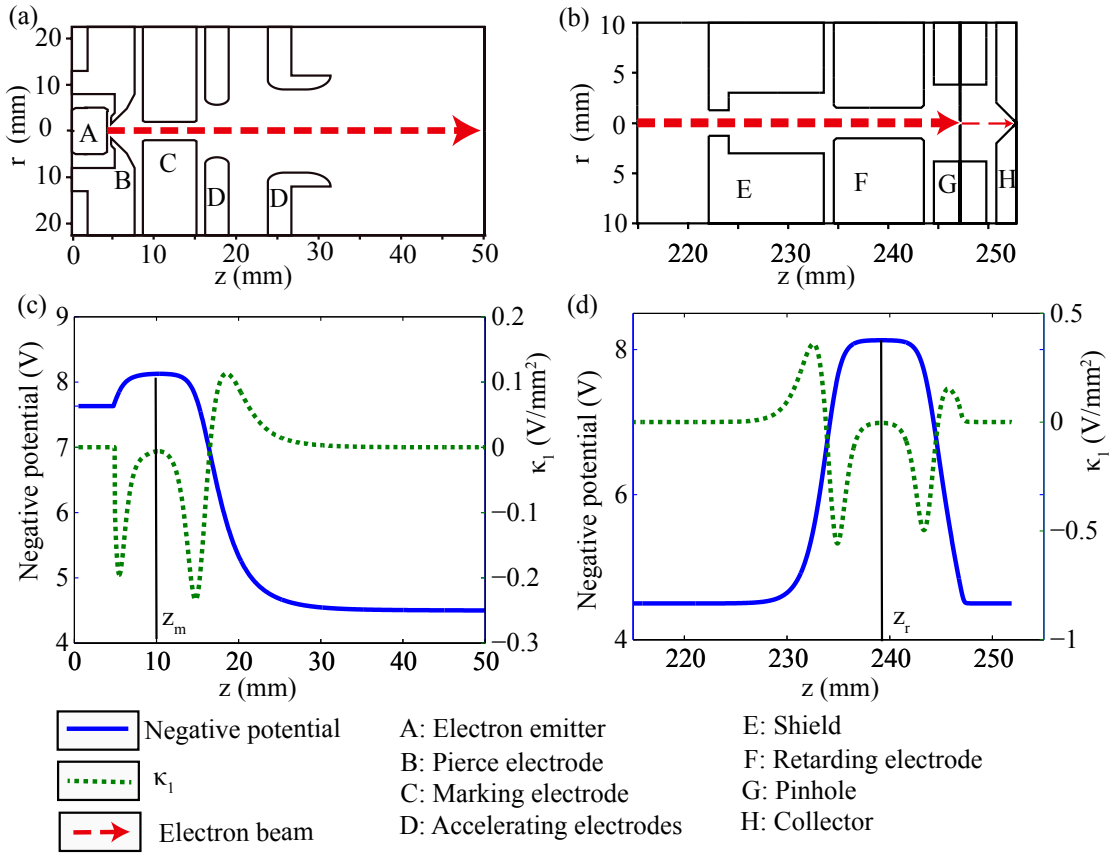


Figure 6.3: (a) Cross section of the gun electrodes, (b) Cross section of the RFA electrodes, (c) Potential and κ_1 on the axis in the gun calculated using POISSON SUPERFISH. For this calculation the potential in the emitter surface was set to $V_e = -7.63$ V, the potential on the pierce and marking electrode surface was set to $V_m = -8.13$ V and the potential on the surface of the accelerating electrodes was set to $F_c = -4.5$ V. Note that $\kappa_1(z_m) < 0.01\text{V/mm}^2$, where $z = z_m$ is the point of maximum potential barrier. (d) Potential and κ_1 on the axis in the RFA calculated using POISSON SUPERFISH. For this calculation the potential on the surface of the shield, pinhole and collector was set to $F_c = -4.5$ V and the potential on the retarding electrode surface was set to $V_r = -8.13$ V. Note that $\kappa_1(z_r) < 0.01\text{V/mm}^2$, where $z = z_r$ is the point of maximum potential barrier. $\kappa_1(z)$ is the negative of the second derivative of the electrostatic potential on axis w.r.t. z as shown in section IV B.

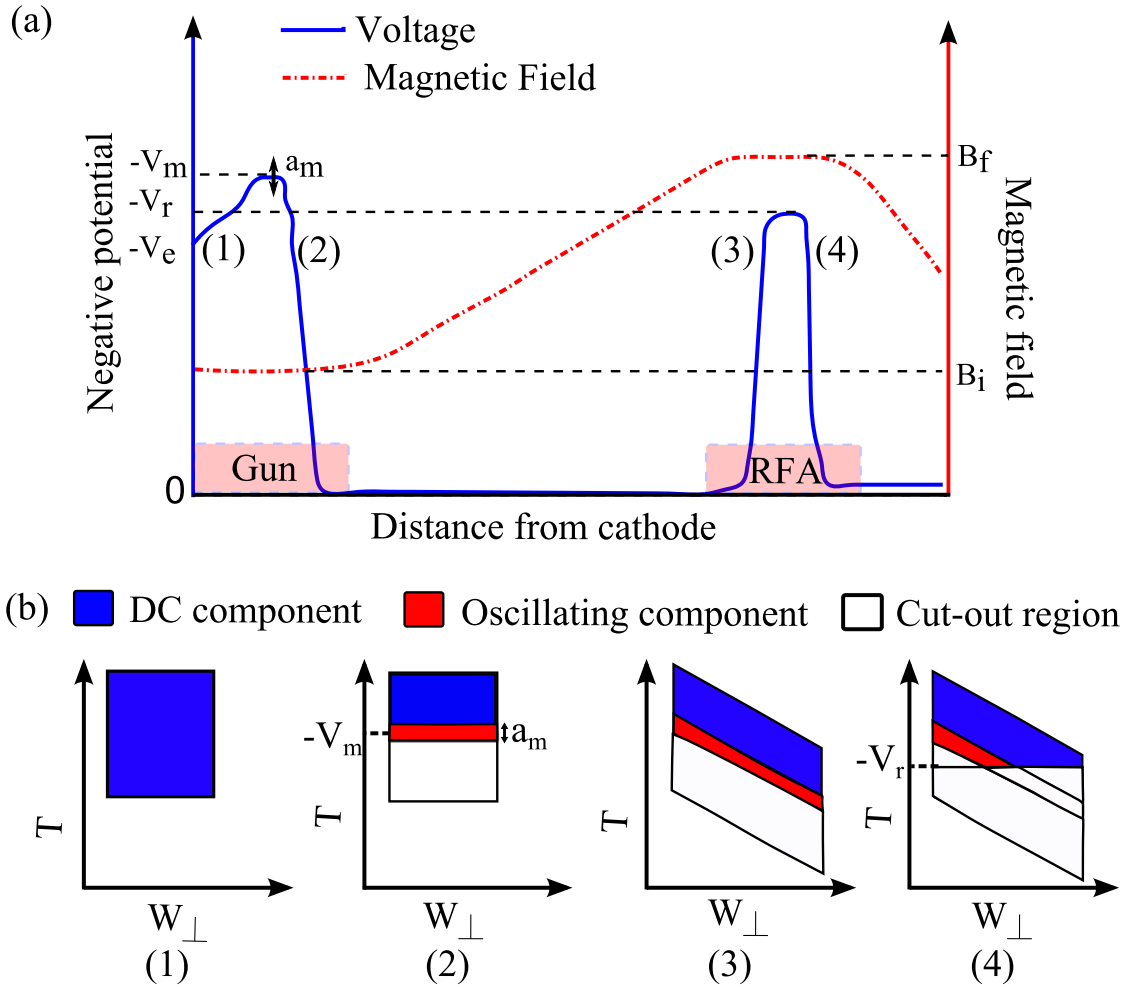


Figure 6.4: (a) a typical electrostatic potential and longitudinal magnetic field setup on axis of the analyzer. (b) evolution of a hypothetical square-shaped, uniform electron distribution as it propagates through the energy analyzer at various locations (1-4) shown in figure 6.4a.

6.4.2 Marking of electrons with a particular longitudinal energy

The electron emitter in the analyzer is biased to a voltage ϵ_e . The electrostatic potential right outside the emission surface is

$$V_e = \epsilon_e - F_e \tag{6.8}$$

where F_e is the work-function of the photoemissive surface in eV.

Let $W_{\parallel e}$ be the longitudinal energy and $W_{\perp e}$ be the transverse energy of an electron just outside the cathode. Thus, just outside the emitter, the total longitudinal energy is given by

$$T_e = W_{\parallel e} - V_e \quad (6.9)$$

The magnetic field (B_i) in the gun section is constant. Hence, owing to the adiabatic invariance, the total longitudinal energy and the transverse energy are constant in this section. Thus, the total longitudinal energy at the marking electrode equals T_e , the total longitudinal energy at the emission surface. The marking electrode is biased with a DC voltage, ϵ_m , along with a small sinusoidal oscillation of amplitude $a_m (\ll \epsilon_m)$ and frequency f_m . The electrostatic potential on the surface of the marking electrode is given by

$$V_m = \epsilon_m + a_m \sin(2\pi f_m t) - F_m \quad (6.10)$$

where F_m is the work-function of the marking electrode. The DC component of this potential is given by

$$V_m^{dc} = \epsilon_m - F_m. \quad (6.11)$$

In this section we assume that the electrostatic potential (V) experienced by an electron passing through the central hole of the electrodes is equal to the electrostatic potential at the surface of the electrode and that the work function on the surface is uniform. Deviations from these assumptions limit the energy resolution of the analyzer and will be considered in the next section.

Of all the emitted electrons, only the ones with $T_e > -V_m$ pass through the marking electrode and rest get reflected back. As V_m has an oscillating component (see equation 6.10), the electron beam current after the marking electrode

consists of a DC current with a small sinusoidal oscillation whose amplitude is proportional to a_m and to the number of electrons with $T_e = -V_m^{dc}$.

Figure 6.4b shows a hypothetical, square-shaped uniform electron distribution as it propagates through the analyzer. At location 2, just beyond the marking electrode this distribution comprises of a DC current of electrons with $T_e > -V_m$ (shown in blue in figure 6.4b (2)) and a small oscillating component whose amplitude is proportional to a_m and to the number of electrons with $T_e = -V_m^{dc}$ (shown in red in figure 6.4b (2)). The longitudinal energy of these electrons at the emission surface is given by

$$W_{\parallel e} = -V_m^{dc} + V_e \quad (6.12)$$

These electrons producing the oscillation are said to be ‘marked’ with the frequency of the oscillation. The longitudinal energy of the ‘marked’ electrons can be changed by varying V_m^{dc} . It is possible to obtain the longitudinal energy distribution of the electrons at the cathode by measuring the amplitude of the oscillation in the beam current and varying the DC bias (ϵ_m) applied to the marking electrode to change V_m^{dc} .

6.4.3 Measuring the 2-D energy distribution

The accelerating electrodes and the vacuum chamber are grounded. Hence, after crossing the marking electrode the electron beam gets accelerated by $(V_c - V_e) = (-V_e - F_c)$ eV, where V_c is the electrostatic potential near the axis after the accelerating electrodes and F_c is the work function of the the vacuum chamber/accelerating electrodes ($V_c = -F_c$ since the accelerating electrodes and the vacuum chamber are grounded). The accelerated beam is guided by the

longitudinal magnetic field to the RFA section of the analyzer. The retarding electrode in the RFA region is biased to a DC voltage ϵ_r . The electrostatic potential at the surface of the retarding electrode is

$$V_r = \epsilon_r - F_r \quad (6.13)$$

where F_r is the work-function of the retarding electrode.

The strength of this magnetic field increases from B_i in the gun section to B_f at the retarding electrode in the RFA section. The magnetic field is constant in the retarding electrode. The adiabatic invariance along with the varying magnetic field in the drift region causes the transverse energy and the total longitudinal energy to couple and transform. Using equation 6.4, the transverse energy near the retarding electrode can be given by

$$W_{\perp r} = \frac{B_f}{B_i} W_{\perp e} = \alpha W_{\perp e} \quad (6.14)$$

Due to conservation of energy (equation 6.6), the total longitudinal energy near the retarding electrode is given by

$$T_r = T_e + W_{\perp e} - W_{\perp r} \quad (6.15)$$

Equations 6.14 and 6.15 can be written in matrix transformation form as follows

$$\begin{bmatrix} T_r \\ W_{\perp r} \end{bmatrix} = \begin{bmatrix} 1 & (1 - \alpha) \\ 0 & \alpha \end{bmatrix} \begin{bmatrix} T_e \\ W_{\perp e} \end{bmatrix} \quad (6.16)$$

The above equation relates the total longitudinal and the transverse energies at the cathode to those near the retarding electrode. From this equation the transverse energy at the cathode can be written in terms of T_r and T_e as

$$W_{\perp e} = \frac{T_r - T_e}{1 - \alpha} \quad (6.17)$$

The hypothetical distribution shown in figure 6.4b transforms according to equation 6.16 as it passes through the drift and reaches the retarding electrode. The transformed distribution at location (3) just before the retarding electrode is also shown in figure 6.4b.

Only electrons with $T_r > -V_r$ pass through the retarding electrode while rest are reflected back. Figure 6.4b shows the hypothetical distribution at location (4), right after the retarding electrode.

After the retarding electrode the beam goes through a pinhole which allows only electrons close to the axis to go through and stops the off axis electrons. As shown in the following section, this helps to improve the energy resolution of the analyzer. The electrons that pass through the pinhole are collected by the collector. The electron current from the collector acts as an input to a lock-in amplifier referenced to the frequency (f_m) of the marking electrode. This allows us to measure the amplitude of oscillating part (A) of the beam current while scanning through the voltages ϵ_m and ϵ_r applied to the marking and retarding electrodes respectively.

This amplitude, $A(\epsilon_m, \epsilon_r)$, is directly proportional to the number of electrons with $T_e = -V_m^{dc}$ and $T_r > -V_r$. By differentiating A w.r.t. ϵ_r we get

$$N_1(\epsilon_m, \epsilon_r) = k \frac{dA(\epsilon_m, \epsilon_r)}{d\epsilon_r} \quad (6.18)$$

as the number of electrons with $T_e = -V_m^{dc}$ and $T_r = -V_r$, where k is a proportionality constant. These electrons have a specific longitudinal energy and a specific transverse energy at the emission surface. These can be calculated from

equations 6.12 and 6.17 as

$$W_{\parallel e} = -(\epsilon_m - \epsilon_e) + (F_m - F_e) \quad (6.19)$$

$$W_{\perp e} = \frac{(\epsilon_m - \epsilon_r) - (F_m - F_r)}{1 - \alpha} \quad (6.20)$$

From equations 6.18,6.19 and 6.20 the number of electrons with a particular longitudinal energy and a particular transverse energy at the emission surface ($N(W_{\parallel e}, W_{\perp e})$) can be calculated. Thus one can obtain the complete 2-D energy distribution by scanning through ϵ_m and ϵ_r .

The work function related offset in the transverse direction, $\frac{F_m - F_r}{1 - \alpha}$, can be obtained from the work function independent measurement of the MTE as shown in the following section. The offset in the longitudinal energy $F_e - F_m$, is more difficult to obtain and requires the knowledge of the work functions of the emitter and the marking electrode. The longitudinal energy axis can also be pinned to the electron energy levels in the emitter if a band structure related feature (e.g. CBM or fermi level) is observed in the energy distribution[117]. In this paper we do not calculate the longitudinal energy offset. Instead the lowest energy obtained in the longitudinal energy distribution is assumed to be zero.

As a demonstration of such a measurement, a 2-D energy distribution of electrons emitted from a GaAs photoemitter[29] activated to negative electron affinity (NEA) using Cs and O₂ was measured. Electrons were excited using a laser of wavelength 780 nm. The work function of the NEA-GaAs photoemitter (F_e) is expected to be near 1.2-1.4 eV whereas the work function of the electrodes (F_m, F_r) is expected to be between 4-5 eV.

For this measurement, ϵ_e was set to -6.23 V, ϵ_m was scanned between -3.75 V and -3.45 V and ϵ_r was scanned between -3.3 V and -2.6 V. α was set to 4.2.

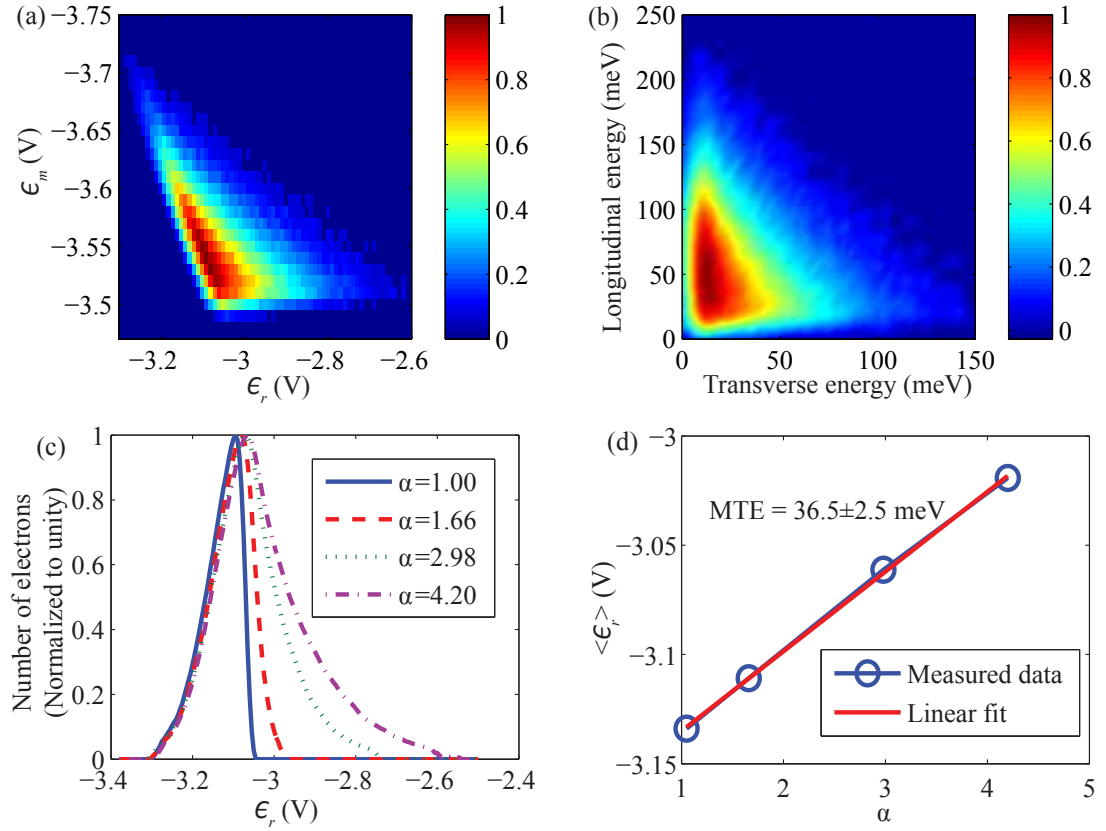


Figure 6.5: Measurements from a NEA-GaAs photoemitter under 780 nm illumination. (a) $N_1(\epsilon_m, \epsilon_r)$ (b) 2-D energy distribution, $N(W_{\parallel e}, W_{\perp e})$ (c) Longitudinal energy distributions at the retarding electrode for different α (d) The values of $\langle \epsilon_r \rangle$ for various values of α are obtained from figure 6.5c. MTE can be calculated as the negative slope of $\langle \epsilon_r \rangle$ vs. α .

Figure 6.5a shows the measured $N_1(\epsilon_m, \epsilon_r)$. This can be transformed to obtain the 2-D energy distribution, $N(W_{\parallel e}, W_{\perp e})$, shown in figure 6.5b.

In figure 6.5b, the zero on the transverse energy axis is set such that the MTE calculated from the 2-D distribution matches the one measured in the following section. This gives $F_m - F_r = -0.41$ eV. Assuming the minimum longitudinal energy to be 0 and $F_e = 1.4$ eV, we obtain $F_m = 4.56$ eV and $F_r = 5.1$ eV, which are within the expected range.

6.4.4 Measuring the MTE

The transverse energy of a single electron can be obtained as the change in the total longitudinal energy at the retarding electrode with α as

$$W_{\perp e} = -\frac{dT_r}{d\alpha} \quad (6.21)$$

Similarly, for an ensemble of electrons the MTE can be obtained as the change in the mean total longitudinal energy with α as

$$\text{MTE} = -\frac{d\langle T_r \rangle}{d\alpha} = -\frac{d\langle \epsilon_r \rangle}{d\alpha} \quad (6.22)$$

To measure the MTE using the above equation, the marking electrode is grounded and the longitudinal energy distribution at the retarding electrode is obtained for various values of α . The mean retarding voltage is then calculated as $\langle \epsilon_r \rangle = \frac{\int \epsilon_r N(\epsilon_r) d\epsilon_r}{\int N(\epsilon_r) d\epsilon_r}$ for all the values of α . Finally, the negative slope of $\langle \epsilon_r \rangle$ vs. α gives the MTE.

Figure 6.5(c) shows the longitudinal energy distributions at the retarding electrode at four values of α for the NEA-GaAs photoemitter under 780 nm illumination. Figure 6.5d shows the plot of $\langle \epsilon_r \rangle$ vs. α which gives a MTE of 36.5 meV. This value matches the MTE value obtained from other techniques[29, 17] within the experimental uncertainty.

Such a measurement of the MTE does not require the knowledge of the work functions and can be used obtain the value of $F_m - F_r$ and and explicitly determine the zero of the transverse energy axis in the 2-D distribution.

6.5 Optimizing the signal to noise ratio and the energy resolution

6.5.1 The signal to noise ratio

Several contributions must be considered when maximizing the signal to noise ratio of the measurements.

The pk-pk noise in the current measured by the lock-in amplifier is limited to 100 fA by the electronics and the cabling.

The signal detected by the lock-in amplifier is proportional to the amplitude of the ac oscillation (a_m) at the marking electrode and the total beam current collected by the collector when no electrons are blocked by any of the electrodes. As shown in the next section, the amplitude of the ac oscillation at the marking electrode should be kept to a minimum to achieve best energy resolution.

Hence, in order to maximize the signal to noise ratio without compromising the resolution, the beam current at the collector should be maximized. The beam current is limited by the maximum allowed current density to keep the space charge and intra-beam scattering effects negligible and by the size of the pinhole that blocks off axis electrons to increase the resolution.

The effects of space charge and intra-beam scattering which are already mitigated due to the strong longitudinal magnetic field can be ignored if the current densities are kept below $2 \mu\text{A}/\text{cm}^2$ as shown by Hoppe *et al*[117]. The current densities used in the measurements presented in this paper are also kept below this value. It was verified that the results obtained were invariant with the cur-

rent density ensuring that the space charge and intra-beam scattering effects are indeed negligible.

The signal to noise ratio cannot be increased by increasing the current density due to space charge and intra-beam scattering limitations. However, it can be increased by increasing the diameter of the pinhole used to block off axis electrons. The diameter of the pinhole used here is $200 \mu\text{m}$ which is 8 times larger than the pinhole used by Hoppe *et al.*[117] making the signal to noise ratio more than 50 times larger. As shown in the following section, increasing the pinhole size does not adversely affect the energy resolution if the electrodes are designed appropriately.

6.5.2 The energy resolution

The energy resolution is the uncertainty in the measurement of the longitudinal and transverse energies. The energy resolution can be measured by marking a particular electron energy at the marking electrode and measuring the width of this mark at the retarding electrode after setting $\alpha = 1$. When $\alpha = 1$ the total longitudinal energy distributions at the marking and retarding electrodes are identical. As ϵ_r is scanned the current measured by the lock-in amplifier is initially constant and shows a sharp drop to 0 when $V_m^{dc} = V_r$. The derivative of the lock-in amplifier output is zero with a sharp peak at $V_m^{dc} = V_r$. This peak can be well fitted by a Gaussian whose standard deviation is taken to be the resolution of the energy analyzer. The measured resolution of the analyzer described here is compared to the analyzer developed by Hoppe *et al.*[117] in figure 6.6.

As shown in Appendix A it is possible to estimate the energy resolution and

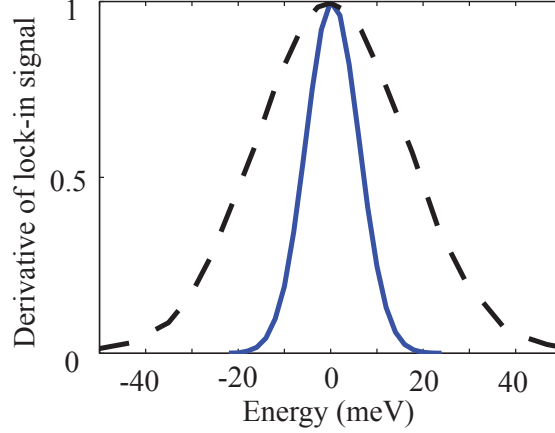


Figure 6.6: Peak defining the analyzer resolution. Blue solid curve ($\sigma = 5.7$ meV) is measured for the analyzer described in this paper. The black dashed curve ($\sigma = 17$ meV) is the curve obtained by Hoppe *et al*[117].

identify several factors that contribute to it. Let $z = 0$ be the position of the electron emitter, $z = z_m$ be the location at which the electrons are marked in the first marking electrode and $z = z_r$ be the position where the electrons are stopped in the retarding electrode. The energy resolution is then given by

$$\Delta W = \left[\frac{a_m^2}{2} + 2(\Delta V)^2 + (\Delta F)^2 + (\Delta S)^2 \right]^{\frac{1}{2}},$$

$$\Delta S = \frac{r_p^2}{4} [|\kappa_1(z_m)| + |\kappa_1(z_r)|] \quad (6.23)$$

where a_m is the amplitude of the oscillation applied to the marking electrode and is limited by the smallest signal to noise ratio required by the lock-in amplifier. ΔV is the rms noise on the dc voltages applied to the emitter, marking electrode and the retarding electrode and with appropriate shielding can be reduced below 0.5 mV. ΔS is the contribution due to the non-zero size of the electron beam about the axis and ΔF is the spatial variation in the potential experienced by the electrons due to the work function variation over the electrode surface. r_p is the radius of the pinhole after the retarding electrode and $\kappa_1(z) = -\frac{\partial^2 V(z)}{\partial z^2}$, where $V(z)$

is the electrostatic potential on the axis of the analyzer.

For the analyzer described in this paper, a_m is set to 5 mV and ΔV is small enough to be negligible. The contributions from ΔS and ΔF can be reduced by the appropriate design of the electrodes.

Reducing ΔS

ΔS can be reduced by reducing the size of the pinhole, r_p . In the analyzer developed by Hoppe *et al*[117], $\kappa_1(z_r) \approx 2$ V/mm². This limits r_p to approximately 10 μm in order to make $\Delta S < 0.1$ meV and negligible.

However, ΔS can also be reduced by reducing both $\kappa_1(z_m)$ and $\kappa_1(z_r)$ thus allowing r_p to be larger. $\kappa_1(z_m)$ and $\kappa_1(z_r)$ can be reduced by increasing the thickness and reducing the diameter of the central hole of the marking and retarding electrodes. The thickness and the diameter of the central hole are limited only by the ability to produce a constant magnetic field in the gun and RFA regions and the ability to coat the surface of the electrodes uniformly to reduce work function fluctuations. The design of the gun and RFA used in the analyzer described in this paper is shown in figures 6.3a and 6.3b, respectively. The on axis electrostatic potential $V(z)$ and $\kappa_1(z)$ for this design are shown in figures 6.3c and 6.3d. For this design both $\kappa_1(z_m)$ and $\kappa_1(z_r)$ are less than 0.01 V/mm² allowing the pinhole size to be larger than 100 μm and still keeping ΔS negligible. Reducing $\kappa_1(z_m)$ and $\kappa_1(z_r)$ instead of r_p to reduce ΔS allows for a higher signal to noise ratio.

Reducing ΔF

ΔF and a_m are the factors that limit the energy resolution. It is difficult to estimate ΔF ; however, steps can be taken to reduce it. Electrodes can be gold plated or coated with a colloidal graphite spray to make the work function uniform and minimize its variation due to surface adsorbates. The design of the electrodes should allow uniform coating of the central hole with ease. In general a larger central hole help to achieve this. Electrodes can be cleaned using a high power laser[117] or by bombarding them with electrons accelerated to ≈ 10 eV. Despite these steps, reducing ΔF largely remains a process of trial and error.

Initially, all the electrodes used in the analyzer described here were gold plated. The retarding electrode had a central hole diameter of 1 mm and a thickness of 5 mm. However, the measured energy resolution was larger than 100 meV. This was most likely due to non-uniform plating of the central hole in the retarding electrode. To solve this issue, the electrodes were coated with a colloidal graphite spray, typically used to coat hemispherical analyzers in order to obtain uniform work functions. The retarding electrode was also redesigned to have a central hole diameter of 3 mm and a thickness of 9 mm. It was also built as a disk that could be split into two halves allowing near normal line of sight to all the surfaces inside the central hole of the electrode ensuring uniform coating. Figure 6.3b shows the redesigned retarding electrode. With these changes the measured energy resolution reduced to less than 6 meV as shown in figure 6.6.

6.6 Conclusion

We have detailed the design and operation of a 2-D analyzer capable of measuring the transverse and longitudinal electron energy distributions simultaneously. Its insensitivity to stray magnetic fields and work function differences between the emitter and the electrodes along with its compact size makes it an excellent tool to study the physics of photoemission.

The design of such an analyzer has been optimized and the various factors limiting the energy resolution and the signal to noise ratio have been identified. The new design demonstrates an energy resolution better than 6 meV along with a 50 fold increase in the signal to noise ratio compared to its previous realization.

This work has been funded by the Department of Energy under Grant No. DESC0003965. The authors would like to especially acknowledge the efforts of Valeri Medjidzade (deceased) for the mechanical design of the analyzer. The authors would also like to thank Dr. Bruce Dunham, Dr. Yulin Li, Dr. Xianghong Liu and Karl Smolenski for review of the drawings and mechanical design.

CHAPTER 7

CONCLUSION

Understanding the process of photoemission is critical in order to design photocathode materials that optimize the photoemission properties like quantum efficiency, mean transverse energy and response time. Improvements in photocathode materials will result in proportional improvements in the performance of large electron accelerators used as electron colliders, hadron beam coolers[5] and 4th generation light sources like Free Electron Lasers[4] and Energy Recovery Linacs[3] and also enable new applications like ultra-fast electron diffraction[8] of proteins and intense gamma ray production using inverse compton scattering[6].

GaAs and other III-V semiconductors activated to negative electron affinity using Cs and O₂ or NF₃ are excellent photocathodes[23, 24] due to their high QE in visible light, small MTE and ability to produce polarized electrons. Despite being used for decades as image intensifiers and source of polarized electrons, the physics of photoemission from these cathodes has not been well understood.

The photoemission from such cathodes can be best described within the framework of Spicer's three-step photoemission model of electron excitation, transport to surface and emission into vacuum[29]. The excitation of electrons from the valance band to conduction band and the transport to the surface can be modeled accurately using the 3 valley model for the band structure of GaAs and Monte Carlo based semiclassical electron transport simulations. These simulations include effects of various electron scattering mechanisms like acoustic and optical phonon scattering, polar optical and piezoelectric phonon scattering, charge impurity scattering and electron-hole binary scattering. The elec-

trons that reach the surface get emitted into vacuum if permitted by the conservation of energy and transverse momentum. Such detail modeling of photoemission accurately predicts the QE and response time from activated GaAs cathodes. However, the predicted MTE is much lower than the measured value. This discrepancy can be solved by including an elastic surface scattering which redistributes the emission angle of electrons uniformly in the polar angle. Such modeling of photoemission from GaAs cathodes reproduces the QE and MTE accurately for wavelengths of incident light ranging from infrared to green.

This photoemission simulation is extended to include other III-V semiconductors and layered structures of III-V semiconductors. Using this simulation, it is possible to design layered structures of III-V semiconductors to optimize photoemission properties[17]. As a demonstration, a layered structure consisting of 100 nm undoped GaAs over *p*-doped GaAs bulk was designed to exhibit a smaller MTE compared to the completely *p*-doped cathode. This structure was grown using molecular beam epitaxy and the measured QE and MTE for wavelengths ranging from infrared to green agreed with the simulations.

In order to address the issue of surface scattering and non-conservation of transverse momentum, the nature and structure of the Cs monolayer on GaAs was investigated via *ab-initio* calculations. Density functional theory calculations suggested that work function variations can exist on the GaAs/Cs surface a scale greater than several nm, not only due to the surface reconstruction of GaAs, but also due to the amorphous nature of the Cs layer[31]. Such work function variations can cause the non-conservation of transverse momentum and limit the MTE causing the discrepancy between theory and experimental values[32].

This thesis also presents a design and practical issues in developing a 2-D energy analyzer to measure the longitudinal and transverse energy distributions of low (< 1 eV) energy electrons simultaneously. This analyzer utilizes the motion of electrons in a strong magnetic field and the principle of adiabatic invariance to obtain an energy resolution of better than 6 meV rms[21]. This analyzer is an important tool to study the physics of photoemission from various photocathodes.

Developing better photocathodes remains a challenge from both physics and materials engineering point of view. The physics of low energy photoemission needs to be understood. The reason for the non-conservation of transverse momentum remains to be poorly understood. Developing complete quantum mechanical photoemission models that take into account surface non-uniformities, scattering with phonons and plasmons near the surface during photoemission and the electronic structure at the surface is essential to establish the factors that limit the MTE. Developing reliable electron energy distribution diagnostics for low energy electrons is necessary in order to obtain consistent experimental data and validate the various photoemission and surface scattering models proposed. The understanding of physics of photoemission will enable engineering of novel materials that have properties suitable for minimizing MTE along with satisfying the other requirements of QE, response time and longevity.

APPENDIX A

CALCULATION OF ENERGY RESOLUTION

The energy resolution is given by the uncertainty in the measurement of $W_{\parallel e}$ and $W_{\perp e}$. It is possible to estimate this uncertainty by expanding the fields near the axis using the paraxial approximation. The near axis region is free of sources and the fields are static. $O(r^2)$ paraxial expansion of the fields gives the radial magnetic field, $B_r(r, z)$, as

$$B_r(r, z) = -\frac{r}{2} \frac{\partial B(0, z)}{\partial z} \dots, \quad (\text{A.1})$$

the axial magnetic field, $B_z(r, z)$, as

$$B_z(r, z) = B(0, z) - \frac{r^2}{4} \frac{\partial^2 B(0, z)}{\partial z^2} \dots, \quad (\text{A.2})$$

the total magnetic field, $B(r, z)$, as

$$B(r, z) = B(0, z) \times \left[1 + \frac{r^2}{8} \frac{\left(\frac{\partial B(0, z)}{\partial z}\right)^2 - 2B(0, z) \frac{\partial^2 B(0, z)}{\partial z^2}}{B(0, z)^2} \dots \right] \quad (\text{A.3})$$

and the electrostatic potential, $V(r, z)$, as

$$V(r, z) = V(0, z) - \frac{r^2}{4} \frac{\partial^2 V(0, z)}{\partial z^2} + \dots \quad (\text{A.4})$$

Let $z = 0$ be the position of the electron emitter, $z = z_m$ be the location at which the electrons are marked in the first marking electrode and $z = z_r$ be the position where the electrons are stopped in the retarding electrode. Consider an electron such that its guiding center is at a distance of $r(z)$ from the z axis. As the guiding center follows the lines of magnetic field, the equation of the guiding center is given by

$$\frac{dr}{dz} = \frac{B_r(r, z)}{B_z(r, z)} \quad (\text{A.5})$$

which on solving using the paraxial approximation to the first order in r gives us

$$r(z) = r(0) \sqrt{\frac{B_z(0,0)}{B_z(0,z)}} \quad (\text{A.6})$$

Combining equation A.6 with the adiabatic invariance and the conservation of energy and utilizing the paraxial approximation, we get the longitudinal energy of the electron as a function of the longitudinal coordinate z as

$$W_{\parallel}(r(z), z) = W_{\perp}(r(0), 0) [\xi(z)] + W_{\parallel}(r(0), 0) + V(0, 0) - V(0, z) - \frac{r(0)^2}{4} [\kappa(z)], \quad (\text{A.7})$$

where $\xi(z)$ is the magnetic precision parameter and $\kappa(z)$ is the electric precision parameter.

The magnetic precision parameter is given by

$$\xi(z) = 1 - \alpha(z) - \frac{r(0)^2}{8} \frac{\left(\frac{\partial B(0,z)}{\partial z}\right)^2 - 2B(0,z) \frac{\partial^2 B(0,z)}{\partial z^2}}{B(0,z)^2}, \quad (\text{A.8})$$

where $\alpha(z) = \frac{B_z(0,z)}{B_z(0,0)}$. However, the solenoid coils are designed such that $\frac{\partial B(0,z)}{\partial z}$ and $\frac{\partial^2 B(0,z)}{\partial z^2}$ are negligible at $z = z_m$ and $z = z_r$ and $\alpha(z_m) = 1$. Thus $\xi(z_m) = 0$ and $\xi(z_r) = 1 - \alpha(z_r)$

The electric field precision parameter is given by

$$\begin{aligned} \kappa(z) &= \frac{\partial^2 V(0,z)}{\partial z^2} \Big|_{z=0} - \frac{1}{\alpha(z)} \frac{\partial^2 V(0,z)}{\partial z^2} \\ &= -\frac{1}{\alpha(z)} \frac{\partial^2 V(0,z)}{\partial z^2} \end{aligned} \quad (\text{A.9})$$

since $\frac{\partial^2 V(0,z)}{\partial z^2} \Big|_{z=0} = 0$ if the surface potential of the emitter is uniform.

From equations A.7, A.8 and A.9 we can obtain the longitudinal energy at z_m and z_r as

$$W_{\parallel}(r(z_m), z_m) = W_{\parallel}(r(0), 0) + V(0, 0) - V(0, z_m) - \frac{r(0)^2}{4} [\kappa(z_m)], \quad (\text{A.10})$$

and

$$W_{\parallel}(r(z_r), z_r) = W_{\perp}(r(0), 0) [1 - \alpha(z_r)] + W_{\parallel}(r(0), 0) + V(0, 0) - V(0, z_r) - \frac{r(0)^2}{4} [\kappa(z_r)], \quad (\text{A.11})$$

The electrons which are both marked by the marking electrode and cut by the retarding electrode have $W_{\parallel}(r(z_m), z_m) = W_{\parallel}(r(z_r), z_r) = 0$ and, at the emitter, have a particular longitudinal energy given by

$$W_{\parallel e} = -V(0, 0) + V(0, z_m) + \frac{r(0)^2}{4} \kappa(z_m) \quad (\text{A.12})$$

and a particular transverse energy given by

$$W_{\perp e} = \frac{V(0, z_m) - V(0, z_r) + \frac{r(0)^2}{4} [\kappa(z_m) - \kappa(z_r)]}{\alpha(z_r) - 1} \quad (\text{A.13})$$

The above two equations are the analogs of equations 6.19 and 6.20 with the potential variation between the electrode surface and the axis taken into account.

Thus the rms uncertainty in the measurement of the longitudinal energy, $W_{\parallel e}$, is

$$\Delta W_{\parallel e} = \left[\frac{a_m^2}{2} + 2(\Delta V)^2 + (\Delta F)^2 + \left(\frac{r_p^2}{4} \kappa(z_m) \right)^2 \right]^{\frac{1}{2}} \quad (\text{A.14})$$

and the rms uncertainty in the measurement of the transverse energy, $W_{\perp e}$, is

$$\Delta W_{\perp e} = \frac{1}{\alpha(z_r) - 1} \left[\frac{a_m^2}{2} + 2(\Delta V)^2 + (\Delta F)^2 + \left(\frac{r_p^2}{4} [\kappa(z_m) - \kappa(z_r)] \right)^2 \right]^{\frac{1}{2}} \quad (\text{A.15})$$

where a_m is the amplitude of the oscillation applied to the marking electrode, ΔV is the rms noise on the dc voltages applied to the emitter, marking electrode and the retarding electrode, ΔF is the variation in the electrostatic potential due to the work function variation on the electrodes, r_p is the radius of the pinhole after the retarding electrode.

It is difficult to directly measure $\Delta W_{\parallel e}$ and $\Delta W_{\perp e}$ due to the lack of a sharp feature in the longitudinal and transverse energy distributions. However the energy resolution can be estimated by setting $\alpha(z_r) = 1$, marking the electrons of a particular longitudinal energy at the marking electrode and measuring the width of the marked electrons at the retarding electrode. When $\alpha(z_r) = 1$ the energy distribution at the retarding electrode is the same as that at the marking electrode. In such a case, according to equations A.10 and A.11 the width of the marking measured at the retarding electrode is given by

$$\Delta W = \left[\frac{a_m^2}{2} + 2(\Delta V)^2 + (\Delta F)^2 + \left(\frac{r_p^2}{4} [|\kappa(z_m)| + |\kappa(z_r)|] \right)^2 \right]^{\frac{1}{2}} \quad (\text{A.16})$$

This width can be easily measured and it represents the energy resolution of the analyzer.

APPENDIX B

2-D ENERGY DISTRIBUTIONS FROM QUANTUM WELL AND SUPER-LATTICE STRUCTURES

In this appendix we report the spectral response and the energy distribution measurements of GaAs/AlGaAs quantum well (QW) and super-lattice (SL) structures grown using molecular beam epitaxy (MBE). These structures were designed such that only electrons with a very narrow range (<20 meV) of longitudinal energies could be emitted. The 2-D distributions measured from these structures using the energy analyzer described in chapter 6 would give better insights into the surface scattering mechanism. However, the results obtained are marred with uncertainties in the exact dimensions of structures grown and in the activation process, making the results inconclusive.

B.1 Physical and electronic structures

B.1.1 Quantum well structure

The QW structure consisted of a GaAs quantum well sandwiched between two $\text{Al}_{0.3}\text{Ga}_{0.7}\text{As}$ barriers. Figure B.1a shows the details of this structure. The entire structure was p -doped to 10^{19} cm^{-3} . The conduction band profile was calculated using a schrodinger-poisson solver[1]. The conduction band at the surface was pinned 0.5 eV below the bulk conduction band due to the fermi level pinning. The barrier due to the Cs and the profile in vacuum was not calculated using the schrodinger poisson solver, but was used from previous literature[29]. The structure of the conduction band and vacuum level is shown in figure B.1b.

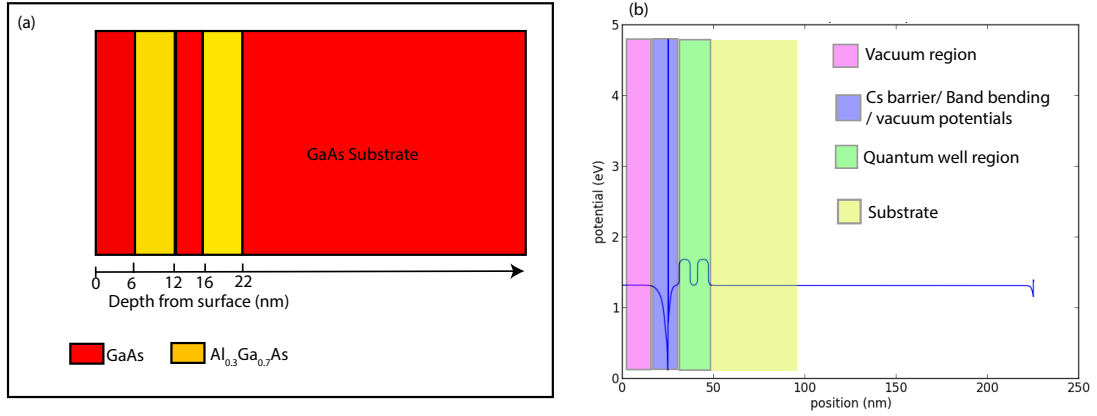


Figure B.1: (a) Structure of the QW sample. (b) Profile of the conduction band for the QW structure as calculated from the schrodinger-poisson solver[1] along with the Cs barrier.

Transmission probability of electrons through this potential well barrier was calculated by approximating the band profile using small rectangles of 0.5 \AA in length and using the propagation matrix approach[59]. The calculated transmission probability as a function of electron energies electron energies is shown in figure B.2. The different curves show calculations by varying the thickness of the quantum well layers by $\pm 3 \text{ \AA}$. This is done to take into account the uncertainty in the layer thicknesses inherent to the MBE growth procedure. We see that for the QW structure the resonant tunneling energy is around 1.46-1.48 eV above the bulk valence band maxima (VBM) with the width of the resonance peak smaller than 1 meV. The exact position of this peak varies between 1.46 eV to 1.48 eV for the $\pm 3 \text{ \AA}$ uncertainty in the thickness of the layers. Thus with this uncertainty we can expect the effective width of the peak to be $\sim 20 \text{ meV}$. Beyond 1.65 eV, the electron energy becomes comparable to that of the barrier and we have a continuous spectrum of transmitted electron energies. One must keep in mind that this is a 1-D calculation and the electron energy corresponds

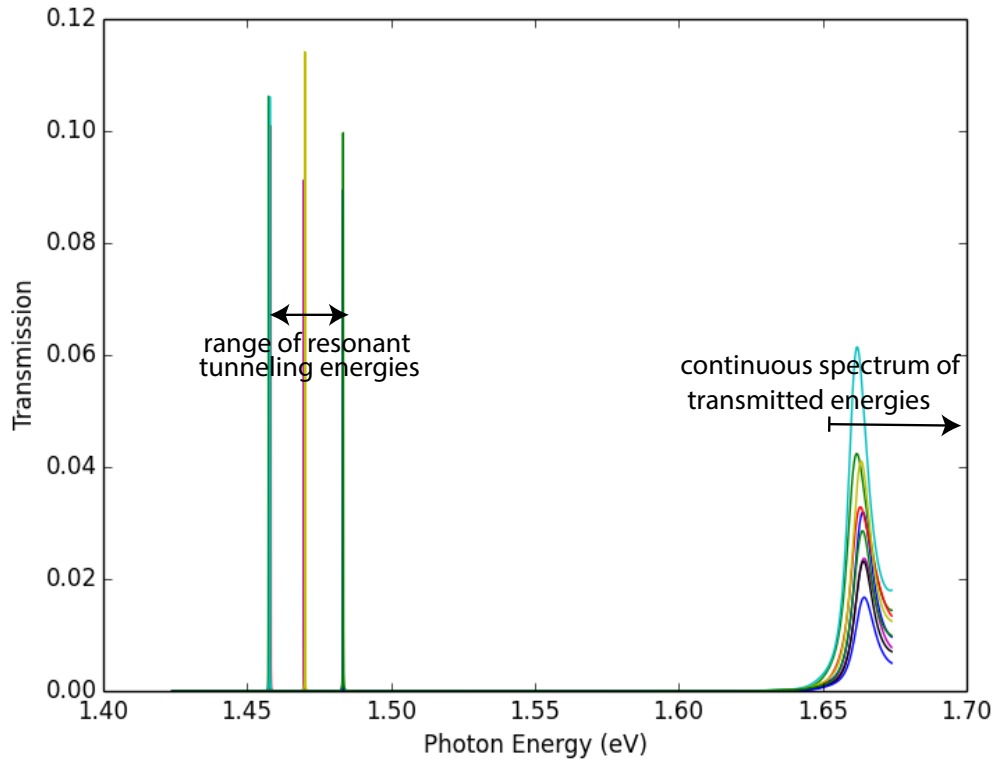


Figure B.2: Transmission energies for the QW shown in figure B.1. The different curves are obtained by changing the thickness of the various layers in the QW by $\pm 3 \text{ \AA}$. This uncertainty can cause a spread of about 20 meV in the resonant tunneling energy.

to only the longitudinal energy. The transverse energy remains unrestricted.

B.1.2 Super-lattice structure

The SL structure consisted of alternating layers of GaAs of thickness 4 nm and $\text{Al}_{0.3}\text{Ga}_{0.7}\text{As}$ of thickness 6 nm. The overall thickness of the super-lattice was greater than $1 \mu\text{m}$. The entire structure was p -doped to 10^{19} cm^{-3} . The structure is shown in figure B.3a.

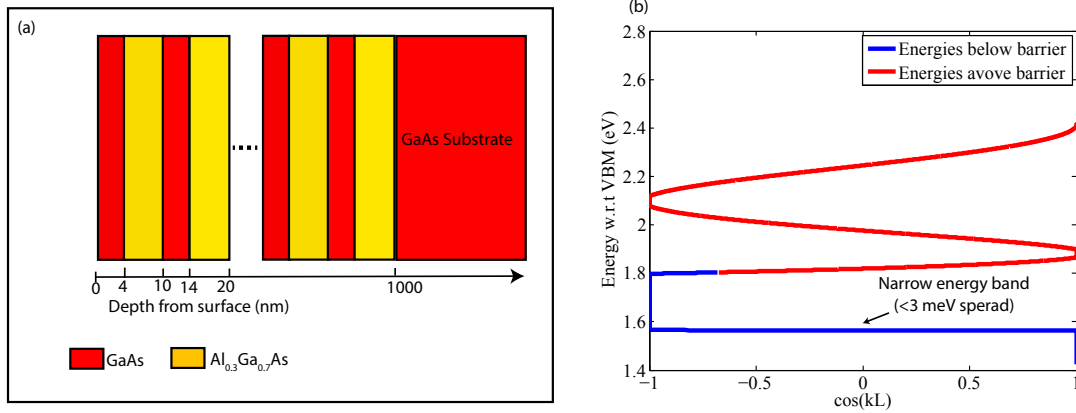


Figure B.3: (a) Structure of the SL sample. (b) Band structure for the SL structure. k is the bloch wave vector and L is the lattice spacing of the SL structure

The conduction band minimum in $\text{Al}_{0.3}\text{Ga}_{0.7}\text{As}$ is 0.38 eV higher as compared to GaAs. This form a periodic potential lattice of barriers for the electrons in the conduction band. The band structure for such a lattice was calculated using the propagation matrix approach[59]. The effective masses and CBM energies for GaAs and $\text{Al}_{0.3}\text{Ga}_{0.7}\text{As}$ were taken from reference [40]. The calculated band structure is shown in figure B.3b.

The lower most band has a very narrow band with an energy spread of 3 meV and is located near 1.55 eV from the VBM. The next band is above 1.8 eV and has a much higher spread. The electrons excited in the narrow band will have a very narrow spread in the longitudinal energy. Due to the 1-D nature of the calculation, the transverse energy is unrestricted. As in the case of the QW structure, the uncertainty in the thickness of the layers the spread of the narrowest band increases to ~ 20 meV.

B.2 Activation and spectral response

Both the samples were activated to negative electron affinity using Cs and O₂. The photocurrent in the green was monitored during activation. The samples were first exposed to a flux of Cs till the photocurrent peaked. Then they were exposed to both Cs and O₂ simultaneously to obtain a further rise in photocurrent.

After activation the spectral response was measured using a Hg lamp with a monochromator. Figure B.4 shows the spectral response of the QW and SL structures along with the regular *p*-doped GaAs for reference. We see that the QE of the QW and SL structure is much smaller compared to the bulk GaAs sample. This is expected because most of the electrons are blocked by the barriers in the quantum well and super-lattice structures. We also observe several features in the spectral response of the QW and SL structures that correspond to features in their respective band structures.

In B.4, A and B indicate the kinks in the spectral response of the QW structure corresponding to the resonant tunneling energy of 1.46-1.48 eV and the barrier height of 1.65 eV. In the spectral response of the SL structure C indicates the peak due to the narrow band at 1.55 eV and D indicates the small kink due to the beginning of the second band at 1.88 eV.

These features in the spectral response indicate the existence of the expected transmission energies and bands in the QW and SL structures grown. However, they do not indicate the width of the transmission energies or the bands.

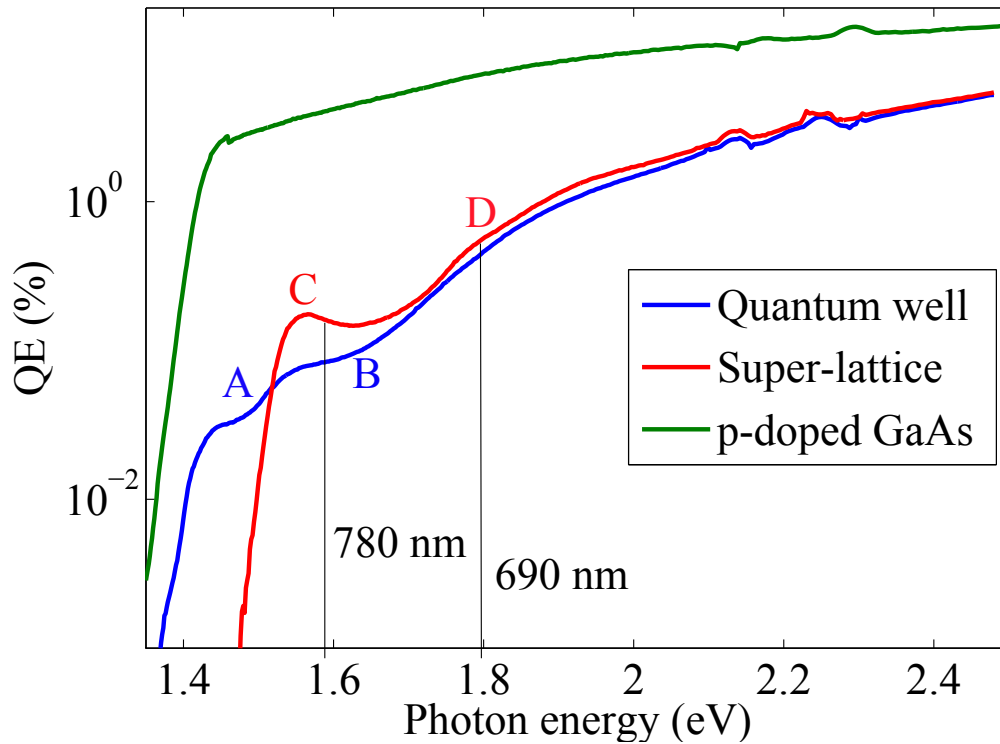


Figure B.4: Spectral response of the quantum well (QW), super-lattice (SL) and *p*-doped GaAs samples. A, B, C and D indicated the features in the spectral response corresponding to the various bands and transmission energies in the band structures. The two wavelengths (780 nm and 690 nm) used to measure the energy distribution are also indicated. The kinks in the spectral response curves in the 2.1-2.3 eV range are an artifact of the measurement caused by the intense emission lines of the Hg lamp.

B.3 2-D energy distributions

The longitudinal and transverse energy distributions were measured for the activated QW and SL structures using the 2-D energy analyzer[21]. The distributions were measured using two wavelengths: 780 nm (photon energy of 1.59 eV) and 690 nm (photon energy of 1.8 eV). These wavelengths are shown in figure

B.4. The measured 2-D energy distributions are shown in figure B.5.

The zero on the transverse energy axis has been fixed with an accuracy of 10 meV using the procedure described in [21]. However the longitudinal energy axis is not fixed and depends on the work functions of the analyzer electrodes and the sample. In figure B.5 the zero of the longitudinal is assumed to be the same as figure 6.5b which shows a 2-D energy distribution for an activated GaAs sample. Thus in figure B.5, zero longitudinal energy implies the longitudinal energy equal to the lowest longitudinal energy of electrons emitted from activated *p*-GaAs.

Figure B.5a and B.5b show the energy distributions for the QW structure using lasers of wavelengths 780 nm and 690 nm respectively. We see that the lowest longitudinal energy of emitted electrons is 0.12 eV higher than that of bulk GaAs. This can be either because the vacuum level of the QW sample was 0.12 eV higher than the activated *p*-GaAs sample or because no electrons are transmitted through the resonance energy of the QW. It is not possible to rule out either with the data we have.

Figure B.5c and B.5d show the energy distributions for the SL structure using lasers of wavelengths 780 nm and 690 nm respectively. We see that the lowest longitudinal energy measured is the same as that measured from activated *p*-GaAs. This tells us that the activation procedure lowered the vacuum level in the SL sample and the *p*-GaAs sample equally. As shown in figure 6.5b the maximum intensity is at 50 meV in longitudinal energy and 20 meV in transverse energy for the *p*-GaAs. However, for the SL sample the maximum intensity region is shifted higher in longitudinal energy to 120 meV. This is because the lowermost energy conduction band in the SL structure is at a higher energy of

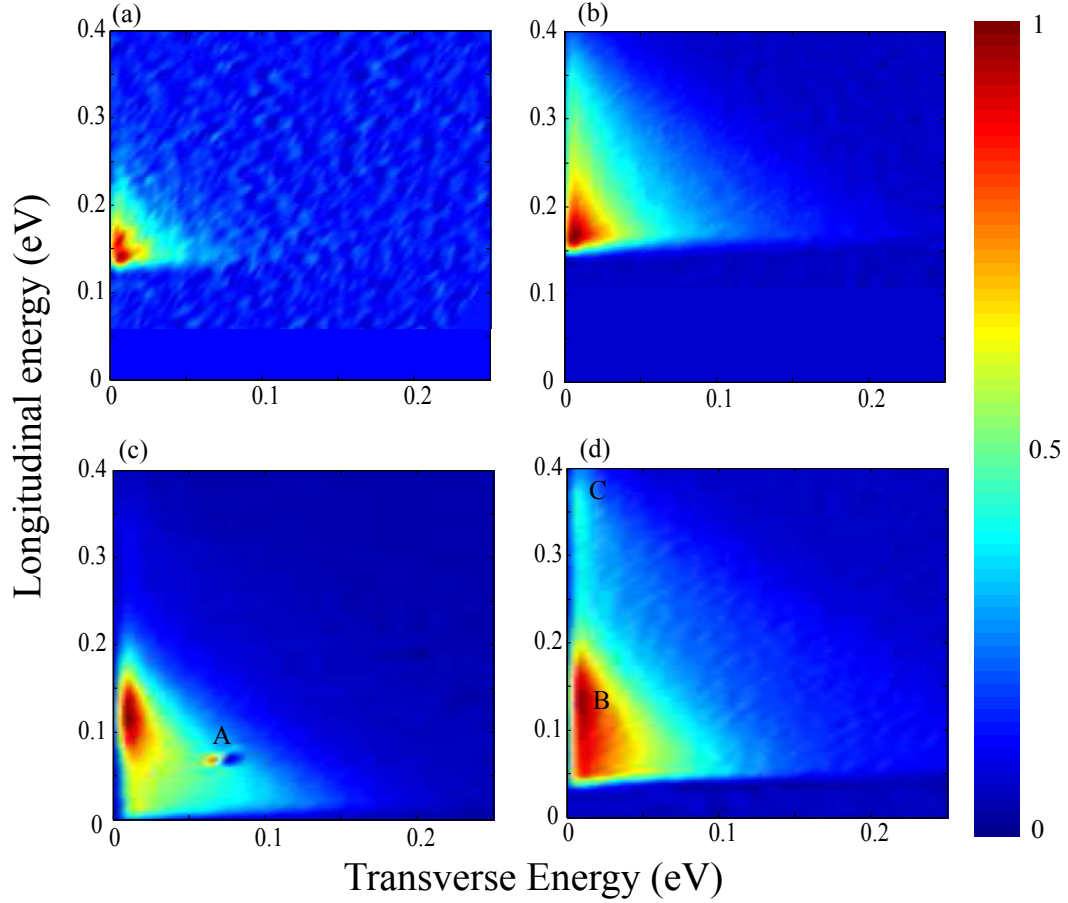


Figure B.5: 2-D energy distributions of (a) QW sample with 780 nm laser, (b) QW sample with 690 nm laser, (c) SL sample with 780 nm laser and (d) SL sample with 690 nm laser. The feature marked by (A) is a glitch in data taking and should be ignored.

1.55 eV as compared to 1.42 eV in *p*-GaAs.

The energy distribution obtained from the SL sample using the 690 nm laser shows two interesting features - 1.) the maximum intensity peak near longitudinal energy of 0.12 eV (indicated by B in figure B.5d) and 2.) a very faint peak in the intensity near longitudinal energy of 0.35 eV (indicated by C in figure B.5d). The difference in the longitudinal energies of these peaks is 0.23 eV which is

equal to the difference between the first and second conduction band of the SL sample. This suggests that the second peak is due to the electrons emitted from the second conduction band of the SL sample.

Even though the longitudinal energy width of the lowermost conduction band in the SL structure is 3 meV, the longitudinal energy spread measured is greater than 100 meV. This can either be due to the surface scattering or due to the imperfections in the growth of the SL structure. SL structures grown using MBE are expected to be accurate with only an atomic monolayer uncertainty of $\pm 3 \text{ \AA}$. In section B1 we estimate this uncertainty could lead to a longitudinal energy spread of $\sim 20 \text{ meV}$. However, there is no way to verify the perfection of the SL structure. Very small imperfections of less than 3 atomic monolayers coupled with non uniformities in the transverse directions on a similar scale can easily cause the spread in longitudinal energies to be of the order of 100 meV. Thus from the available data it is not possible to say with certainty that the spread in longitudinal energy is only due to surface scattering during emission. Independent verification of the band structure of the SL structure is required.

B.4 Conclusion

The QW and SL structures grown were activated and their energy distributions were measured.

In the case of the QW structure, no emission at the resonant energy was observed in the energy distribution. This was either due to non-ideal activation or due to the electrons not being able to tunnel through the barrier because of the extremely narrow resonant energy.

In the case of the SL structure even though emission was observed from the narrow conduction band, it is impossible to attribute the observed energy spread to either surface scattering or imperfections in the SL structure. Owing to the difficulties in interpreting this experimental data no concrete conclusion can be made from this work. This appendix, nonetheless, contains essential experimental details in hopes of guiding the thinking process of the follow-up work.

BIBLIOGRAPHY

- [1] M. C. Foisy. *A physical model for the bias dependence of the modulation-doped field-effect transistor's high-frequency performance*. PhD thesis, Cornell University, 1990.
- [2] Triveni Rao and David H. Dowell. *An Engineering Guide to Photoinjectors*. CreateSpace Independent Publishing Platform, 2013.
- [3] S. M. Gruner, D. Bilderback, I. Bazarov, K. Finkelstein, G. Krafft, L. Merminga, H. Padamsee, Q. Shen, C. Sinclair, and M. Tigner. *Rev. Sci. Instr.*, 73:1402, 2002.
- [4] W. Ackermann *et al.* *Nat. Photonics*, 1:336, 2007.
- [5] Ilan Ben-Zvi *et al.* *Nucl. Instr. Meth. A*, 532:177, 2004.
- [6] S. Boucher, P. Frigola, A. Murokh, M. Ruelas, I. Jovanovic, J.B. Rosenzweig, and G. Travish. *Nucl. Instr. Meth. A*, 608:S54, 2009.
- [7] I. V. Bazarov, B. M. Dunham, and C. K. Sinclair. *Phys. Rev. Lett.*, 102:104801, 2009.
- [8] P. Musumeci, J. T. Moody, C. M. Scoby, M. S. Gutierrez, H. A. Bender, and N. S. Wilcox. *Rev. Sci. Instr.*, 81:013306, 2010.
- [9] T. van Oudheusden, E. F. de Jong, S. B. van der Geer, W. P. E. M. Op t Root, O. J. Luiten, and B. J. Siwick. *J. Appl. Phys.*, 102:093501, 2007.
- [10] J. M. Maxson, I. V. Bazarov, W. Wan, H. A. Padmore, and C. E. Coleman-Smith. *New J. Phys.*, 15:103024, 2013.
- [11] D. H. Dowell, I. Bazarov, B. Dunham, K. Harkay, C. Hernandez-Garcia, R. Legg, H. Padmore, T. Rao, J. Smedley, and W. Wan. *Nucl. Instrum. Methods Phys. Res. A*, 622:685, 2010.
- [12] B. Dunham *et al.* *Appl. Phys. Lett.*, 102:034105, 2013.
- [13] I. V. Bazarov, B. M. Dunham, Y. Li, X. Liu, D. G. Ouzounov, C. K. Sinclair, F. Hannon, and T. Miyajima. *J. Appl. Phys.*, 103:054901, 2008.

- [14] A. Polyakov, C. Senft, K. F. Thompson, J. Feng, S. Cabrini, P. J. Schuck, H. A. Padmore, S. J. Peppernick, and W. P. Hess. *Phys. Rev. Lett.*, 110:076802, 2013.
- [15] K. Nemeth, K. C. Harkay, M. van Veenendaal, L. Spentzouris, M. White, K. Attenkofer, and G. Srajer. *Phys. Rev. Lett.*, 104:046801, 2010.
- [16] T. C. Droubay, S. A. Chambers, A. G. Joly, W. P. Hess, K. Nemeth, K. C. Harkay, and L. Spentzouris. *Phys. Rev. Lett.*, 112:067601, 2014.
- [17] S. Karkare, L. Boulet, L. Cultrera, B. Dunham, X. Liu, W. Schaff, and I. Bazarov. *Phys. Rev. Lett.*, 112:097601, 2014.
- [18] D.H. Dowell and J.F. Schmerge. *Phys. Rev. ST Accel. Beams*, 12:074201, 2009.
- [19] J. D. Koralek, J. F. Douglas, N. C. Plumb, J. D. Griffith, S. T. Cundiff, H. C. Kapteyn, M. M. Murnane, and D. S. Dessau. *Rev. Sci. Instrum.*, 78:053905, 2007.
- [20] J. Feng, J. Nasiatka, W. Wan, T. Vecchione, and H. A. Padmore. *Rev. Sci. Instrum.*, 86:015103, 2015.
- [21] S. Karkare, L. Cultrera, Y. Hwang, R. Merluzzi, and I. Bazarov. *Rev. Sci. Instrum.*, 86:033301, 2015.
- [22] I. Bazarov, L. Cultrera, A. Bartnik, B. Dunham, S. Karkare, Y. Li, X. Liu, J. Maxson, and W. Roussel. *Appl. Phys. Lett.*, 98:224101, 2011.
- [23] R. L. Bell. *Negative affinity electron devices*. Clarendon press, Oxford.
- [24] J. S. Escher. *Semiconductors and Semimetals. Vol . 15: Chapter 3 - NEA Semiconductor Photoemitters*. Academic Press . Inc.
- [25] D. J. Bradley, M. B. Allenson, and B. R. Holeman. *J. Phys. D: Appl. Phys.*, 10:111, 1977.
- [26] J. H. Pollard. Directional properties of emission from negative affinity photocathodes. In *Proceedings of the 2nd European Electro-Optics Markets and Technology Conference*, 1974.
- [27] T. Nishitani *et al.* *J. Appl. Phys.*, 97:094907, 2005.

- [28] W. E. Spicer. *Appl. Phys. A*, 12:115, 1977.
- [29] S. Karkare, D. Dimitrov, W. Schaff, L. Cultrera, A. Bartnik, X. Liu, E. Sawyer, T. Esposito, and I. Bazarov. *J. Appl. Phys.*, 113:104904, 2013.
- [30] Z. Liu, Y. Sun, P. Pianetta, and R. F. W. Pease. *J. Vac. Sci. Technol. B*, 23:2758, 2005.
- [31] S. Karkare, L. Boulet, A. Singh, R. Hennig, and I. Bazarov. *Phys. Rev. B*, 91:035408, 2015.
- [32] S. Karkare and I. Bazarov. *Phys. Rev. Applied*, submitted, 2015.
- [33] K. Aulenbacher, J. Schuler, D. V. Harrach, E. Reichert, J. Rothgen, A. Subashev, V. Tioukine, and Y. Yashin. *J. Appl. Phys.*, 92:7563, 2002.
- [34] B. Yang and Y. L. Xu. *J. Phys. D: Appl. Phys.*, 23:455, 1990.
- [35] G. Vergara, A. Herrera-Gomez, and W. Spicer. *Surf. Sci.*, 436:83, 1999.
- [36] K. Tomizawa. *Numerical simulation of submicron semiconductor devices*. Artech House, Boston.
- [37] R. Ahrenkiel and M. Lundstrom. *Minority Carriers in III-V Semiconductors: Physics and Applications, Semiconductors and Semimetals Volume 39*. Academic press inc.
- [38] M. V. Fischetti and S. E. Laux. *Phys. Rev. B*, 38:9721, 1988.
- [39] D. Vasileska and S. M. Goodnick. Bulk monte carlo: Implementation details and source codes download. <http://nanohub.org/resources/9109>, 2010.
- [40] Electronic archive - new semiconductor materials. characteristics and properties, ioffe institute. <http://www.ioffe.ru/SVA/NSM/>.
- [41] B. V. Zeghbroeck. Principles of semiconductor devices. <http://ecee.colorado.edu/~bart/book/effmass.htm>, 2011.
- [42] J. S. Blakemore. *J. Appl. Phys.*, 53:R123, 1982.

- [43] M. Lundstrom. *Fundamentals of Carrier Transport*. Cambridge University Press.
- [44] B. K. Ridley. *Quantum processes in semiconductors*. Oxford University Press.
- [45] H. C. Casey, D. D. Sell, and K. W. Wecht. *J. Appl. Phys.*, 46:250, 1975.
- [46] Y.-F. Lao and A. G. U. Perera. *J. Appl. Phys.*, 109:103528, 2011.
- [47] A. G. U. Perera. Private communication, 2012.
- [48] M. A. Osman and D. K. Ferry. *Phys. Rev. B*, 36:6018, 1987.
- [49] http://en.wikipedia.org/wiki/Verlet_integration#Velocity_Verlet.
- [50] H. Taniyama, M. Tomizawa, T. Furuta, and A. Yoshii. *J. Appl. Phys.*, 68:621, 1990.
- [51] D. S. Kim. *Monte carlo modeling of carrier dynamics in photoconductive terahertz sources*. PhD thesis, Georgia Institute of Technology, 2006.
- [52] J. Pozela and A. Reklaitis. *Solid State Commun.*, 27:1073, 1978.
- [53] N. G. Nilsson. *Phys. Status Solidi A*, 19:K75, 1973.
- [54] J. J. Scheer and J. V. Laar. *Solid State Commun.*, 5:303, 1967.
- [55] S. M. Sze. *Semiconductor Devices: Physics and Technology*. John Wiley and Sons.
- [56] C. A. Sanford. *Laser pulsed GaAs negative electron affinity photocathodes for electron beam instrumentation*. PhD thesis, Cornell University, 1990.
- [57] D. G. Fisher, R. E. Enstrom, J. S. Escher, and B. F. Williams. *J. Appl. Phys.*, 43:3815, 1972.
- [58] K. L. Jensen, P. G. OShea, and D. W. Feldman. *Appl. Phys. Lett.*, 81:3867, 2002.
- [59] A. Levi. *Applied Quantum Mechanics*. Cambridge University Press.

- [60] D. A. Orlov, M. Hoppe, U. Weigel, D. Schwalm, A. S. Terekhov, and A. Wolf. *Appl. Phys. Lett.*, 78:2721, 2001.
- [61] S. Pastuszka, D. Kratzmann, D. Schwalm, A. Wolf, and A. S. Terekhov. *Appl. Phys. Lett.*, 71:2967, 1997.
- [62] G. Vergara, A. Herrera-Gomez, and W. E. Spicer. *J. Appl. Phys.*, 80:1809, 1996.
- [63] S. Karkare and I. Bazarov. *Appl. Phys. Lett.*, 98:094104, 2011.
- [64] L. Cultrera, I. Bazarov, A. Bartnik, B. Dunham, S. Karkare, R. Merluzzi, and M. Nichols. *Appl. Phys. Lett.*, 99:152110, 2011.
- [65] Y. Zhang, B. Chang, J. Niu, J. Zhao, J. Zou, F. Shi, and H. Cheng. *Appl. Phys. Lett.*, 99:101104, 2011.
- [66] Herbert S. Bennett. *J. Appl. Phys.*, 83:3102, 1998.
- [67] Colwyn Gulliford *et al.* *Phys. Rev. ST Accel. Beams.*, 16:073401, 2013.
- [68] T. Vecchione, D. Dowell, W. Wan, J. Feng, and H. A. Padmore. Quantum efficiency and transverse momentum from metals. In *Proceedings of FEL, New York*, 2013.
- [69] L. Cultrera, S. Karkare, H. Lee, X. Liu, I. Bazarov, and B. Dunham. *Phys. Rev Lett.*, *submitted*, 2015.
- [70] S. Schubert, M. Ruiz-Oses, I. Ben-Zvi, T. Kamps, X. Liang, E. Muller, K. Muller, H. Padmore, T. Rao, X. Tong, T. Vecchione, and J. Smedley. *APL Materials*, 1:032119, 2013.
- [71] H. J. Qian, C. Li, Y. C. Du, L. X. Yan, J. F. Hua, W. H. Huang, and C. X. Tang. *Phys. Rev. ST Accel. Beams*, 15:040102, 2012.
- [72] S. Karkare, I. Bazarov, L. Cultrera, A. Iyer, X. Liu, and W. Schaff. Effect of surface roughness on the emittance from gaas photocathode. In *Proceedings of Particle Accelerator Conference, New York, NY, USA*, 2011.
- [73] Th. Glatzel, S. Sadewasser, R. Shikler, Y. Rosenwaks, and M. Ch. Lux-Steiner. *Mat. Sci. Eng. B*, 102:138, 2003.

- [74] W. Melitz, J. Shena, A. Kummel, and S. Lee. *Surf. Sci. Rep.*, 66:1, 2011.
- [75] C. Barth and C. R. Henry. *Nanotechnology*, 17:S155, 2006.
- [76] Nicolas Gaillard, Denis Mariolle, Francois Bertin, Mickael Gros-Jean, and Ahmad Bsiesy. Metal electrodes work function measurement at decanometer scale using kelvin probe force microscope: a step forward to the comprehension of deposition techniques impact on devices electrical properties. In *Symposium E Gate Stack Scaling Materials Selection, Role of Interfaces, and Reliability Implications*, volume 917 of *MRS Proceedings*, 2006.
- [77] E. Harier, C. Lubich, and G. Wanner. *Geometric Numerical Integration - Structure Preserving Algorithms for Ordinary Differential Equations*. Springer Series in Computational Mathematics, 2006.
- [78] Peter Johansson. *Phys. Rev. B*, 48:8938, 1993.
- [79] D. Z.-Y. Ting, E. T. Yu, and T. C. McGill. *Phys. Rev. B*, 45:3583, 1992.
- [80] D. Z. Y. Ting, S. K. Kirby, and T. C. McGill. *Appl. Phys. Lett.*, 64:2004, 1994.
- [81] D. Z. Y. Ting, S. K. Kirby, and T. C. McGill. *J. Vac. Sci. Technol. B*, 11:1738, 1993.
- [82] W. T. Dietze and R. B. Darling. *Phys. Rev. B*, 53:3925, 1996.
- [83] H. C. Liu and D. D. Coon. *J. Appl. Phys.*, 64:6785, 1988.
- [84] Kai Sandfort. *The Factorization Method for Inverse Scattering from Periodic Inhomogeneous Media*. PhD thesis, Karlsruher Institut für Technologie, 2010.
- [85] D. T. Pierce, R. J. Celotta, G.C. Wang, W. N. Unertl, A. Galejs, C. E. Kuyatt, and S. R. Mielczarek. *Rev. Sci. Instrum.*, 51:478, 1980.
- [86] A.J. Van Bommel and J.E. Crombeen. *Surf. Sci.*, 45:308, 1974.
- [87] A.J. Van Bommel and J.E. Crombeen. *Surf. Sci.*, 57:109, 1976.
- [88] L. J. Whitman, Joseph A. Stroscio, R. A. Dragoset, and R. J. Celotta. *Phys. Rev. Lett.*, 66:1338, 1991.
- [89] T. Yamada, J. Fujii, and T. Mizoguchi. *Surf. Sci.*, 479:33, 2001.

- [90] A.J. Van Bommel, J.E. Crombeen, and T.G.J. Van Oirschot. *Surf. Sci.*, 72:95, 1978.
- [91] J. Kim, M.C. Gallagher, and R.F. Willis. *Appl. Surf. Sci.*, 67:286, 1993.
- [92] B. Goldstein. *Surf. Sci.*, 47:143, 1975.
- [93] J. Derrien and F. A. D'avitaya. *Surf. Sci.*, 65:668, 1977.
- [94] J. Derrien and F. A. D'avitaya. *Rev. Phys. Appl.*, 11:377, 1976.
- [95] B. Goldstein and D. Szostak. *Appl. Phys. Lett.*, 26:111, 1975.
- [96] D. Rodway. *Surf. Sci.*, 147:103, 1984.
- [97] V.L Alperovich, O.E Tereshchenko, A.N Litvinov, and A.S Terekhov. *Appl. Surf. Sci.*, 175-176:175, 2001.
- [98] Livia Giordano, Fabrizio Cinquini, and Gianfranco Pacchioni. *Phys. Rev. B*, 73:045414, 2006.
- [99] S. H Chou, J. Voss, I. Bargatin, A. Vojvodic, R. T. Howe, and F. Abild-Pedersen. *J. Phys.: Condens. Matter*, 24:445007, 2012.
- [100] A. K. Singh, H. L. Zhuang, and R. G. Hennig. *Phys. Rev. B*, 89:245431, 2014.
- [101] S. E. Kulkova, S. V. Ereemeeva, A. V. Postnikov, and I. R. Shein. *J. Exp. Theor. Phys.*, 104:590, 2007.
- [102] C. Hogan, D. Paget, Y. Garreau, M. Sauvage, G. Onida, L. Reining, P. Chiaradia, and V. Corradini. *Phys. Rev. B*, 68:205313, 2003.
- [103] G. Kresse and J. Furthmuller. *Phys. Rev. B*, 54:11169, 1996.
- [104] P. E. Blochl. *Phys. Rev. B*, 50:17953, 1994.
- [105] G. Kresse and D. Joubert. *Phys. Rev. B*, 59:1758, 1999.
- [106] J. P. Perdew, A. Ruzsinszky, J. Tao, V. N. Staroverov, G. E. Scuseria, and G. I. Csonka. *J. Chem. Phys.*, 123:062201, 2005.

- [107] G. P. Srivastava and S. J. Jenkins. *Phys. Rev. B*, 53:12589, 1996.
- [108] S.E. Kulkova, D.V. Khanin, and A.V. Subashiev. *Nucl. Instrum. Meth. A*, 536:295, 2005.
- [109] G. Mills, H. Jonsson, and G. K. Schenter. *Surf. Sci.*, 324:305, 1995.
- [110] H. Jonsson, G. Mills, and K. W. Jacobsen. *Nudged Elastic Band Method for Finding Minimum Energy Paths of Transitions*. World Scientific, 1998.
- [111] L. W. James and J. L. Moll. *Phys. Rev.*, 183:740, 1969.
- [112] A. S. Terekhov and D. A. Orlov. *JEPT Lett.*, 59:864, 1994.
- [113] H. J. Drouhin, C. Hermann, and G. Lampel. *Phys. Rev. B*, 31:3859, 1985.
- [114] L.B. Jones, R.J. Cash, B.D. Fell, K.J. Middleman, T.C.Q. Noakes, B.L. Milit-syn, H.E. Scheibler, D.V. Gorshkov, and A.S. Terekhov. The commissioning of tess: An experimental facility for measuring the electron energy distribution from photocathodes. In *Proceedings of FEL, New York*, 2013.
- [115] A.L. Bukhgeim, V.E. Andreev, and A.S. Terekhov. *J. Inv. Ill-posed Problems*, 7:427, 1999.
- [116] Richard Fitzpatrick. Plasma physics, the university of texas at austin. <http://farside.ph.utexas.edu/teaching/plasma/lectures/node21.html>.
- [117] Markus Hoppe. *Differential energy analysis of electron beams : A study of Photoemission for NEA-GaAs*. PhD thesis, Rupretus Carola University of Heidelberg, Germany, 2001.
- [118] A.I.Morozov *et al.* *Review of Plasma Physics, Consultants Bureau*, 2:101–197, 1966.
- [119] Udo Weigel. *Cold Intense Electron Beams from Gallium Arsenide Photocathodes*. PhD thesis, Rupretus Carola University of Heidelberg, Germany, 2003.